MOLECULAR MODELING OF IONIC LIQUIDS: STRUCTURE, DYNAMICS AND ELECTROCHEMICAL PERFORMANCE IN SUPERCAPACITORS

By

Song Li

Dissertation

Submitted to the Faculty of

Graduate School of Vanderbilt University

In partial fulfillment of the requirements

for the degree of

DOCTOR OF PHILOSOPHY

In

CHEMICAL ENGINEERING

May, 2014

Nashville, Tennessee

Approved:

Peter T. Cummings, Ph.D.

Clare M. McCabe, Ph.D.

Kane G. Jennings, Ph.D.

Kalman Varga, Ph.D.

DEDICATION

This dissertation is dedicated to my husband, Yuqiang Zhao, whose love and encouragement support me throughout my Ph.D. study, and to my encouraging parents and supportive friends in Vanderbilt University.

ACKNOWLEDGMENTS

I would never have been able to complete my dissertation without the guidance of my advisor, help from group members and support from my family.

I would like to express my deepest and sincerest gratitude to my advisor, Professor Peter T. Cummings for his guidance, encouragement and support throughout the course of this work. His extensive knowledge, insightful vision and creative thinking inspired me to pursue not only my Ph.D. but also a future career in scientific research. I greatly appreciate the opportunities provided for me by Prof. Cummings to present my work and communicate with other researchers in international conferences. I would also like to thank my committee members: Prof. Clare McCabe, Prof. Kane G. Jennings and Prof. Varga Kalman. Their invaluable critiques and helpful suggestions are precious during this process.

Special thanks go to Dr. Guang Feng, whose instruction and mentorship greatly improve my research skills and scientific thinking. I appreciate the time and effort he spent for inspiring discussion and helpful advices. His passion for scientific research and philosophy also boost my motivation to pursue an academic position. I also gratefully appreciate the discussion with several members in Cummings Group: Li Wan, Dr. William French, Dr. Mingjie Wei and Dr. Stepan Hlushak. I really enjoy the time in laboratory with their warmhearted help and friendship.

I would like to sincerely thank Dr. David J. Wesolowski, the director of Fluid Interface Reactions, Structures and Transport (FIRST) center, an Energy Frontier Research Center. I cherish and appreciate the collaborating opportunities provided by FIRST center throughout my Ph.D. and the chance to meet and communicate with excellent researchers from different fields. A big thank you goes to several collaborators in FIRST center: Dr. José Leobardo Bañuelos (ORNL), Dr. Pasquale F.

Fulvio(ORNL), Dr. Kee Sung Han (ORNL), Dr. Jianchang Guo (ORNL), Dr. Pengfei Zhang (ORNL), Katherine L. Van Aken (Drexel University), John K. McDonough (Drexel University). They performed the experiments to support the simulation results discussed in this dissertation. In addition, I would like to thank Dr. Sheng Dai, Dr. Edward Hagaman and Dr. Yury Gogotsi. Their encouragement and help make me bravely face the challenges and difficulties in research.

I also own my gratitude to all of my friends in Vanderbilt University, especially those in Department of Chemical and Biomolecular Engineering. Their company and friendship make my life during Ph.D. study less stressful and full of happiness. Finally, I would like to thank my beloved husband, Yuqiang Zhao, my parents and parents-in-law. Without their love, patience, and sacrifice, I cannot complete this work and achieve my goals.

Table of Contents

LIST OF FIGURES

Figure Page

LIST OF ABBREVATIONS

MD molecular dynamics

RTILs room temperature ionic liquids

SAXS small angle X-ray scattering

FCS fluorescence correlation spectroscopy

NMR nuclear magnetic resonance

AFM atomic force microscopy

DSC differential scanning calorimetry

RDF radial distribution function

HOP heterogeneity order parameter

MILs monocationic ionic liquids

DILs dicationic ionic liquids

EDLs electric double layers

PZC potential of zero charge

OLC onion-like carbon

C-V differential capacitance – electric potential

$[C_nMPy][Tf_2N]$ 1-alkyl-1-methylpyrrolidinium bis(trifluoromethanesulfonyl)-imide

$[C_4mpip][Tf_2N]$ 1-methyl-1-butylpiperidinium bis(trifluoromethylsulfonyl)imide

$[C_n(mim)_2](BF_4)_2$ 1-alkyl-3-dimethylimidazolium tetrafluorborate

CHAPTER I

INTRODUCTION

Room temperature ionic liquids (RTILs) have attracted increasingly wide attention in recent years[1-3] due to their low vapor pressure, high thermal and electrochemical stability, non-combustibility, tunable miscibility and so on.[1,2] RTILs have been used in a variety of fields, such as catalysts, solvents, lubricants and electrolytes for energy storage devices including batteries, fuel cells and supercapacitors. Supercapacitors, also named electric double layer capacitors (EDLCs), store electric energy into the electric double layers (EDLs) near electrode surfaces by physically accumulation of ions, which exhibit comparable energy density with lithium batteries and ultrahigh power density in contrast to other energy storage devices.[4] These days, the development of RTILs electrolytes-based supercapacitors has won increasingly research interests due to the outstanding properties of RTILs as electrolytes. However, there are still lots of problems unresolved on the structural organization, dynamics and capacitive performance of RTILs electrolytes.

RTILs consisting of cations and anions are structurally more ordered and designable by tuning their structure and composition.[5] Thus task-specific RTILs with improved properties can be obtained by rationally modification. Therefore, to understand the structure-functionality relationship in RTILs is of great importance for rational design of RTILs. Experimental and theoretical studies[6,7] reported that spatial heterogeneity in RTILs is responsible for many observed phenomena such as decreased polarity, low density, and increased dynamics heterogeneity. Small angle X-ray scattering (SAXS) revealed that the spatial heterogeneity in long-chain imidazolium-based RTILs is a

consequence of segregation of polar cation head/anion and nonpolar alkyl tails,[7-9] which is also verified by computational work.[6] For novel type of RTILs, such as pyrrolidinium-based RTILs and dicationic ionic liquids (DILs), the influence of different chain lengths on the nanoscale organization is still rarely reported.

In addition, the properties of RTILs are also greatly influenced by confinements. It is known that the dynamics, structure, phase transition temperature of RTILs are changed once confined.[10] To interpret solid-liquid interfacial behavior of RTILs in confinements is crucial for the fundamental study and their application in lubrication and energy storage devices. At last, the capacitive performance of RTILs electrolytes, determined by the EDLs mainly consisting of counter-ions accumulated at charged electrode, whose thickness is directly related to the energy density stored in supercapacitors. The influence of temperature, ion size, anion type, solvents on EDLs are still elusive.

All-atom molecular dynamics (MD) simulation is a powerful tool to investigate RTIL spatial heterogeneity, dynamics in confinement and EDLs in supercapacitors. MD simulation has been successfully used to predict the structural segregation in RTILs and obtain the structure factor in consistent with that obtained from SAXS.[11] The interfacial dynamics of RTILs in confinement measured from NMR also exhibit a good agreement with MD-obtained results.[12] And MD simulation has been commonly used in predicting the EDLs of RTILs at carbon electrode in atomic level.[13,14] Therefore, MD simulation is the major tool used in this dissertation to characterize RTILs and their performance as electrolytes in supercapacitors.

The rest of dissertation was organized as follows: Chapter II summarizes the properties and applications of RTIL as well as the recent studies on spatial heterogeneity

of RTILs and RTILs electrolytes in supercapacitors. Chapter III provides a brief introduction into MD simulation and relevant methods used for analyzing spatial heterogeneity of RTILs and computing the capacitance used to estimate the energy density of supercapacitors. Next, in Chapter IV, the structural organizations of monocationic ionic liquids (MILs) $[C_nMPy][Tf_2N]$ and dicationic ionic liquid (DILs) $[C_n(mim)_2](BF_4)_2$ with varying chain lengths were investigated.[11,15] The spatial heterogeneity was estimated through structure factors of bulk RTILs calculated using Eq. 3.1 and directly compared with the results obtained from SAXS.[11] The influence of temperature on spatial heterogeneity of $[C_nMPy][Tf_2N]$ was also studied for the first time by MD simulation.

Moreover, due to the dissimilar chemical structure of DILs in contrast to their monocationic counterparts, different spatial heterogeneities of DILs are expected, which is delineated in Chapter IV.

Chapter V focuses on the confinement effects on RTILs $[C_4mim][Tf_2N]$ in silica and carbon mesopores at different loading fractions and temperatures by MD simulations.[12] Although confinement alter the behavior of RTILs compared to that in bulk, different solid materials may exert dissimilar influences on confined RTILs. Silica and carbon mesopores are used as two typical solid nanomaterials. The interfacial behavior of RTILs at different solid materials is probably critical for the performance of RTILs electrolytes in EDLs and RTILs as lubricants. This study may inspire further experimental research on RTILs near differently featured solid walls as well as provide a baseline of neutral liquid-solid interfaces for the application of confined RTILs in the field of energy storage devices and lubrication.

In Chapter VI, the performance of RTILs electrolytes in carbon electrode-based supercapacitors are investigated using MD simulations. The binary mixture of RTILs is reported to exhibit higher conductivity and lower melting point than neat RTILs, which is expected to be a promising electrolytes at severe cold weather conditions.[16] Moreover, the temperature influence on the EDLs was investigated. Although the positive temperature dependent capacitance has been observed in lots of experiments,[16-18] the acceptable explanation for this phenomenon is still missing. This is the first study that reveals the reason of the positive temperature dependence of capacitance with the increase of temperature by MD simulation.[14] In addition, the performance of DILs electrolytes in supercapacitors was studied.[19] DILs with dications carrying two unit charges have more concentrated charge density and are supposed to exhibit different behaviors in contrast to counterpart MILs. In addition, the shape of the differential capacitance-electric potential (C-V) curves for DILs is also expect to be different from those of MILs. This study provides fundamental molecular insights and explanation into the behaviors of DILs in EDLs. Finally, the influence of organic solvents is investigated.[20] The application of DILs electrolytes is impeded by their slow dynamics, which greatly limits the charge/discharge rate of DILs-based supercapacitors. Organic solvent such as acetonitrile has been reported to be able enhance the conductivity and dynamics of RTILs, which makes DILs/organics solvents are promising electrolyte with enhanced performance..

Finally, Chapter VII summarizes the conclusions obtained from the above studies and make recommendations for furture work.

CHAPTER II

BACKGROUND

2.1 Ionic Liquids

Interest in room temperature ionic liquids (RTILs) has risen dramatically since the late 1990s. RTILs are organic salts with low melting points (below room temperature), which exist as liquids at room temperature. In *common* with molten salts (such as molten NaCl, obtained by heating NaCl above its melting point of 1074K), RTILs consist of cations and anions in a liquid phase. However, in contrast with simple molten salts, RTILs consist of exclusively organic cations and organic or inorganic anions. Since the first RTIL was identified and characterized by Walden in 1914,[21] RTILs have won considerable attention from the research community due to their unique characteristics. Unlike most conventional liquids, ionic liquids possess negligible vapor pressure, high thermal and electrochemical stability, outstanding electric conductivity, non-combustibility, and tunable miscibility, among other properties.[1,2,22,23]

Although RTILs were initially synthesized for use as catalytic or green solvent candidates in organic chemistry, their potential applications were further extended to inorganic chemistry, electrochemistry, material science and biochemistry with more and more task-specific RTILs produced.[5] Task-specific ionic liquids, also named functionalized ionic liquids, are synthesized by incorporating various functional groups into cations or anions to impart desired physical and/or chemical properties. To date, RTILs are being widely studied in multiple fields as illustrated in Figure 2.1.[24] Among these applications, RTILs as promising electrolyte candidates[25] are of particular interest

to our research. Currently the most popular families of RTILs are those having imidazolium-, piperidinium- or pyrrolidinium-based cations. Among all of them, the imidazolium-based RTILs are the most frequently studied as electrolytes due to their outstanding stability and electroconductivity. Piperidinium- and pyrrolydinium-based RTILs have not been extensively studied. As for anions, bis(trifluoromethanesulfonyl)amide (Tf_2N) is commonly used as the anion due to its extraordinary electrochemical stability, low viscosity and high conductivity.[26]

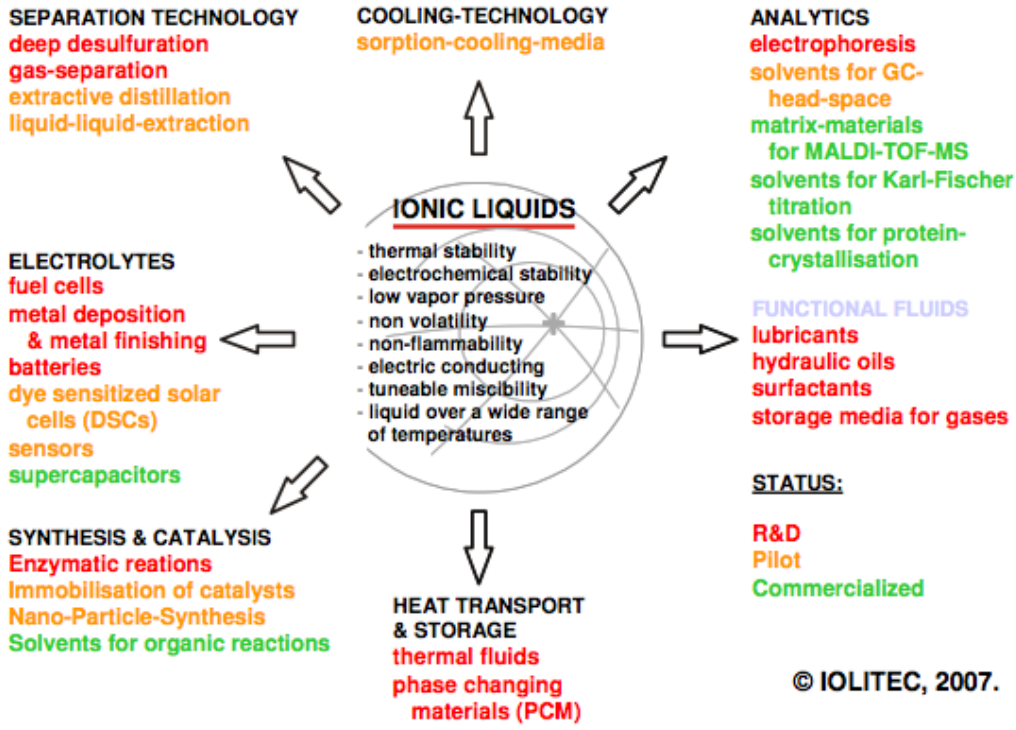

Figure 2.1. Potential applications of ionic liquids. Reproduced from Ref. 24.[24]

2.2 Spatial Heterogeneity in Ionic Liquids

Ionic liquids can be tailored to specific applications by fine-tuning the functional groups of the weakly coordinating organic cation and the inorganic/organic anion.[27] The spatial heterogeneity is a special feature of ionic liquids with long alkyl chain in cations, which is attracting increasing research interests. It is known that the alkyl chain length of

the cation influences both the physical and chemical properties of RTILs. A longer cation side chain is commonly accompanied by lower density, lower solubility, slower diffusion, higher viscosity[28-30] and heterogeneous dynamics observed in neutron spin echo[31,32] and MD simulation.[33,34] It is also reported that the "red-edge effects" observed in ionic liquids in the study of fluorescence of the organic probe 2-amino-7-nitrofluorene is related with the structural and dynamical heterogeneity.[35]

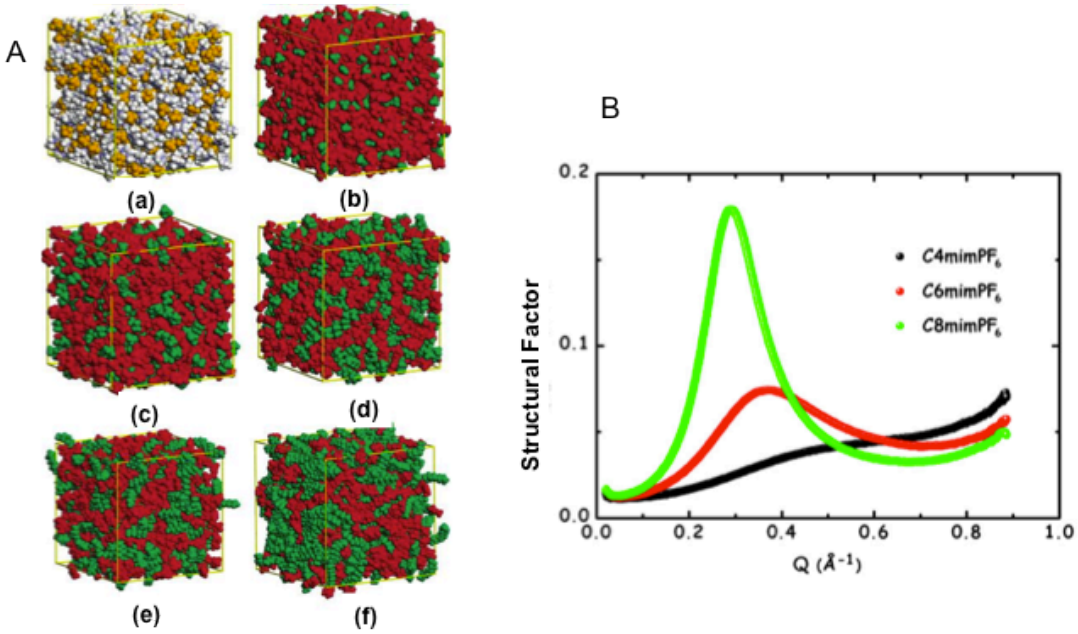

Figure 2.2. Spatial heterogeneity observed in (A) snapshots of MD simulation[36] and (B) structure factor from SAXS measurement.[37] (A) presents the snapshots of [$C_n$mim+][PF_6-]: (a) n=2 CPK coloring; (b) n=2, red/green coloring; (c) n=4; (d) n=6; (e) n=8; (f) n=12.

Imidazolium-based ionic liquids, one of the most studied RTILs to date, have been reported to exhibit aggregation behavior as a function of alkyl chain length by atomistic/coarse-grained molecular dynamics simulation.[38-41] Experimentally, small angle X-ray scattering (SAXS), a technique adopting elastic scattering of X-rays and recording the structural information of a sample with heterogeneities at very low angles (typically

0.1–10°)[42] was employed to investigate the structural heterogeneity in ionic liquids. SAXS has also been used to identify the presence of liquid crystalline phases in imidazolium-based ionic liquids with $n \geq 12$, depending on the type of anion,[43] while structural heterogeneity has been found in shorter alkyl chain ionic liquids.[37,44,45] The effect of cation asymmetry on structural heterogeneity[28,46] and several physicochemical properties[47] has also been recently addressed. Small angle neutron scattering has also been used to show that the increased heterogeneity stems primarily from the increasing asymmetry of the cation as the chain length is increased.[8,48] The obtained structure function from SAXS as shown in Figure 2.2B exhibit an increased prepeak at 0.3 $Å^{-1}$ as the prolongation of alkyl chain, which associates with the enhanced aggregation of ionic liquids. So far, the molecular insight into the spatial heterogeneity in ionic liquids, especially the novel type of ionic liquids, for instances, $[C_nMPy][Tf_2N]$ and dicationic ionic liquids, is still unexplored. Therefore, more investigations are required in this field.

2.3 Ionic Liquids Electrolytes in Supercapacitors

The low operating voltage, leading to low energy density of energy storage devices, and high evaporation pressure restricts the use of conventional aqueous electrolytes. RTILs are promising alternatives in energy storage devices due to their good physical and chemical properties. The recent application of RTILs as electrolytes in energy storage devices (for example, lithium batteries, fuel cells and supercapacitors) has captured the attention of a growing number of scientists. In the development of lithium-based battery, the limited operating temperature range, volatility and flammability of electrolytes and narrowness of electrochemical windows constitute key challenges. RTILs, with a wide range of operation temperatures, high thermal stability and electric conductivity, and

wider electrochemical window, are promising replacements for conventional electrolytes.[49,50] A series of studies have been, or are being, conducted to evaluate the performance of batteries and supercapacitor using RTILs as electrolytes.[51] Imidazolium-based RTILs have been most frequently investigated as electrolytes in Li batteries.[52-54] Mixed ionic liquids were also adopted as a potential battery electrolyte in order to lower the viscosity and enhance the thermal stability.[55] Compared to the applications of RTILs in battery, the use of RTILs in fuel cell is not widely studied due to its special requirement for RTILs. Fuel cells work differently from batteries by consuming the fuels (usually hydrogen) and oxidant (oxygen) to convert chemical energy into electric energy. In a fuel cell, RTILs serve as proton transport media, which can be satisfied by the protic ionic liquids electrolytes. Protic ionic liquids consist of Brønsted acids as proton generator and Brønsted bases as proton acceptor, by which the transportation of protons between cathode and anode can be realized.[56,57]

The use of RTILs in supercapacitors has been widely studied for some time. Unlike batteries and fuel cells, supercapacitors store electric energy by the physical movement of ions rather than by chemical redox reaction. The supercapacitor (or EDLC) is a rechargeable device that stores energy by accumulating electric charge in the electric double layer at the interface between electrode and electrolyte.[4] In terms of electric power and energy, supercapacitors store higher energy than conventional capacitors but lower than batteries and fuel cells; thus, supercapacitors fill the energy density gap between capacitors and batteries as shown in Figure 2.3. Supercapacitors have won growing attentions due to their high power density and long cycling life, and they greatly exceed batteries and fuel cells in relation to power density. The performance of supercapacitors

is primarily influenced by two factors: the electrolyte employed and the electrode materials used. Based on their favorable properties, RTILs are considered to be promising supercapacitor electrolytes.

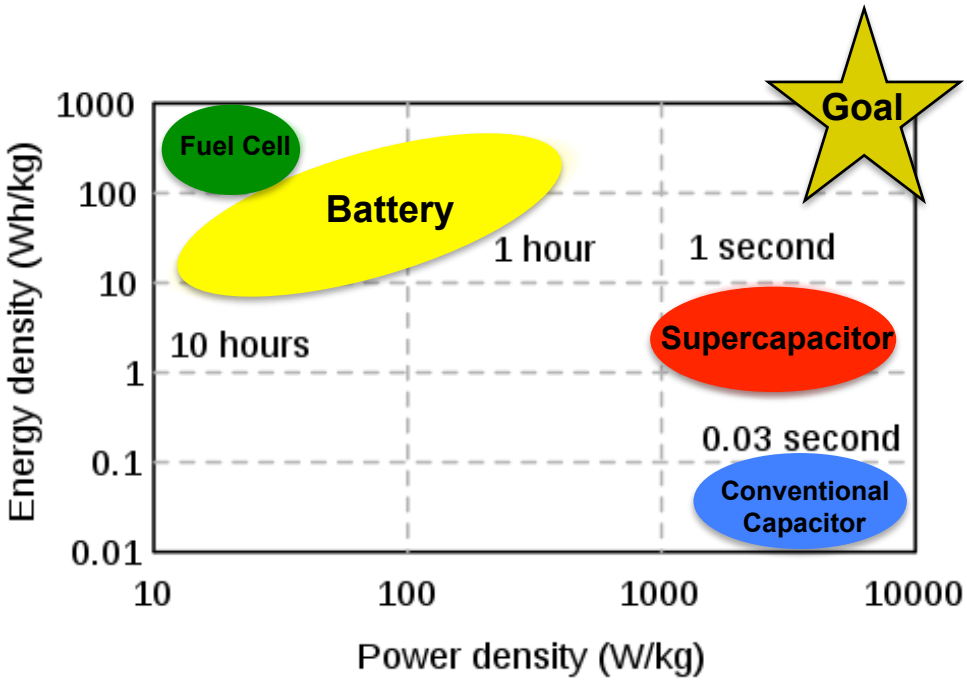

Figure 2.3. Ragone plot for various energy storage devices. (Image adapted from http://newenergyandfuel.com/)

The performance of a supercapacitor is commonly rated by its capacitance, which is a measure of the capability of the supercapacitor to store electric energy. There are two main types of capacitances used to evaluate the performance of supercapacitors: normalized electric double layer capacitance and normalized differential capacitance.[58] The normalized electric double layer capacitance is defined as the ratio of the electric charge per unit area and the electrode-electrolyte potential difference.

$$C_{EDL} = \frac{Q}{V_{EDL}} \frac{1}{A_{electrode}}$$

In this equation, C_{EDL} is the normalized EDL capacitance per unit area. Q is the charge stored; $A_{electrode}$ is the specific surface area of the electrode and σ is the electrode surface charge density. V_{EDL} is the potential drop across the EDL, which is calculated as $V_{EDL} = V_{electrode} - V_{bulk}$.

The normalized differential capacitance is defined as the ratio of the changes (dQ) in charge per unit area and the corresponding change (dV_{EDL}) in electrode potential:

$$C_d = \frac{dQ}{dV_{EDL}} \frac{1}{A_{electrode}}$$

The differential capacitance curve is also commonly used to assess supercapacitor performance, and it is found to predominantly exhibit three qualitative shapes: the bell-shaped, camel-shaped and U-shaped curves shown in Figure 2.4.

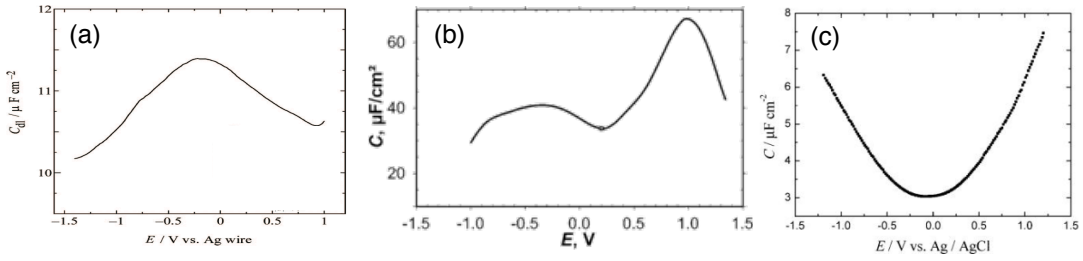

Figure 2.4.Varying differential capacitance curves: a) bell-shaped C-E curve measured at the platinum electrode in argon-saturated [$DMOA^+$][Tf_2N^-] [59]; b) camel shaped C-E curve measured at glassy carbon electrode in [C_4mim+][Cl-] [60]; c) U shaped C-E curve measured at the HOPG electrode in nitrogen-saturated [Bmim+][BF_4 -].[61]

In terms of electrode materials, the widely used carbon-based electrode is considered to be one of the most suitable materials because of its favorable properties, such as low cost, high thermal and electrochemical stability, tunable forms and easy operation. For

parallel capacitors, the capability of electric energy that the capacitor is able to accumulate is expressed in the following equation [4]

$$C = \frac{\varepsilon_r \varepsilon_0}{d} A$$

where C is the capacitance, ε_r is the electrolyte dielectric constant, ε_0 is the vacuum permittivity, A is the accessible electrode surface area to electrolyte, d is the effective electric double layer thickness. From the above equation, it is evident that increase of the effective surface area or decrease of the EDL thickness will result in the increase of the capacitance. Thus, a series of carbon-based electrodes with large surface area have been considered, such as activated carbon, carbon nanotube and carbon onions.

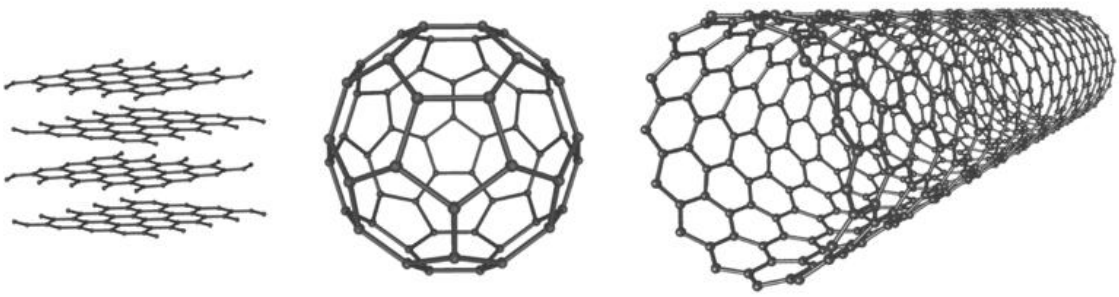

Figure 2.5. Examples of possible carbon-based electrodes (from left to right): graphite, buckylball and nanotube.[62]

CHAPTER III

METHODOLOGY

3.1 Molecular Dynamics Simulation

Molecular dynamics (MD) simulation is one of the most widely used atomistic techniques based on classical Newtonian equation of motion. In comparison with other atomistic techniques such as molecular mechanics and Monte Carlo, time evolution of interacting atoms and time scale are explicitly present in MD simulation, by which the macroscopic properties (such as kinetic energy, temperature, diffusion coefficient, etc.) can be computed by time-averaging of the behavior of individual atoms. In MD simulation, provided the initial condition of the system and the inter-atomic potential, the atomic position, velocity, etc will be updated within required time by integration of the equation of motion. The output information can be then used to compute macroscopic properties related to structure and dynamics. MD simulation can explicitly model the interfacial behavior of electrolytes and the structure of EDLs, e.g. ion distribution and orientation,[63-66] which are difficult to be exploited from experimental studies.

Several models have been proposed to describe the microstructure of the EDL. The Helmholtz model[67] is firstly proposed, which describes the EDL as the single layer formed by compact counter ions near electrode surface and the charges on electrode are completely compensated by the compact layer. Thus in Helmholtz model, the potential drop linearly due to the rigid layer, which contradicts with experimental observation. The Gouy-Chapman model[68,69] described the EDL as diffusive double layer consisting of counter-ions and co-ions. Stern then modified the Gouy-Chapman theory.[70] In this model, the EDL contains one compact layer formed by counter ions and one diffusive layer.

However, both theories are based on the dilute electrolyte and ions are well separated and only electrostatic interaction between ions is taken into accounted, which are not true for solvent-free RTILs in nature.

MD simulation is able to provide more realistic information on the EDLs structure formed by ionic liquids in contrast to other theoretical studies: such as ab initio molecular dynamics (AIMD), Monte Carlo (MC) and continuum theory. Although AIMD is more accurate investigating the electronic structure of many-body system, the limited system size, time scales and expensive computation restrict its application in EDL modeling due to the large system size and long equilibration time required for EDL structure. MC is able to model the system in atomic level as MD simulation. Nevertheless, it cannot be used to obtain the complete description of the dynamics properties of the system as MD simulation. Even though both continuum and MD simulation are feasible for the EDL modeling, continuum simulation uses averaged description for modeling the interfacial properties by assuming the electrolytes and ion distribution are continuous, which neglects the discretization of charge in nature. Therefore the localized non-linear material deformation, micro/nano-scale material structures, ion distribution and various nano-scale phenomena cannot be explicitly described by continuum simulation. Additionally, continuum simulation is limited by low electrolytes concentration and applied potential. And its Poisson-Boltzmann equation overestimates the electrolytes concentration and thus the capacitance due to the missing of finite ion size in continuum simulations.[71] However, in MD simulation, individual atoms with finite size are modeled and molecular shape and inter-atomic potentials are taken into account, which describe the system more realistically.

3.2 Data Analysis

3.2.1 Structure Factor Calculation

Static structure factor or structure function is a mathematical description of how materials (in this case, RTILs) scatter incident irradiation such as X-ray, neutron or electron. It provides particular useful information on the structural organization of materials under investigation. Structure factor can be experimentally measured using small angle X-ray/neutron scattering (SAXS/SANS), which has been extensively used in exploring the spatial heterogeneity observed in long-chain RTILs. In theory, structure factor is also calculated to predict or verify the structural arrangements in RTILs. To compare the calculated structure factor for RTILs with that obtained from small angle X-ray scattering, the X-ray weighted total structure function $S(Q)$ at wave number Q is calculated based on the atom correlation functions using the following equation[72]

$$S(Q) = \frac{\sum_{\alpha\beta} \chi_\alpha \chi_\beta f_\alpha(Q) f_\beta(Q) 4\pi\rho \int_0^{r_c} [g_{\alpha\beta}(r) - 1] r^2 \frac{\sin(Qr)}{Qr} dr}{\left[\sum_{\alpha\beta} \chi_\alpha f_\alpha(Q)\right]^2} \qquad (3.1)$$

Where, χ_α and χ_β are the mole fractions of atom species α and β, $f(Q)$ is the form factors of atom species , and $g_{\alpha\beta}(r)$ is the atom-atom radial distribution function (RDF) between, atom species α and β, which is obtained from the output of MD simulation. For radial distribution functions computed from simulation, the upper limit (truncation point) in the integrals in Eqn. (3.1) is the cutoff point r_c, which equals half of the simulation box length. All calculated structure functions are only shown for $Q \geq \frac{2\pi}{r_c} = \frac{4\pi}{L}$, where L is the simulation box length. This is because of the truncation of the RDFs at $r = r_c = L/2$, which makes $S(Q)$ unreliable for $Q \leq 2\pi / r_c$; even without truncation of the RDF, $S(Q)$

would be unreliable for $Q \leq 2\pi/L$ due to the periodic boundary conditions with periodicity in real space of length L in each coordinate direction.

3.2.2 Supercapacitor Capacitance Computation

The capacitance calculation of supercapacitors is dependent on the model of electrode adopted. For parallel graphite-based supercapacitors, the simulation setup is as follows. The parallel graphene sheets are adopted as electrodes and their positions are fixed during the simulation as in experiment. The distance between two electrodes is tunable. The system is setup as shown in the Figure 3.1. Periodic boundary condition is applied in both x and y dimensions but not in z dimension, which will give rise to infinite electrode surface area. The graphite is parallel to x-y plane. The density of RTILs in the middle of the channel will remain the same as the bulk density. The electrode is charged directly by attributing the same quantity of partial charge to each carbon atom in the inner graphene sheets of electrodes. As the electrode is neutral, only van der Waals interaction between electrode and electrolyte is taken into account; as the electrode is charged, both van der Waals interaction and electrostatic interaction will be accounted.

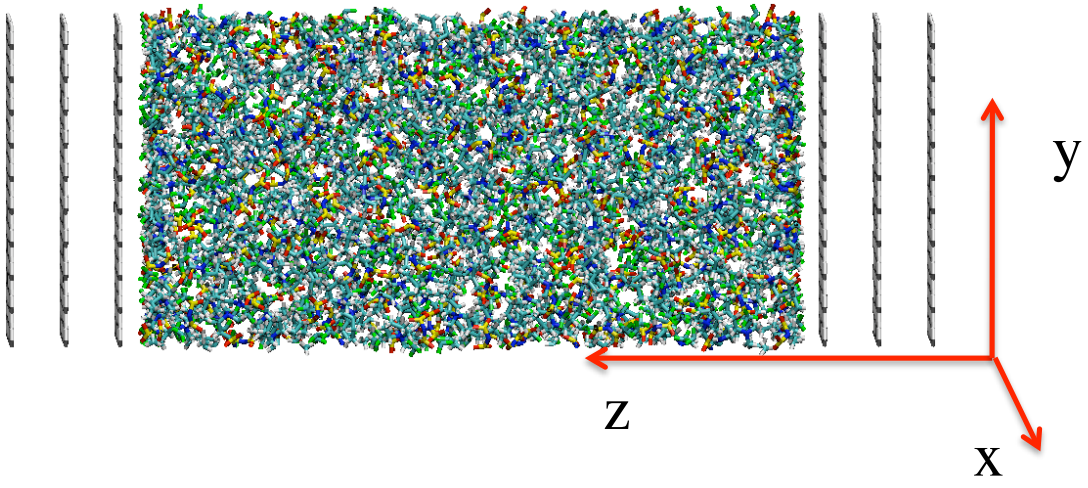

Figure 3.1. Simulation setup for graphite/RTILs-based supercapacitors

The number density profile $\rho_n(z)$ of cations and anions will be calculated using binning method,[73] which is the density distribution as a function of the distance between electrolytes and electrode surface (defined as z). Density profile provides the information of ion distribution and EDL structure.

The normalized capacitance is computed with the following equation.

$$C_{EDL} = \frac{\sigma}{\phi_{EDL} - PZC} \qquad (3.2)$$

where σ is the surface charge density and ϕ_{EDL} is the potential drop across the EDL with surface charge density σ. PZC is the potential of zero charge, which is the potential drop as the electrode is neutral, *i.e.*, ϕ_{EDL} at σ=0. PZC is the potential drop caused by physical affinity between electrode and the ions in electrolytes. It is calculated here to calibrate the EDL potential drop as the electrode surface is charged. The potential distribution can be obtained by numerical integration of the reduced 1D Poisson Equation.[74]

$$\nabla^2\phi = -\frac{\rho_e}{\varepsilon_0} \qquad (3.3)$$

ρ_e is the space charge density across EDL. ε_0 is the vacuum permittivity.

Two boundary conditions will be applied here: (1) the potential on electrode surface is zero, *i.e.*, $\phi(0)=0$; (2) In the position far away from electrode, there is no potential change in the bulk region of electrolytes, *i.e.*, $\frac{d\phi}{dz} = 0$. Employing the above two boundary conditions, the solution of 1D Poisson Equation[75,76] is shown as below

$$\phi(z) = -\frac{1}{\varepsilon_0}\int_0^z (z-u)\rho_e(u)du - \frac{\sigma}{\varepsilon_0}z \qquad (3.4)$$

u is along the normal direction of electrode. Herein, it is a dummy variable introduced to reduce the double integral to single. This solution is only valid for the planar electrode

surfaces. Since the partial charge $q(i)$ and position of individual atoms are known, the distribution of each atom species along z ($\rho_i(z)$) can be calculated by binning method. The total space charge density is $\rho_e(z) = \sum_i q(i)\rho_i(z)$.

After acquiring the potential distribution $\phi(z)$, the potential drop ϕ_{EDL} can be easily obtained by using the potential near electrode subtracting the potential at the position where no potential fluctuation occurs.

The C-V curve describes the capacitance as a function of potential drop (ϕ_{EDL}) changes. To obtain the C-V curve, multiple independent simulations with varying surface charge densities (σ) will be run, by which a series of the corresponding potential drops across EDL will be acquired. The differential capacitance (C_{d}) is calculated using the following equation

$$C_d = \frac{d\sigma}{d\phi_{EDL}} = \frac{\Delta\sigma}{\Delta\phi_{EDL}} \qquad (3.5)$$

Except the calculation of density profile, C-V curve, in order to better understand the arrangement of cations near electrode surfaces, the orientation ordering parameter will be evaluated as well to analyze the orientational order parameter of rings near electrode surface.

$$P_2(\theta) = \left\langle (3\cos^2\theta - 1)/2 \right\rangle \qquad (3.6)$$

where θ is the angle of a direction vector normal to the ring and the direction normal to electrode surface. $P_2(\theta)$ varies between −0.5 to 1, which estimates the range and extent of the orientation preference of ring near electrode surface.

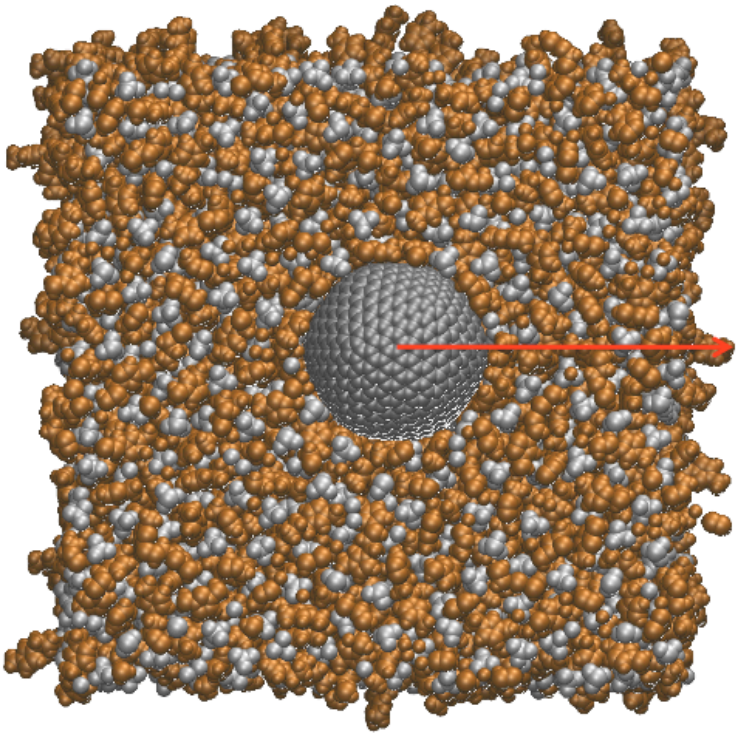

Figure 3.2. Simulation setup for OLC/RTILs-based supercapacitors. The yellow represents cation atoms and white denotes anion atoms.

For spherical carbon electrode, *i.e.*, onion-like carbon (OLC), the supercapacitor system in MD simulation is shown as in Figure 3.2. The curvature effects of electrode on the EDL structure and capacitance of supercapacitors with RTILs as electrolytes have been reported in MD simulations.[66] The curvature is defined by $\frac{1}{R}$, where R is the radius of electrode in this study. For flat graphite, $R = \infty$. All simulations will be run using Gromacs.[77] The size of carbon onion is between 0.35-2 nm in radius. Three-dimension periodic boundary conditions are applied with the carbon onion in the center of the box. The box size should be at least 3 times of the radius of electrodes, since the EDL is in nanometer ranges.

The way to calculate the normalized capacitance of OLC is a little bit different from the simulation using the flat graphite electrode. The space charge density profile is calculated in radial direction ρ_e (r), which is the space charge density distribution as function of the distance between electrode surface and electrolytes in radial direction. The potential drop across EDL will be obtained by solving the spherical Poisson equation as shown in below.

$$\frac{1}{r^2}\frac{d}{dr}(r^2\frac{d\phi}{dr}) = -\frac{\rho_e}{\varepsilon_0} \qquad (3.7)$$

The boundary conditions herein are: (1) $\phi(R)=0$, R is the radius of the carbon onion and (2) at the position far away from the electrode, there is no potential change, *i.e.*, $\frac{d\phi}{dr}=0$. By applying the above boundary conditions, the potential drop can be obtained using the following equation

$$\phi(r) = -\frac{1}{\varepsilon_0}\left[\int_R^r (1-\frac{u}{r})u\rho_e(u)du - \sigma R(1-\frac{R}{r})\right] \qquad (3.8)$$

For carbon nanotube , cylindrical Poisson equation will be applied.

$$\frac{1}{r}\frac{d}{dr}(r\frac{d\phi}{dr}) = -\frac{\rho_e}{\varepsilon_0} \qquad (3.9)$$

Outside the naotube, the boundary condition is (1) $\phi(R)=0$, R is the radius of the carbon onion and (2) at the position far way from the electrode, there is no potential change, *i.e.*, $\frac{d\phi}{dr}=0$.

The potential can be obtained using the following equation[66]

$$\phi(r) = -\frac{1}{\varepsilon_0}\left[\int_R^r u\rho_e(u)\ln\frac{r}{u}du + \sigma R\ln\frac{r}{R}\right] \qquad (3.10)$$

The potential inside the nanotube using different boundary conditions:(1) $\phi(R)=0$, R is the inner radius of the carbon nanotube and (2) at the axis of nanotube, *i.e.*, r=0, $\frac{d\phi}{dr}=0$. Using the boundary conditions, the potential distribution inside nanotube can be obtained as shown in the following equation:

$$\phi(r) = -\frac{1}{\varepsilon_0}\int_R^r u\rho_e(u)\ln\frac{r}{u}du \qquad (3.11)$$

CHAPTER IV

STRUCTRAL ORGANIZATION OF BULK IONIC LIQUIDS

In this chapter, the spatial heterogeneity of bulk ionic liquids is investigated by molecular dynamics simulation. Both monocationic ionic liquids (MILs) and dicationic ionic liquids (DILs) are taken into consideration. Section 4.3 presents a combined MD simulation and small angle X-ray scattering (SAXS) study on the liquid structure of pyrrolidinium-based monocationic ionic liquids, $[C_nMPy][Tf_2N]$. This work has been published in reference 11. Section 4.4 presents a systematic study on DILs 1-alkyl-3-dimethylimidazolium tetrafluoroborate $[C_n(mim)_2](BF_4)_2$ (n=3, 6, 9, 12, 16) in contrast to their monocationic counterparts, which has been published in reference 15. These studies provide a clearer view of the heterogeneous nature in ionic liquids.

4.1 Introduction

Room temperature ionic liquids (RTILs), as promising electrolytes and green solvents, have been widely studied in recent years due to their interesting and unique properties such as negligible volatility, and high electrochemical and thermal stability.[25,78] Recently, 1-alkyl-1-methylpyrrolidinium bis(trifluoromethanesulfonyl)-imide ($[C_nMPy][Tf_2N]$, *n*=3, 4, 6, 8, 10) has been recognized as an interesting class of monocationic ionic liquids (MILs) due to its wider electrochemical window: up to 5.9 V, compared to the more studied $[C_nmim][Tf_2N]$(4.9 V). Also $[C_nMPy][Tf_2N]$ exhibits higher electrochemical stability than $[C_nmim][Tf_2N]$.[79] Presently, only limited studies, especially computational studies, on pyrrolidinium-based ionic liquids have been reported. The X-ray scattering study by Santos *et al.*[80] revealed that long alkyl chain $[C_nMPy][Tf_2N]$ homologs display a first sharp diffraction peak (FSDP) for *n* = 6, 8, and 10, similar to what is observed in

[$C_n$mim][Tf_2N].[44] In that study, the FSDP was attributed to intermediate range ordering arising between the first and second shell neighbors of the asymmetric ions. Additionally, the shift of structural peaks towards larger distances with increased temperature has been discussed by Santos *et al.,*[80] but the temperature dependence of the low-*Q* peak for [C_nMPy][Tf_2N], which exhibits the opposite trend demonstrated in the new experimental data in this paper, has not been previously reported. However, a corresponding computational study of [C_nMPy][Tf_2N] has not been reported, and it would be of interest to see whether the reported heterogeneity probed by FCS can be also observed using MD simulation and other experimental methods. Section 4.3 presents a combined MD simulation and SAXS study on the liquid structure of pyrrolidinium-based monocationic ionic liquids, [C_nMPy][Tf_2N]. Self-aggregation of non-polar alkyl chains appear clearly in long chain [C_nMPy][Tf_2N] ionic liquids, and the resulting alkyl chain-dependent polar group ordering, provides a clearer view of the heterogeneous nature of ionic liquid structures.

In spite of a remarkable increase in the number of RTILs reported, a majority of RTILs under investigation are monocationic ionic liquids (MILs), *i.e.*, having monovalent cations. It has been suggested that the physical and chemical properties of RTILs are mainly determined by the anion due to its diversity whereas most cations are structurally similar and thus exert less influence on RTIL properties.[81] To expand the diversity of the cation family, a series of imidazolium- and pyrrolidinium-based geminal dicationic ionic liquids (DILs)[82,83] with cations consisting of two identical imidazolium or pyrrolidinium rings linked together by alkyl chains of different lengths. In contrast to cations in MILs, each dication in DILs carries two positive unit charges and it is structurally symmetrical

in most cases. Moreover, subsequent studies reported that DILs, similar to MILs, can be used equally well as catalysts,[84-87] solvents,[88] lubricants[89,90] and electrolytes,[91,92] especially at high temperatures due to their high stability.[83]

Although the structural and physicochemical properties of MILs have been extensively studied[25,27,93,94] and several studies on DILs have been reported,[95-98] the spatial heterogeneity of DILs has yet to be fully explored. The nanoscale organization of MILs has been comprehensively investigated using small/wide angle X-ray (SAXS/WAXS),[7,37,99] small angle neutron scattering (SANS)[8] and a variety of theoretical simulations.[38,40,100] The physical significance of the "prepeak" or "FSDP" observed at the low-Q range in the structure functions of MILs with long alkyl chains from both experimental and theoretical work has been debated for decades. Recently, partly as a result of simulation studies, a consensus is emerging that the prepeak is a result of the correlations between anions that are separated by the aggregated long alkyl chains and thus corresponds to anion-anion correlations beyond the first nearest neighbor shell. The intensity of the prepeak mostly depends on the types of anions whose constituents usually have large X-ray form factors in comparison to the cation alkyl chains.[101] However, relevant studies on this issue have not been reported for DILs. Does linkage chain length impose the same influence on the structural arrangement of DILs as the free alkyl chain in MILs? Do DILs exhibit structural heterogeneity similar to that observed in MILs? What role does the anion play in the structure of DILs? Some answers have been obtained in simulation studies by Ishida[102] and Bodo *et al*.,[103] in which they reported that the increase of linkage chain length results in the emergence of a prepeak at low-Q range

in the structure function for DILs. However, the majority of the aforementioned issues are still inviting in-depth exploration.

In Section 4.4, a systematic study on DILs 1-alkyl-3-dimethylimidazolium tetrafluoroborate $[C_n(mim)_2](BF_4)_2$ (n=3, 6, 9, 12, 16) was performed using MD simulation. The effects of the linkage chain length on the nanoscale organization of DILs were analyzed in comparison with those of the free alkyl chain length in MILs. The structural heterogeneities resulting from the assembly of long linkage chains in DILs were derived and compared with those formed by long alkyl tail chains in MILs. Moreover, the BF_4- anions were replaced with different alternatives (Br- and PF_6-) for short- and long-chain dications and monocations, respectively, in order to study the influence of anion type on the nanoscale ordering. Based on these insights, The idealized structural models are propsed for nanoaggregates formed by the alkyl chains of DILs and MILs that provide a basis for understanding the dissimilarities in the nanoscale segregation of DILs and MILs.

4.2 Simulation Details

The all-atom force field for $[C_nMPy][Tf_2N]$ used in the simulation was transferred from APPLE&P potential (Atomistic Polarizable Potential for Liquids, Electrolytes, & Polymers) developed by Oleg Borodin.[104] All parameters were transferred to exp-6 force field without any alteration except that the polarizability term was excluded from the potential.[105] The partial charges of carbon groups beyond the fourth carbon near the pyrrolidium ring were all set to zero except the terminal methyl group. The force field used for dicationic $[C_n(mim)_2](X)_2$ (n=3, 6, 9, 12, 16 and X=Br-, BF_4-, PF_6-) was adapted from the all-atom force field developed by Yeganegi *et al.,*[106] which has been validated

and used to predict the densities of DILs with high accuracy compared with experimental data.[83] The force field for monocationic $[C_n mim][X]$ (n=3, 6, 9 and X=Br-, BF_4-, PF_6-) was taken from the study by Lopes' group.[107] All the hydrogen bonds were constrained during the simulation using the LINCS algorithm.[108] Long-range electrostatic interactions were processed using the particle mesh Ewald (PME) method.[109] Periodic boundary condition (PBC) was applied in three dimensions. All simulations were performed using MD package Gromacs.[77] The cubic simulation box was sufficiently equilibrated at 1 bar after energy minimization followed by a 4-ns production run. A linear mean square displacement and the density without significant variation confirmed the equilibrium state of the simulation box. Timesteps of 1 fs were adopted. The Nosé-Hoover thermostat and Parrinello-Rahman barostat were used respectively for the temperature coupling and pressure coupling. To investigate the temperature influence on the structural organization of $[C_n MPy][Tf_2N]$, the simulations were completed using the above protocol in the isothermal-isobaric ensemble at 1 bar and 298 K, 348 K and 363 K respectively.

Due to the high melting point (~400K)[83] of DILs $[C_n(mim)_2](X)_2$, all the simulations were performed at 450 K rather than room temperature to ensure that all ionic liquids are in liquid phase. The equilibrated box size is in the 8-10 nm range, which is sufficiently large to accurately represent the low-Q peaks above 0.15 $Å^{-1}$ in the structure function. A 2-ns production run generated at 1 bar and 450 K was used for further analysis. The total static structure factors were calculated using Eqn. 1.[72]

The heterogeneity order parameter (HOP) was calculated as well to quantify the effect of the increased alkyl chain on the spatial heterogeneity of DILs and MILs. The following equation is used for the HOP calculation,[39,110]

$$h = \frac{1}{N_s}\sum_{i=1}^{N_s}\sum_{j=1}^{N_s}\exp(\frac{-r_{ij}^2}{2\sigma^2}) \qquad (4.1)$$

where N_S is the total number of sites in system, r_{ij} is the distance between site i and j corrected by periodic boundary conditions, and $\sigma = \frac{L}{N_s^{1/3}}$ with L the length of the cubic simulation box. From equation 2, it is indicated that the value of h increases as the spatial heterogeneity is enhanced, because the tighter packing of sites results in the smaller r_{ij}, which leads to a larger h.

4.3 Monocationic Ionic Liquids $[C_nMPy][Tf_2N]$

4.3.1 Influence of Chain Length on Spatial Heterogeneity

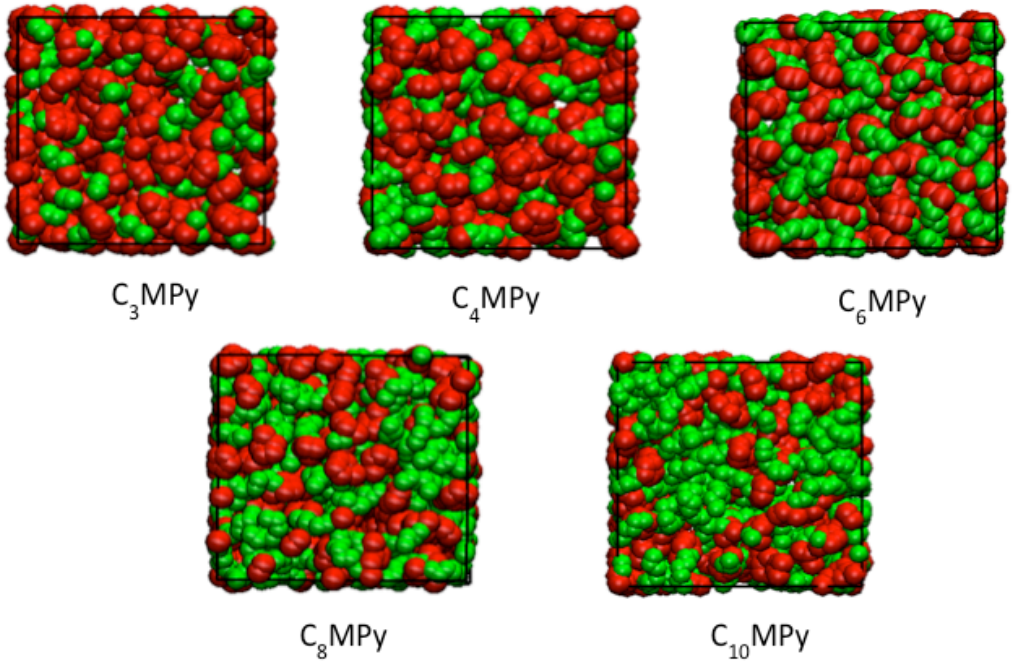

Figure 4.1. Snapshots of a series of ionic liquids $[C_nMPy][Tf_2N]$. Red atoms indicate the charged pyrrolidinium ring. The alkyl chains are shown as green.

The snapshots for $[C_nMPy][Tf_2N]$ are shown in Figure 4.1. It is clear that the tail groups aggregate and form several spatially heterogeneous domains. The domains grow larger with increasing alkyl chain length of the cationic $[C_nMPy]^+$. The intermolecular center of mass (COM) site-site radial distribution functions (RDFs) were calculated as shown in Figure 4.2 Initially, we assumed the cations would assemble through tail aggregation in $[C_nMPy][Tf_2N]$ as the alkyl chain length was increased, similar to the phenomenon reported in imidazolium-based ionic liquids. Surprisingly, the calculated cation-cation RDF decreases with increasing *n*, while the peak shifts to longer distances (Figure 4.2a). These results suggest that a longer alkyl chain does not cause cation aggregation. On the contrary, the cations are more spatially separated as *n* was increased. This is possibly due to the shift of cation COM. With increasing alkyl chain length, the COM is shifted towards the alkyl chains. Nevertheless, the length of the side alkyl chain of the cation does not affect the anion-anion radial distribution (Figure 4.2b). The cation-anion RDF is greatly decreased with increasing *n* (Figure 4.2c). To exclude the effects of the alkyl chain on the COM of the cation, we calculated the RDF of the pyrrolidinium ring relative to the COM of the anion. An opposite trend, in which the correlation of ring-anion increases with increased alkyl chain length, was observed (Figure 4.2d). This phenomenon agrees with Margulis' report on imidazolium-based ionic liquids.[40]

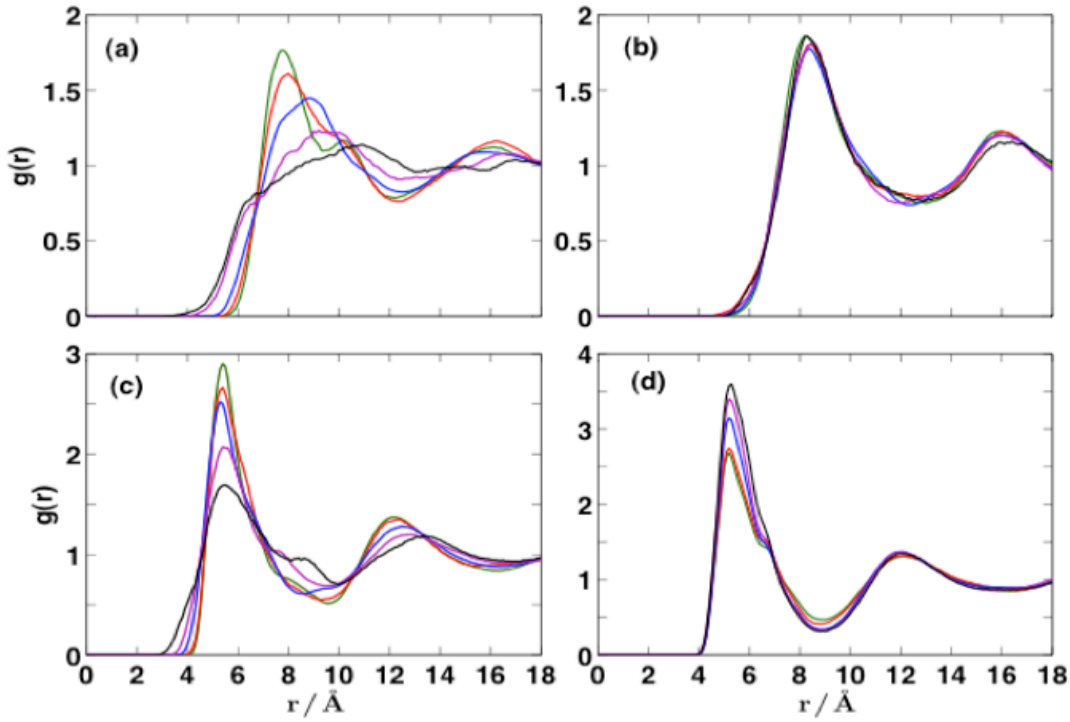

Figure 4.2. Center of mass radial distribution functions at 298 K of a) cation-cation b) anion-anion c) cation-anion and d) pyrrolidinium ring-anion for *n*=3 (green), 4 (red), 6 (blue), 8 (purple) and 10 (black).

The RDF of the alkyl side-chain terminal carbon is typically the most direct evidence of alkyl tail aggregation. However, no evident differentiation among $[C_6MPy]^+$, $[C_8MPy]^+$ and $[C_{10}MPy]^+$ was observed (Figure 4.3), in contrast to reports on imidazolium-based ILs.[38,40] Although the RDF of the terminal carbon does not clearly show the expected behavior, the coordination number increases as n increases, from 3 for *n*=3 to 6.8 for *n*=10, which indicates the enhancement of aggregation behavior.

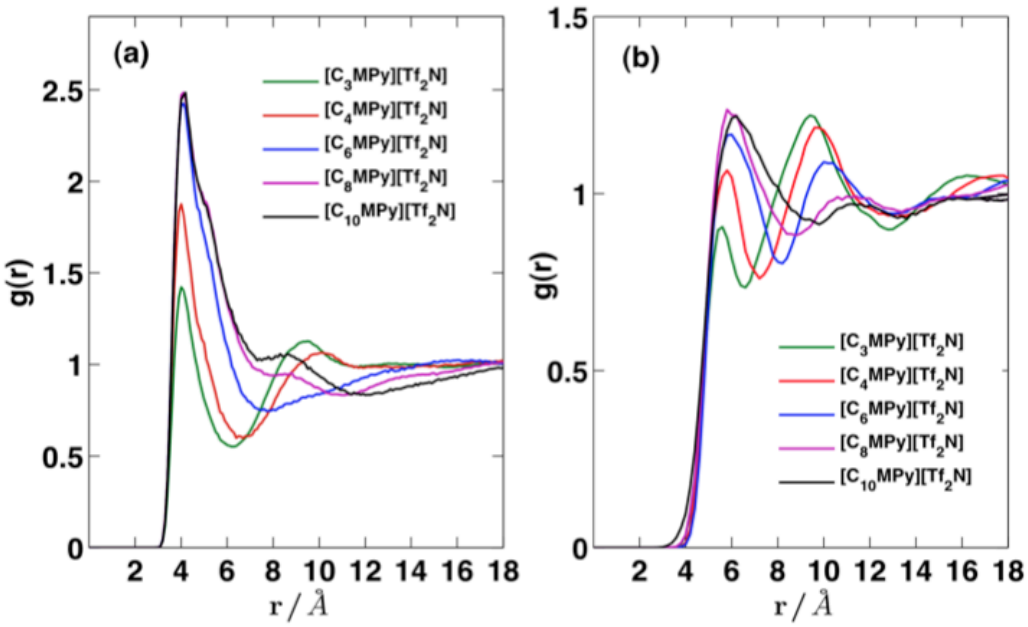

Figure 4.3. Center of mass radial distribution function at 298 K of a) terminal carbon b) alkyl chain.

To further explore the effects of alkyl chain length on the liquid structure of $[C_nMPy][Tf_2N]$, the structure function $S(Q)$ of all five ILs was calculated and compared with SAXS results, as shown in Figure 4.4a. For scattering at low values of wave vector transfer in ionic liquids, sources of higher electron density are needed in order to provide good X-ray contrast. The cation ring and the corresponding anion in $[C_nMPy][Tf_2N]$ are closely bound, forming a polar group in the ionic liquid that provides excellent X-ray contrast with neighboring alkyl chains. SAXS provided information with a 0.01–2.8 $Å^{-1}$ Q-range, covering both intermolecular as well as large-scale intramolecular length scales.

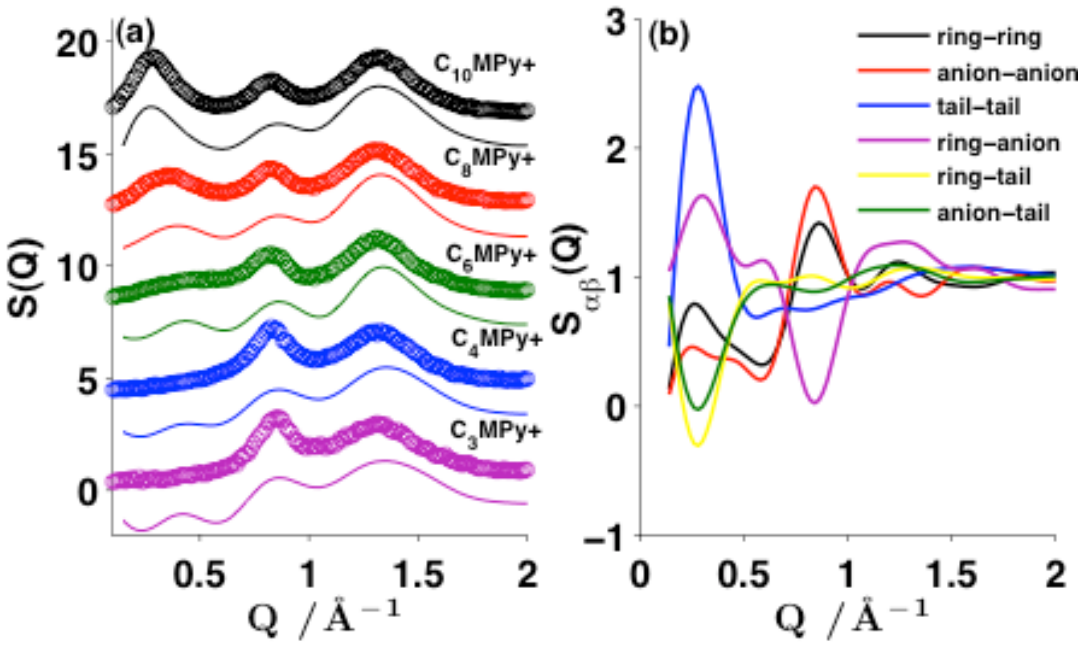

Figure 4.4. (a) Structure functions for *n*=3, 4, 6, 8, 10 [C_nMPy][Tf_2N] measured at room temperature. Open symbols in varying colors represent SAXS results; the solid lines with corresponding colors represent MD calculated results; (b) Partial structure functions contributed by varying site-site correlations of [C_{10}MPy][Tf_2N] calculated from MD simulation at 298 K. Here the ring is defined as the center of mass of the pyrrolidinium ring; the tail is defined as the terminal carbon of alkyl chain.

Three peaks were observed as shown in Figure 4.4a; for example, for *n*=10, peaks occur near 1.35, 0.8 and 0.3 Å^{-1}. Figure 4.4b is the unweighted partial structure functions for *n*=10 calculated by Fourier transformation of corresponding MD-generated site-site RDFs of [C_nMPy][Tf_2N]. We first consider the peak near 1.35 Å^{-1}, corresponding to the real space distance of $2\pi/1.35 = 4.65$ Å, which is close to the ring-anion correlation. Figure 4.4.b explicitly shows that the strongest contribution to the peak near 1.35 Å^{-1} is from the ring-anion correlations, which is consistent with Aoun's computational result on

[$C_n$mim+][8,111] and Santos' X-ray scattering study on [C_nMPy][Tf_2N].[80] We now consider the two peaks near 0.8 $Å^{-1}$ and 0.3 $Å^{-1}$. Peaks that arise at low-Q values, or FSDPs, are a prominent feature in network glasses and typically interpreted as a sign of intermediate range order.[100,112-115] Two main trends are immediately evident from observation of $S(Q)$ within $Q < 1$ $Å^{-1}$. First, a strong alkyl chain-dependent FSDP (see Figure 4.4.b) occurs (clearly defined at ~0.29 $Å^{-}$ for n=10). This FSDP drops in intensity and shifts toward higher Q (0.36 $Å^{-1}$ for n = 8 and 0.47 $Å^{-1}$ for n = 6) and decreases in intensity as the alkyl chain length is shortened so that its contribution at n=4 and n=3 is weak as shown in Figure 4.5.b. Second, Figure 4.4.b shows that at 0.8 $Å^{-1}$, corresponding to a real space distance of 7.8 Å, positive contributions from the cation ring-ring and anion-anion correlation, along with a negative contribution from the cation ring-anion correlation are present. This is similar to what has been observed in imidazolium-based ionic liquids[116] with Cl and PF_6 anions and is a clear sign of the charge ordering in this system.

Figure 4.2 shows the deep valley in the cation-anion real space correlation function (Figure 4.2c) that corresponds to the distance between the like-charged species (Figure 4.2a). Since the peak near 0.8 $Å^{-1}$ in Figure 4.4a does not change in position substantially as the alkyl chain length is decreased, it appears that the low-Q peak near 0.3 $Å^{-1}$ merges with the second polar group peak near 0.8 $Å^{-1}$ noted by the slight yet systematic increase of the second peak's intensity as the chain length is decreased. These low-Q features can provide insight into the large-scale organization of the [C_nMPy][Tf_2N] system.

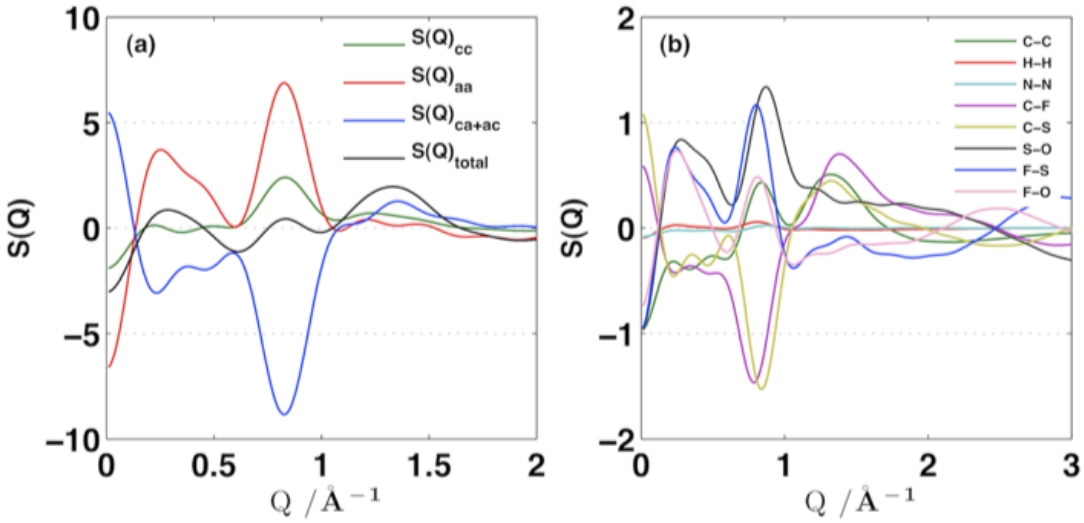

Figure 4.5. (a) X-ray weighted subcomponents of $S(Q)$ contributed by cation-cation, cation-anion and anion-anion correlations compared with total structure function at 298 K of $[C_{10}MPy][Tf_2N]$; (b) X-ray weighted atomic subcomponents of $S(Q)$ in $[C_{10}MPy][Tf_2N]$.

The X-ray-weighted subcomponents of partial structure function contributed by cation-cation, cation-anion and anion-anion correlations (Figure 4.5a) were calculated using Santos's method.[46] As reported by Annapureddy *et al.*[116] for imidazolium-based RTILs, our results suggest that anion-anion correlations contribute positively to the positive FSDP and the second peak located at 0.8 $Å^{-1}$. Negative contribution to the peaks result from the cation-anion correlation. The atomic partial structure factor was then calculated as shown in Figure 4.5b, which demonstrated that the positive FSDP was mainly from cross-atom correlations in anions. However, carbon-carbon and hydrogen-hydrogen correlations barely contribute to the structure function. These findings are in agreement with our above analysis.

The results of several experimental and computational investigations have been recently combined by Annapureddy *et al.*[116] Their study identifies the origin of the pre-

peak in imidazolium-based ionic liquids and offers a way to describe liquid-state structural observations based on observed crystallographic ordering. Although the crystalline and liquid states are not the same, this approach nevertheless helps to understand the scattering measurements. A similar approach is used here to describe the alkyl chain-dependent experimental observations in our pyrrolidinium system. We define I_E as the structural peak corresponding to the nearest neighbor polar group separation, which is primarily governed by electrostatic interactions, and I_A as corresponding to the alkyl chain-separated polar group distance.

Analysis of the peak positions and intensities in the SAXS data for $Q < 1$ Å^{-1} for the series in this study yield some interesting trends. These were obtained by fitting two Gaussian functions with a quadratic baseline, in a manner similar to other studies,[115,116] which fit the data well. The peak positions for samples with n=6 to n=10 lie on a line with a slope of 2 Å per CH_2 group. The low-Q peak I_A centers for n =3 to n=10 convert to real space values between 8.8 and 22 Å, respectively, corresponding to the peaks lying on a line of slope (22 Å - 8.8 Å)/7 = 1.9 Å per CH_2 group; focusing just on samples with n=6 to n=10, the slope is 2 Å per CH_2 group. Hence, the measured alkyl chain-separated polar group distance for a given n is less than twice that of an all-trans n-alkyl chain for all the ionic liquids. This suggests some level of interdigitization[116] or coiling of the alkyl chains, especially for the longer alkyl chain liquids. The low-Q I_A peak contribution is clearly visible for n = 10 and 8 but less obvious for n = 6, 4 and 3. From the low-Q I_A peak analysis we obtain peak positions corresponding to distances of 13.3 Å, 9.6 Å and 8.8 Å for n = 6, 4, and 3, respectively for the alkyl-chain separated polar group distance. As the alkyl chain length decreases, it is clear that this dimension approaches the near-

neighbor polar group separation distance of 7.8 Å (*i.e.*, I_E peak), which shows no significant alkyl chain length dependence. Thus, the I_E peak at 0.8 $Å^{-1}$ shows a systematic increase in intensity with decreasing alkyl chain length, while the low-Q I_A peak is diminished. These observations are consistent with previous reports on the alkyl chain length dependence of the low-Q scattering in imidazolium-based RTILs.[8,116]

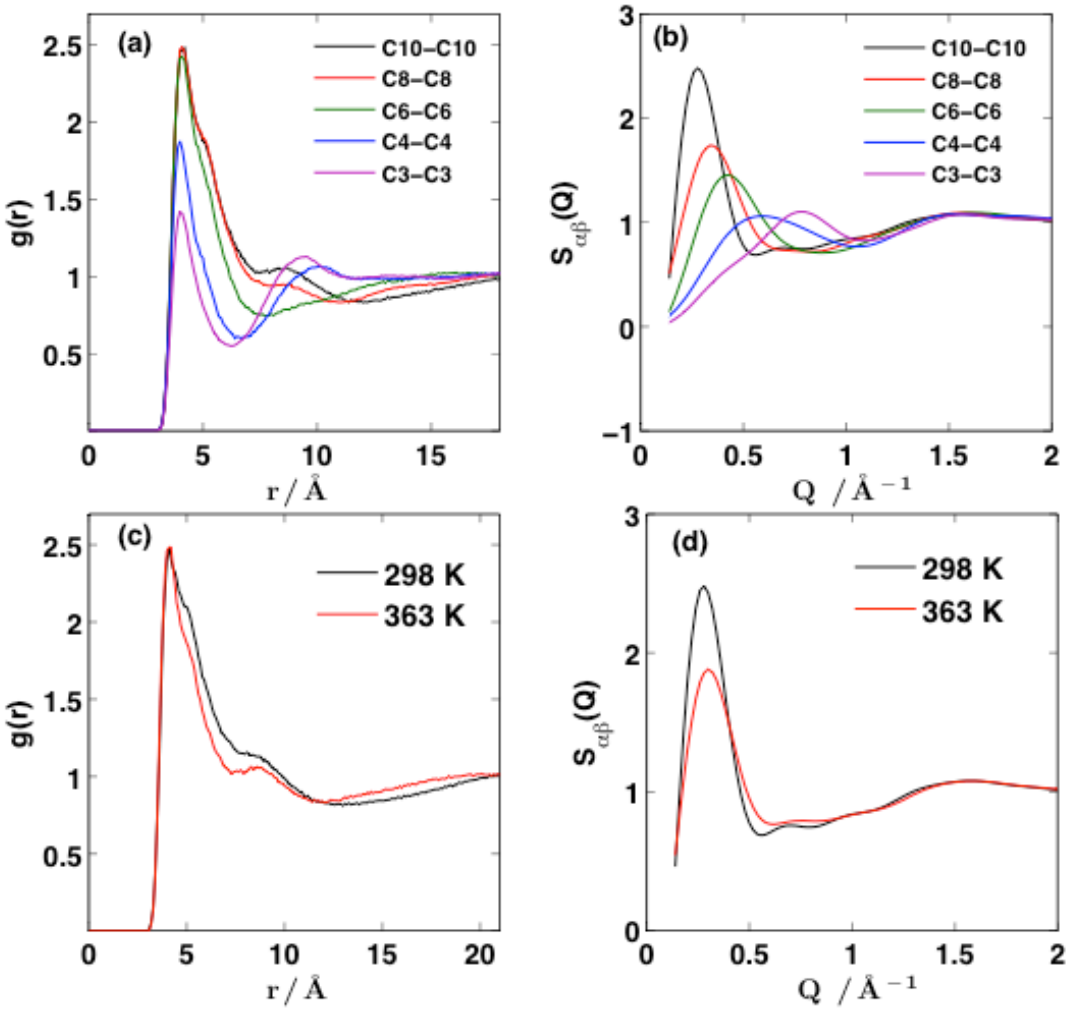

Figure 4.6. (a) Tail-tail correlation functions of $[C_nMPy][Tf_2N]$;(b) The corresponding partial structure functions of (a); (c) Tail-tail correlation functions of $[C_{10}MPy][Tf_2N]$ as a function of temperature; (d) The corresponding partial structure functions of (c) calculated at 298 and 363 K respectively.

Figure 4.6b shows that the tail-tail correlations contribute to the FSDP especially for longer chain $[C_nMPy][Tf_2N]$. The main peak in the tail-tail partial structure functions coincides with the peaks of other partials involving the anions, cations, and tails, and while other correlations play a dominant role due to their electronic weights as shown in Figure 4.5, it is nevertheless present and plays a role in the organization of the charged species in the system. The contribution of tail-tail correlations to I_A is smaller for $n < 6$ and the peak position shifts to higher Q with a decrease in n. These results show that longer alkyl chains greatly favor tail-tail assembly as reported in the fluorescence correlation spectroscopy (FCS) experiments.[117] For chain length $n < 6$, the alkyl chain van der Waals forces cannot overcome the electrostatic forces to exhibit closer association.

4.3.2 Temperature Effects

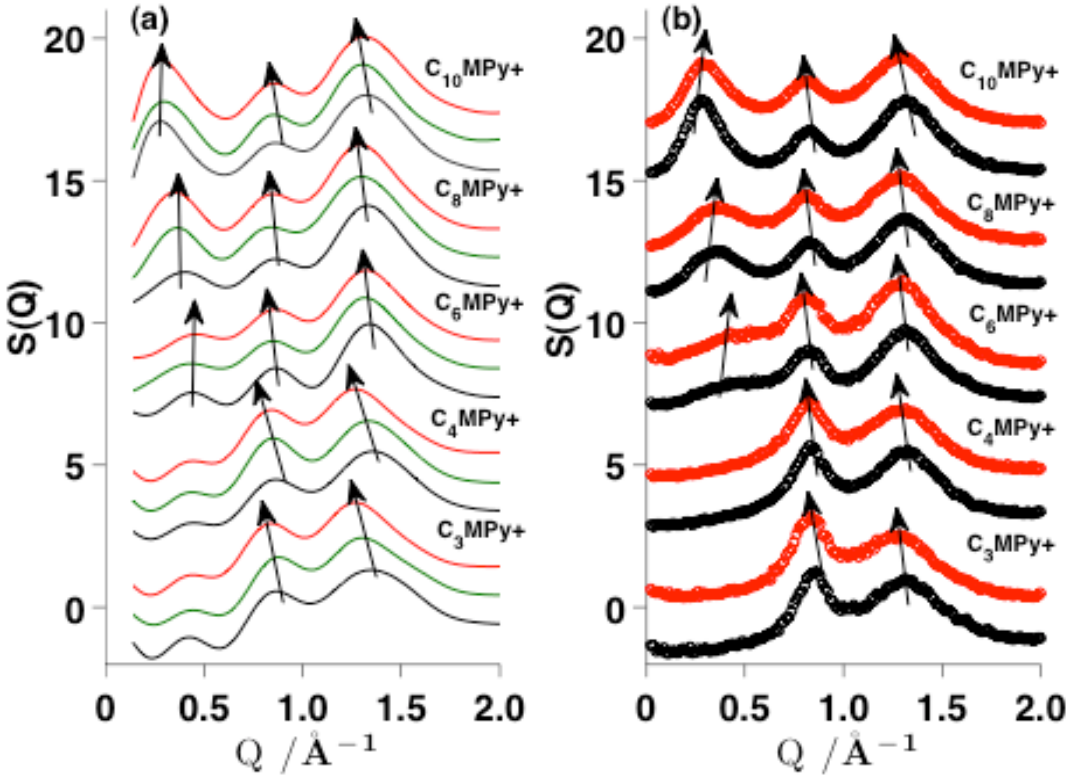

Figure 4.7. MD (a) and SAXS (b) curves showing the temperature dependence of structure factors for $[C_nMPy][Tf_2N]$. Black symbols denote MD/SAXS results at 298 K, green symbols denote MD/SAXS results at 348 K and red denote MD/SAXS results at 363 K. The curves have been offset vertically for clarity. The second and third peaks shift toward lower *Q*-values as the temperature is increased, however, the alkyl chain-separated polar group peak shifts towards higher *Q* with increasing temperature for $n = 6$, 8, and 10.

The temperature effects on the structure functions of $[C_nMPy][Tf_2N]$ obtained from both simulation and SAXS are shown in Figure 4.7. It is common to observe broadening of diffraction peaks as the temperature is raised in a liquid.[118-120] The shift of diffraction peaks to lower *Q* values is a feature that correlates with a density decrease[80] as intra- and intermolecular distances increase. These observations hold for the current series under investigation, with the exception of the alkyl chain-dependent peak, I_A. For $n = 8$ and 10, there is a clear shift of this FSDP to higher *Q* with increasing temperature (Figure 4.7). For $n = 3$, 4 and 6, this effect, if present, is very slight.

The work reported by Triolo on $[C_nmim][BF_4]$ with $n = 3$-10 exhibits a similar trend in the supercooled liquid in the range from 90 to 290 K.[45] For temperatures above the glass transition, T_g, they attribute a spatial correlation decrease with increasing temperature to diffusion, and when diffusive processes are arrested below T_g, then the peak shift is strictly related to density changes. In order to reveal the temperature effects on the FSDP position, the temperature-dependent tail-tail correlation was analyzed. Figure 4.6c displays calculated tail-tail correlations for $[C_{10}MPy][Tf_2N]$ at varying temperatures, and the corresponding *S*(*Q*)s in Figure 4.6d. As the temperature was raised, the FSDP shifted

to higher Q; no significant change in the 1st and 2nd neighbor position occurs, but an increase in the ordering between the tails does occur as indicated by the narrowing in the correlation peak. Also, the tail-tail coordination number calculated by integration of its correlation from 0 to 12 Å decreased from 11.6 at 298 K to 10.8 at 363 K, which may be crucial for an understanding of the temperature-dependent FSDP shift.

The following is an interpretation of our observations. Because of the increased interaction between alkyl chains as the chain length is increased (shown in the present simulation, Figure 4.6), the alkyl chains play a significant role in the ordering of the liquid. There is, in effect, competition between the strong charge ordering of the ions and the weaker van der Waals influence of the alkyl chains. At ambient temperatures, the van der Waals interactions are stronger for the long alkyl chain liquids and increase chain association. However, at higher temperatures, the van der Waals interactions are reduced and the polar group electrostatic forces dominate. At higher temperatures it is more likely for a cation tail to diffuse[45] from its non-polar aggregate, thus resulting in a decrease in the aggregate size shown by the slight shortening of the alkyl chain-separated polar group distance (Figure 4.7). The diffusion step is necessary to preserve first neighbor ionic distances, since they are dependent on the density rather than the temperature. This reduction in aggregate size will result in shorter chain aggregate correlation distances, indicated by the shift to higher Q values in the tail-tail partial $S(Q)$ (Figure.4.6b).

MD simulations, as shown in the snapshot at 4 ns (Figure 4.1) and the RDFs (Figure. 4.6b), clearly demonstrate that the aggregation size increases with increasing alkyl chain length, consistent with our FCS findings.[117] The FCS results showed evidence for self-aggregation domains for $[C_3mpy][Tf_2N]$ and SAXS experiments show evidence of the

existence of an alkyl chain-dependent weak polar group ordering, I_A, for n = 3 and 4. MD simulations suggest the averaged aggregation size for $[C_3MPy][Tf_2N]$ is ~ 3 alkyl chains. All the techniques unambiguously show the self-aggregation for $n > 4$.

Structural heterogeneity in ILs has been a subject of considerable attention in the past few years. It has been reported that long chain $[C_nmim+]$ ($n > 12$) systems or alcohols can form micelle-like structures easily. The self-aggregation of mid-range alkyl chain $[C_nmim+]$ systems was first suggested by MD simulations from Voth *et al*.[38] and supported by SAXS from Triolio *et al*.[37,45] Hardacre and coworkers[8] called the meaning of the FSDP peak into question through well-designed SANS experiments based on selectively H/D-isotopically substituted $[C_nmim+]$ systems. Other experimental evidence, such as the observation of pronounced "hyperpolarity", biphasic diffusion dynamics observed using FCS, as well as rotational dynamics probed by optical heterodyne-detected Raman-induced Kerr effect spectroscopy,[44] point to self-aggregation, or locally ordered domains/structures, or microphase separation of ionic liquids. The results from our MD simulation support the aggregation of alkyl chains in $[C_nMPy][Tf_2N]$, as evidenced by the snapshot in Figure 4.1. The SAXS measurements in turn highlight the ordering of the polar groups that result from both electrostatic ion ordering at short distance and the complex alkyl chain interactions at further distances. More carefully designed SANS experiments with different H/D-isotropically exchanged $[C_nMPy][Tf_2N]$ as well as rotation dynamics of dyes in $[C_nMPy][Tf_2N]$ probed by fluorescence anisotropy spectroscopy will be reported elsewhere.

4.4.3 Conclusion

In Summary, molecular modeling and small angle X-ray scattering were applied to elucidate the alkyl chain length and temperature effects on the nanoscale organization of pyrrolidinium-based ionic liquids. For the first time, we demonstrated that the cation tails of pyrrolidinium-based ionic liquids with long alkyl chains exhibit aggregation behavior, which is analogous to imidazolium-based ionic liquids. The alkyl chain segregation is attributed to electrostatic interactions between polar groups and van der Waals forces of the nonpolar alkyl chains.

4.4 Dicationic Ionic Liquids

4.4.1 Chain Length Effects on Dicationic $[C_n(mim)_2](BF_4)_2$

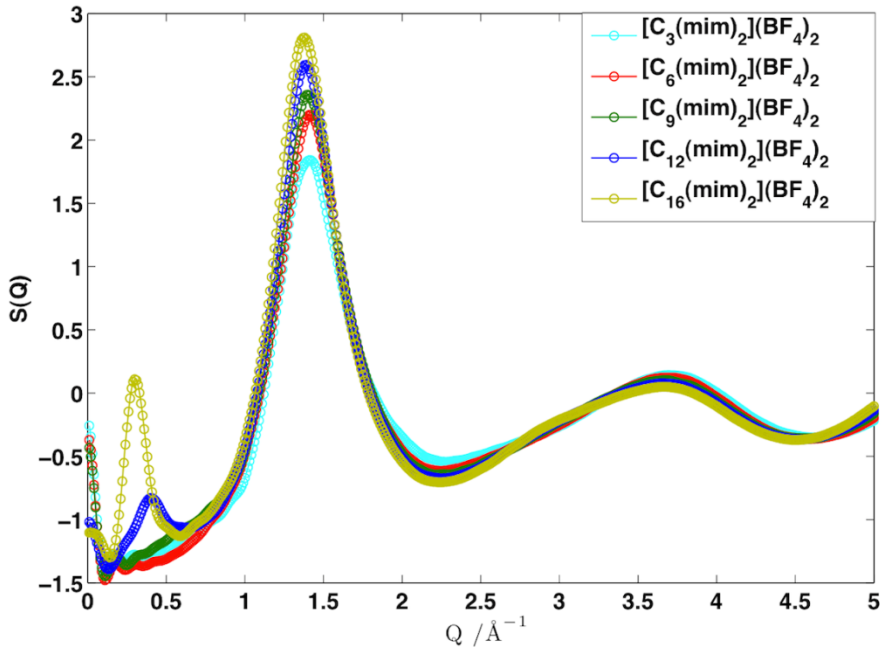

Figure 4.8. Total static structure factor for dicationic $[C_n(mim)_2](BF_4)_2$ (n=3, 6, 9, 12, 16).

The calculated total static structure factors for DILs $[C_n(mim)_2](BF_4)_2$ are shown in Figure 4.8, based on which two findings should be noted. First of all, the intensity of the

peak at approximately 1.4 $Å^{-1}$ increases with the elongation of the linkage chain length and shifts to low-Q range. According to previous studies of MILs,[11,121,122] the peak located at 1.4 $Å^{-1}$ is mainly due to the interaction between co-ions, that is, cation-cation or anion-anion interactions. The chain-length-dependent increase of the peak intensity implies a strengthened correlation between co-ions and the peak shift toward low-Q range corresponds to the increased distance between co-ions. The partial structure factors shown in Figure 4.9 reveal that the peak located at 1.4 $Å^{-1}$ in Figure 4.8 mainly results from the cation-cation correlations (Figure 4.9a), which displays the enhanced peak intensity as well as shifted peak positions toward low-Q as the linkage chain length increases from C3 to C16. By focusing on subcomponents (*i.e.*, the head and chain in the dication) of the cation-cation correlation as shown in Figure 4.9e-f, we see that the increased intensity of the peak at 1.4 $Å^{-1}$ is dominated by the linkage chain-chain correlations (Figure 4.9f). The enhanced chain-chain interaction is also confirmed by the radial distribution functions (RDFs) of linkage chains. The first peak of the chain-chain RDF increases significantly with increasing linkage chain length. The other phenomenon noticed at the low-Q range is the rise of the prepeak located at 0.3 $Å^{-1}$ as the chain length increases, which is similar to that observed in MILs with long alkyl tails.[11,37,45,111,121,123]

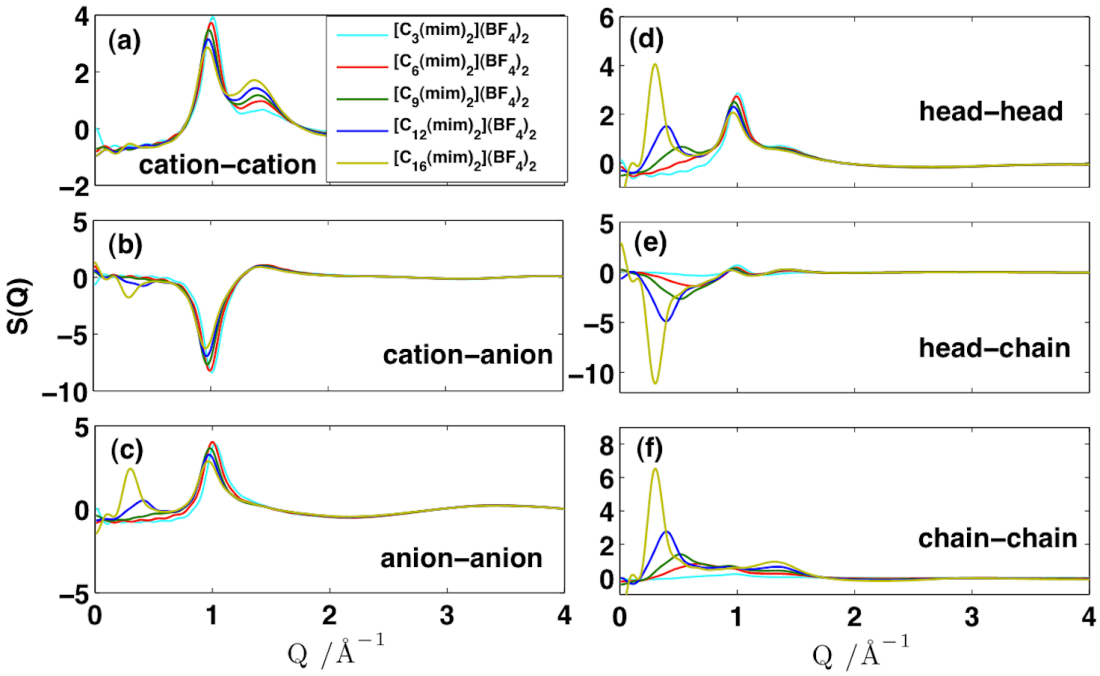

Figure 4.9. Structure functions of $[C_n(mim)_2](BF_4)_2$ (n=3, 6, 9, 12, 16) contributed by cation-cation (a), cation-anion (b) and anion-anion (c) correlations and the cation head-head (d), head-chain (e) and chain-chain (f) subcomponents of cation-cation correlations for $[C_n(mim)_2](BF_4)_2$.

Figure 4.9c verifies that the presence of prepeak is mainly attributed to the anion-anion correlation, similar to the conclusion drawn from studies on MILs.[101,124] Although Figure 4.9f presents the enhanced chain-chain interactions as chain length increases, the chain-chain interactions do not contribute to the increased prepeak intensity directly. Nevertheless, the increased alkyl chains occupy more space, which leads to the enhanced anion-anion correlations and eventually the presence of the pepreak. Moreover, the aggregate composed of long linkage chains is shown in the snapshots of Figure 4.10, suggesting that DILs as well as MILs manifest enhanced structural heterogeneity with the elongation of chain length. Based on the above findings, it seems fair to conclude that the

increased linkage chain in DILs plays the similar role as the alkyl chain in MILs. However, there are significant dissimilarities in the nanoscale structure between DILs and MILs as the elongation of the chain length. Based on visual inspection of Figure 4.10, it is apparent that the aggregate sizes formed in MILs ($[C_6mim][BF_4]$ and $[C_8mim][BF_4]$) are larger than those in DILs ($[C_{12}(mim)_2](BF_4)_2$ and $[C_{16}(mim)_2](BF_4)_2$). It is worthwhile to note that in this work, to compare chain length effects on the structural segregation of DILs and MILs in a rigorous way, MILs with varying alkyl tail lengths are chosen, where each alkyl tail chain length corresponds to one half of the linkage chain length in DILs (*i.e.*, $[C_nmim][BF_4]$ (n=3, 6, 8) versus $[C_n(mim)_2](BF_4)_2$ (n=6, 12, 16)).

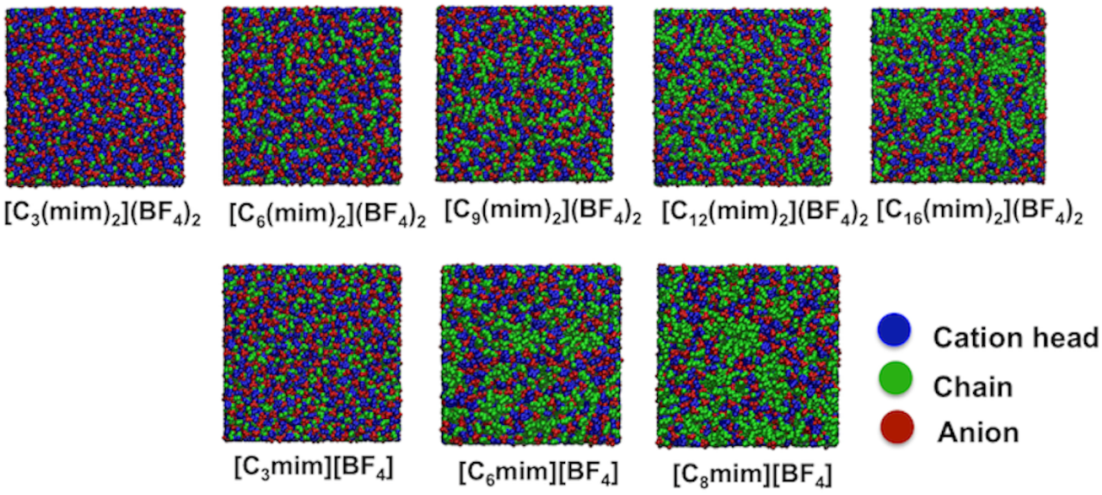

Figure 4.10. Snapshot of MD simulation of bulk dicationic $[C_n(mim)_2](BF_4)_2$ (n=3, 6, 9, 12, 16) and monocationic $[C_nmim][BF_4]$ (n=3, 6, 8). Cation head represents the imidazolium ring with its connected methyl group and the remainder is classed as the chain.

To quantify the spatial heterogeneity observed in Figure 4.10, the HOP for both DILs and MILs were calculated and shown in Figure 4.11. According to the study by Voth's group,[39] the HOP value for homogenously distributed ideal particles is ~15.74. All the

HOPs shown in Figure 4.11 are above 15.74, indicating the heterogeneous system for both DILs and MILs. Moreover, the HOP value increases with the elongation of the alkyl chain length in both DILs and MILs, indicating the increased structural segregation as chain length increases. This trend is in agreement with previous reports on MILs.[39,110] Nevertheless, the alkyl chains of MILs exhibit much larger HOP values compared with those in DILs, implying the higher degree of alkyl chain aggregation in MILs, which is evident by visual inspection of the snapshots shown in Figure 4.10. In addition, it is noteworthy that the alkyl chains of MILs display the highest HOP values compared with anions and head groups, whereas in DILs, the head groups exhibit the largest HOP, which underscores the fundamental structural differences between DILs and MILs. However, on average, the HOPs for DILs are dramatically lower than those of MILs.

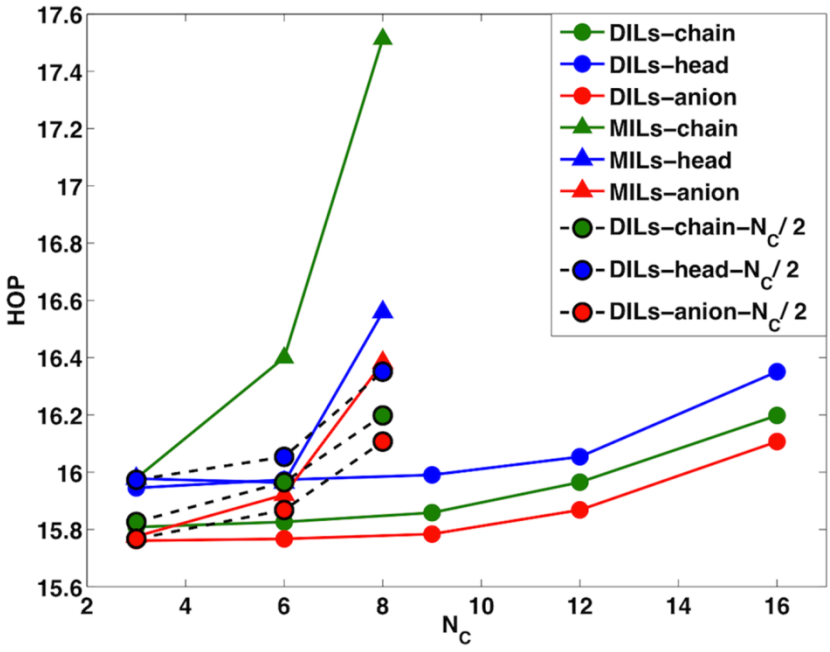

Figure 4.11. Heterogeneity order parameter (HOP) for alkyl chains (green), head groups (blue) and anions (red) of DILs (solid circles) and MILs (solid triangles) as a function of chain length (N_C, the number of -CH_2 in alkyl chain). The solid circles with black dash

lines are HOP values of DILs with N_C =N/2 (N= 6, 12, 16, N is the number of -CH_2 in alkyl chain of DILs). The carbon atom in the end of alkyl tail chain of MILs and the carbon atoms in the middle of linkage chain for DILs represent the alky chain site (for the even-numbered DILs, the site is defined as the center of mass of the two central carbon atoms in an alkyl linkage chain); the center of mass of head groups and anions were used to denote the anion sites and head sites, respectively.

To understand the different heterogeneities between DILs and MILs, the structural discrepancy between DILs and MILs is also analyzed through their total static structure functions shown in Figure 4.12. It is observed that for short-chain dicationic $[C_6(mim)_2](BF_4)_2$ and monocationic $[C_3mim][BF_4]$, almost the identical structure functions are present, both of which exhibit only one peak located at 1.4 $Å^{-1}$. For chain lengths in the medium-range ($[C_{12}(mim)_2](BF_4)_2$ versus $[C_6mim][BF_4]$), the discrepancy in prepeaks at 0.3 $Å^{-1}$ is evident; monocationic $[C_6mim][BF_4]$ displays a noticeable prepeak above the baseline, whereas the corresponding prepeak in the structure function of dicationic $[C_{12}(mim)_2](BF_4)_2$ is much less pronounced. Previous studies by Bodo[103] and Ishida *et al.*[102] claimed very similar structure factors between MILs and DILs, which is due to the short alkyl chains of cations investigated.

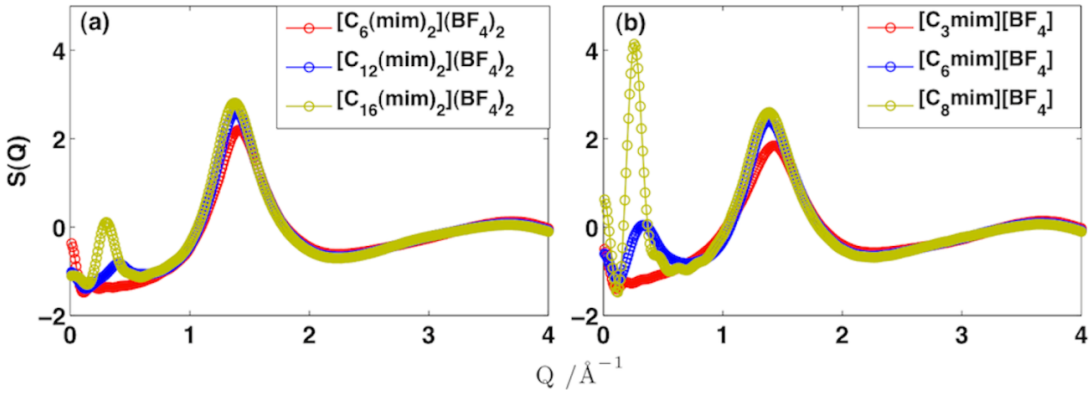

Figure 4.12. Total static structure factors for dicationic $[C_n(mim)_2](BF_4)_2$ (n=6, 12, 16) (a) and monocationic $[C_nmim][BF_4]$ (n=3, 6, 8) (b).

The analysis of the partial structure functions in Figure 4.13(c and d) reveals that in monocationic $[C_6mim][BF_4]$, both anion-anion and cation-anion correlations contribute to the prepeak; whereas the prepeak in dicationic ($[C_{12}(mim)_2](BF_4)_2$ stems from the anion-anion correlation exclusively. Such a trend becomes more evident for the long-chain dicationic $[C_{16}(mim)_2](BF_4)_2$ and monocationic $[C_8mim][BF_4]$ (Figure S4.13c-d). We note that the anion-anion interaction is greatly strengthened in MILs in comparison to DILs. Also, the positive contribution of cation-anion correlations in MILs manifests itself as a negative contribution to the total S(Q) in DILs. The partitioned cation head-anion and chain-anion subcomponents of cation-anion correlations show that the contribution of cation head-anion correlation to the prepeak in DILs is largely cancelled by the trough in the chain-anion structure function. The combined effect of cation head-anion and chain-anion correlations causes the dramatically increased prepeak in monocationic $[C_8mim][BF_4]$, which is associated with the enhanced structural heterogeneity.

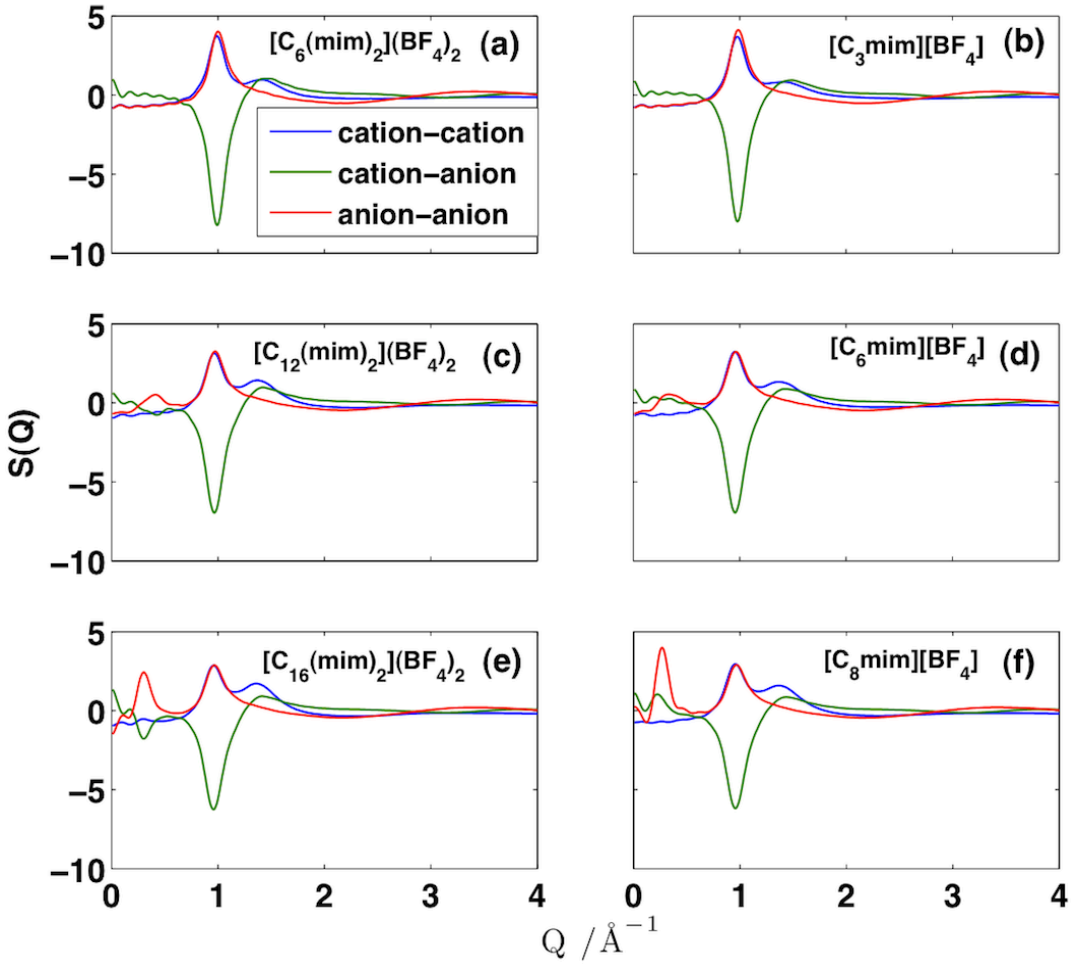

Figure 4.13. Comparison of partial structure functions of DILs $[C_n(mim)_2](BF_4)_2$ (n=6, 12, 16) and MILs $[C_nmim][BF_4]$ (n=3, 6, 8).

According to Hettige *et al.*'s study,[101] it was concluded that the positive-negative (*i.e.*, cation-anion) or polar-polar/apolar-apolar (*i.e.*, polar head-head or anion-anion and apolar chain-chain) interaction gives rise to the length scale for the charge or polarity alternations, which suggests that the size of nanoaggregates may be understood by considering the non-polar alkyl chains. Figure 4.14 presents the cation head-anion subcomponents for both DILs and MILs in the series. Since it is reported that the positive prepeak identifies the length scale of polarity alternation and negative peak (anti-peak) at

approximately 1.0 $Å^{-1}$ identifies that of charge alternations,[124] it is clear that the DILs in Figure 4.14 exhibit charge alternation distance similar to their counterparts of MILs but a polarity alternation distance shorter than that of MILs. Combined with the visual observation in Figure 4.10, it is rational to conclude that the nanoaggregate size formed by alkyl chain is perhaps correlated with the length scale of polarity alternation in both DILs and MILs. The lower-Q prepeak position in MILs corresponds to the larger aggregate size and more significant structural heterogeneity.

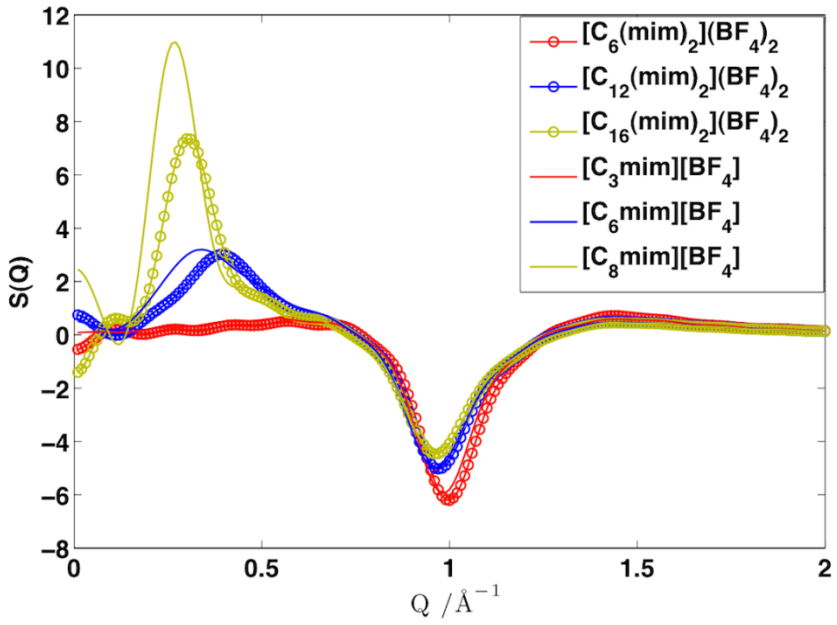

Figure 4.14. Comparison of cation head-anion subcomponents of DILs $[C_n(mim)_2](BF_4)_2$ (n=6, 12, 16) and MILs $[C_nmim][BF_4]$ (n=3,6,8), which implies the real space distance for polarity alternations.

The greater structural segregation in MILs is also supported by Baltazar *et al.*'s experiment.[125] In their study, the critical micelle concentration (CMC) values of a series of monocationic ($[C_nBIm][Br]$ (n=8,10,12)) and dicationic ionic liquids ($[C_n(BIm)_2](Br)_2$ (n=8,10,12)) were measured and they found the CMC decreases with increasing alkyl

chain length of both MILs and DILs. The interesting finding is the dramatic decrease of the CMC for long-chain MILs, whereas DILs exhibit more moderate decrease, suggesting the favorable aggregation for long-chain MILs but relatively unfavorable aggregation for DILs. Although the nanoscale aggregation for ILs in aqueous solutions is not exactly the same as that in neat ionic liquids, the similar trend predicted from this work invites further experimental explorations on this issue. The distinct structural nano-organizations for the aggregates formed in long-chain MILs and DILs will be discussed below.

4.4.2 Influence of Anion Types

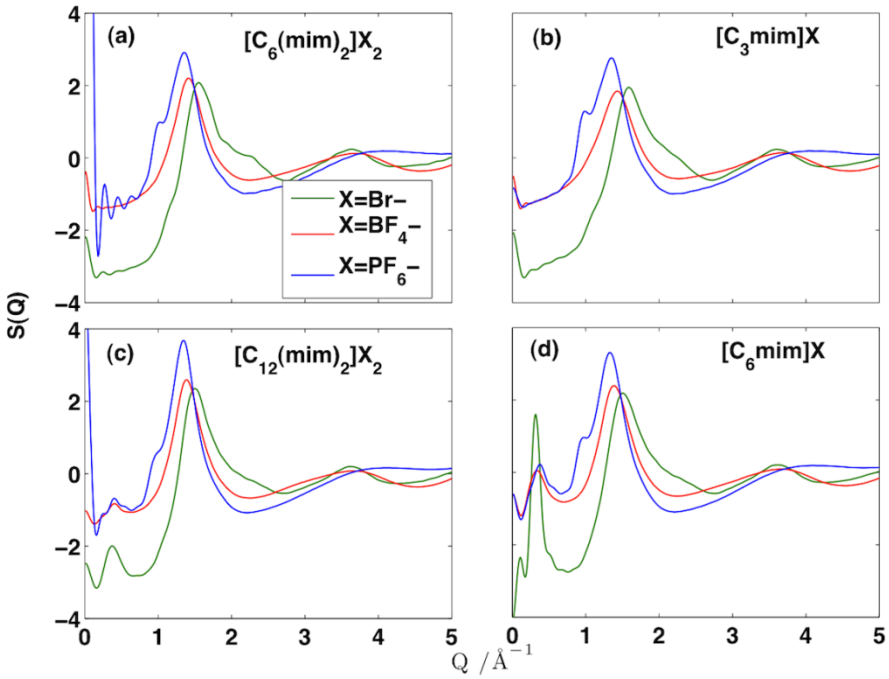

Figure 4.15. Anion-featured total static structure factors for dicationic $[C_n(mim)_2](X)_2$ (n=6, 12 and X=Br-, BF_4-, PF_6-) (a and c) and monocationic $[C_n mim][X]$ (n=3, 6 and X=Br-, BF_4-, PF_6-) (b and d).

The dominant role of anions in the structure of MILs has been demonstrated in Hettige *et al.*'s study.[101] In order to examine the role of anions in DILs compared to MILs,

different types of anions are employed and their structure functions are shown in Figure 4.15. A variety of anions give rise to various structure functions for both long- and short-chain MILs and DILs. For short-chain $[C_6(mim)_2](X)_2$ and $[C_3mim][X]$, the peaks in their structure functions have almost identical amplitudes (ignoring the noise present at Q < 0.15 $Å^{-1}$). For long-chain $[C_{12}(mim)_2](X)_2$ and $[C_6mim][X]$, a discrepancy evident in the prepeaks is located at approximately 0.3 $Å^{-1}$. Br-containing MILs generate the most noticeable prepeaks followed by PF_6- and BF_4-containing MILs, stemming from the variety of the anion X-ray form factors. Their partial structure factors also reveal that anion-anion correlation contributes most to the prepeak in MILs and DILs regardless of the anion type. In particular, cation-anion interactions also contribute to the prepeak in MILs in contrast to DILs.

4.4.3 Structure Models for DILs

Now let us look into the structural nano-organization of long-chain MILs and DILs. Triolo *et al*. have proposed a micelle-like nanoaggregate model for MILs with long alkyl tails[37,123] as shown in Figure 4.16a, in which the free alkyl tails in the center interact with each other by van der Waals interaction and anions are excluded due to the strong electrostatic interaction between cation head groups and anions. For DILs, the nanoscale organization is more complicated since the linkage alkyl chain is constrained by the imidazolium ring at two ends, leading to the decreased flexibility. Therefore, it is relatively unfavorable for DILs with long linkage chains to assemble compared with their monocationic counterparts with free long tails. Deng *et al*.'s study[126] revealed that the replacement of the terminal -CH_3 group with -OH group in the alkyl chain of MILs results in the failure of aggregation of long alkyl tails. Similar consequence occurring in

DILs may result from the enhanced polarity compared with MILs by additional polar head groups in dications, which prevents the evident aggregation of non-polar alkyl chains. This is also evidenced by the shorter polarity alternation distance of DILs in contrast to MILs shown in Figure 4.14. The smaller-sized aggregates observed in DILs indicate fewer DILs are involved in the aggregates formation because of the increased polarity resulting from additional polar head groups.

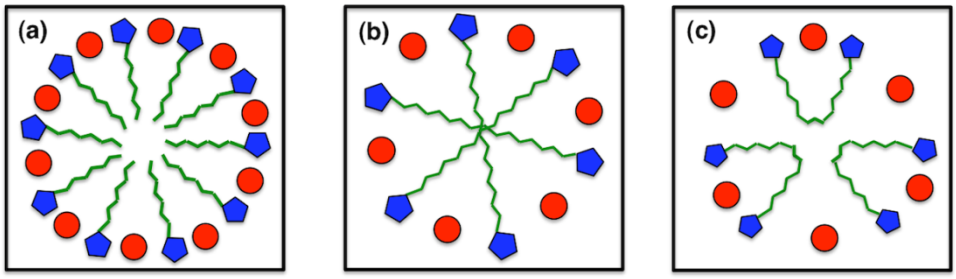

Figure 4.16. Schematic representation of the micelle-like nanoaggregates formed by long alkyl tail in MILs proposed by Triolo *et al*.[37,45] (a) in contrast to the straight (b) and folded chain (c) models for the nanoscale arrangement of DILs with long linkage chain, respectively. The red dot represents the anion; the blue one denotes the positively charged ring and the green line is the alkyl chain. Note that there is two anions for each cation in b) and c).

Moreover, the relative distance of the two imidazolium rings may also play a big role during the aggregation of long-chain DILs. In this case, there are two models proposed for the assembly of long linkage chains in DILs, which are shown in Figure 4.16b-c. One is the straight chain model (Figure 4.16b), in which straight linkage chains cross with each other in the center of micelle with the two completely separated positively charged rings surrounded by negatively charged anions. The other folded chain model (Figure 4.16c) describes the situation when two rings are close to each other through a highly

curved linkage chain. However, the distribution of the angle formed by the two vectors pointing from each ring of dication to the center of linkage chains, shown in Figure 4.17a, demonstrates that the folded chain model is not preferred in DILs, since the long-chain dications exhibit the highest population in large obtuse angles, which suggests the dication tends to be in an unfolded state. The angle with the largest population as a function of chain length shown in Figure 4.17b exhibits a bell-like relationship, which can be interpreted as the interplay between the polarity alternation and the increased flexibility with the elongation of alkyl chains. For short-chain dications, the shorter distance between polar groups (head groups and anions) results in the stronger electrostatic interaction between head groups and anions, which may highly fold the chain with sharp angles; with the increase in chain length, the polarity alternation distance is increased, which strengthens the unfolding of alkyl chains. However, as the chain length increases, the chain flexibility is enhanced as well. The maximum angle was reached as the polarity alternation dominates (as n=9); whereas as the chain flexibility increases, the influence of the chain flexibility overwhelms the increased polarity alternation, which leads to the folding of alkyl chains again.

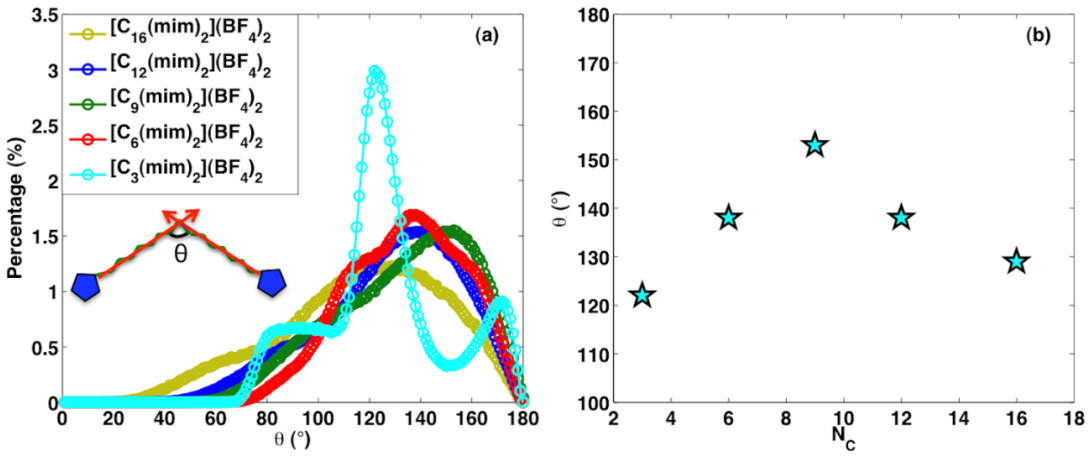

Figure 4.17. (a) The distribution of the angle formed by two vectors pointing from the ring to the center atoms of linkage chain in $[C_n(mim)_2](BF_4)_2$ (n=3, 6, 8, 12, 16); (b) The angle with the largest population (the angle corresponding to the maximum percentage show in (a)) as a function of linkage chain length.

It should be noted that the models shown in Figure 4.16b-c do not correspond to the angular distribution function in Figure 4.17a. The straight chain model represents the highly unfolded state or wide-angle region and the folded chain model corresponds to the tightly folded state or narrow angle region. Although Figure 4.16b presents the favorable nanoaggregate structure for long-chain dications, it is noteworthy that these two models describe the idealized cases; in reality the nanoscale aggregates are more complicated and may consist of the mixture of a majority of unfolded (as shown in Figure 4.16b) and a small portion of highly folded (as shown in Figure 4.16c) DILs. Compared with the linkage chains of DILs with restrained flexibility, the flexible alkyl tails in MILs are likely able to aggregate with each other under the driving of van der Waals interactions, which is reflected in the more significant structural heterogeneities in MILs.

4.4.4 Conclusion

In conclusion, this work unravels the different behaviors in structural arrangement of the alkyl linkage chain of DILs at long-, medium- and short-range lengths in comparison with the alkyl tail chains of MILs. For short-range alkyl chain, the cations in DILs and MILs exhibit nearly identical structural nano-organization and heterogeneity; the significant difference in structural heterogeneity of DILs and MILs is observed in medium-/long-chain ILs regardless of the type of anions, which is supported by the HOP values as well. The unique assembly pattern for long linkage chains (straight and folded

chain models) in DILs explains the observed insignificance of prepeaks contrary to those in MILs, which provides molecular insights into the nature of structural heterogeneity in DILs as well as a conceptual model for the interpretation of experimental observations.

CHAPTER V

IONIC LIQUIDS IN CONFINMENT

This chapter presents the dynamics and structural properties of a room temperature ionic liquid (RTIL) 1-Butyl-3-Methyl-Imidazolium(trifluoromethanesulfonimide) ([C_4mim][Tf_2N]) confined in silica and carbon mesopores at different loading fractions using MD simulations and nuclear magnetic resonance (NMR) experiments. The interfacial properties of RTILs at solid interfaces are crucial for the application of RTILs in energy storage devices. This study investigated the interfacial microstructure of RTIL and the dynamical property at silica and carbon surfaces at different temperatures, which may inspire further experimental research on RTILs near differently featured solid walls as well as provide a baseline of neutral liquid-solid interfaces for the application of confined RTILs in the field of energy storage devices. This work has been published in reference 12.

5.1 Introduction

Room temperature ionic liquids (RTILs) are currently attracting widespread research interest due to a variety of properties (*e.g.* wide electrochemical window, low vapor pressure, non-flammability and high conductivity)[2,3,127] and a wide range of applications (*e.g.* electrolytes,[128-130] lubricants[131,132] and solvents[78]). Among these, the most attractive uses of RTILs are for energy storage devices and lubricants. Both of these applications take advantage of the interfacial behavior of RTILs at solid-liquid interfaces. In energy storage devices, such as supercapacitors, their performance is dominated by the electrical double layer (EDL), which is formed by the accumulated electrolytes near electrode surfaces.[133,134] The relationship between EDL microstructure and the energy stored has

been investigated in a great number of studies.[17,135-139] The charging efficiency is determined by the solid-liquid interface as well.

Regardless of the ionic liquid itself, solid materials also play a vital role in determining the efficiency of charging/discharging of energy storage devices. Both the constituent and surface properties of electrodes are responsible for the performance of energy storage devices. At present, carbon and silica-based materials are commonly used electrodes.[140,141] Compared with molecularly smooth graphene-based carbons such as graphene sheets and carbon nanotubes, the silica surface is mostly hydroxylated, thus generating nanoscale corrugation. Surface nanoroughness has been reported to retard the dynamics of liquids drastically.[142] Although a series of studies[143-145] of surface roughness effects on confined fluids has been reported, research on confined RTILs is incomplete. In the present work, the hydroxylated silica surface exhibits solvophilic-like properties in contrast to a solvophobic carbon surface. These terms are to be understood analogous to "hydrophilic" and "hydrophobic", respectively, used in the case where the solvent is water. Hence a solvophilic surface can be easily solvated by polar solvents while solvophobic one is not. The different behaviors of RTILs near solvophilic and solvophobic surfaces are critical for understanding the related application of RTILs in energy storage and lubrication.

RTILs were also reported to exhibit distinguishing properties under confinement compared to those in bulk.[10] The RTIL density near the interface is enhanced relative to bulk and approaches the bulk value as the distance from the interface increases.[16,146] Therefore, the RTILs at the center of a mesopore were shown to exhibit a bulk-like dynamic behavior; in contrast, ions close to a solid surface displayed solid-like (rigid

layer-by-layer) structure and slow dynamics. The restricted diffusion of confined RTILs has been investigated in numerous studies;[146-148] however, to our knowledge, the temperature effects on the dynamic properties of confined RTILs have not been previously reported. The decrease of the melting temperature of RTILs was observed in nanoporous silica matrix.[149,150] In a recent experimental study,[151] it was demonstrated that the compressed gas during RTIL loading dominated the variation of phase behavior: the loading of RTILs at high vacuum resulted in fully loaded nanopores with increased melting point and slower dynamics; atmospheric loading resulted in partially filled nanopores with decreased melting point and enhanced dynamics. The effects of the loading fraction on structural and dynamic properties of RTILs were also investigated in a molecular dynamics (MD) simulation study.[148] Due to the vacuum environment of the mesopore in our simulation, samples with low RTIL loading fractions in the silica pore form a layer on the surface and their dynamics exhibit a loading fraction-dependent decrease. Therefore, understanding how the structure and dynamic properties of RTILs vary in relation to the method of confinement is essential for future applications in the areas of energy storage and lubrication relating to the solid-liquid region.

From the above-mentioned perspective, the fundamental study of the interfacial properties of RTILs near carbon and silica surfaces is of great interest. This work investigated the influence of different confinement environments on the dynamics and structural properties of 1-Butyl-3-Methyl-Imidazolium(trifluoromethanesulfonimide) ($[C_4mim][Tf_2N]$) near solid-liquid interfaces (silica/$[C_4mim][Tf_2N]$ and carbon/$[C_4mim][Tf_2N]$) using MD simulations and nuclear magnetic resonance (NMR) measurements. The effects of loading fraction and temperature were examined as well,

which render the fundamental understanding the interfacial behaviors of RTILs near different solid surfaces.

5.2 Simulation Details

The amorphous silica was prepared by initially heating bulk silica up to 1800 K followed by gradually annealing to 300 K within 10 ns using MD package LAMMPS.[152] During this process, the ClayFF force field was adopted for bulk silica.[153] The silica mesopore with the diameter of 9.5 nm was carved in the bulk amorphous silica and then simulation annealing was performed again for 10 ns. Afterwards, the pore surface was fully hydroxylated at the experimental surface density of 4.6 OH/nm^2.[154] The hydroxylated silica pore was finally relaxed in a 200 ps MD simulation. The carbon mesopore was modeled by three layers of CNTs with a gap of 0.341nm between each two neighboring layers. The inner tube has a diameter of 6.78nm.

All production simulations in this work were performed using MD package Gromacs.[77] The exp-6 force field was used for RTIL [C_4mim][Tf_2N].[155] All the bonds were constrained during simulations. The time step of 1 fs was used to integrate the equation of motion with spherical cutoff of 1.1 nm in non-bonded van der Waals interactions. Long-range electrostatic interactions were treated by particle mesh Ewald (PME) method.[109] Periodic boundary conditions were applied in three dimensions. The silica/carbon mesopore was completely frozen throughout the simulations, i. e., no movable atoms in silica/carbon mesopores. The force field for hydroxylated silica was adopted from Ref. 148.[148] To obtain a reasonable density inside the pore at varying temperatures, grand canonical MD simulations were performed first using isothermal-isobaric ensemble (NPT) at target temperatures (280 K, 300K, 320K, 340 K, 360 K) and

1 bar. After equilibration, canonical (NVT) simulations were performed for $[C_4mim][Tf_2N]$-filled mesopores at different loading fractions (f = 1.0, 0.5, 0.25, f = loading fraction) in the canonical ensemble. The simulation setup is shown in Figure 5.1.

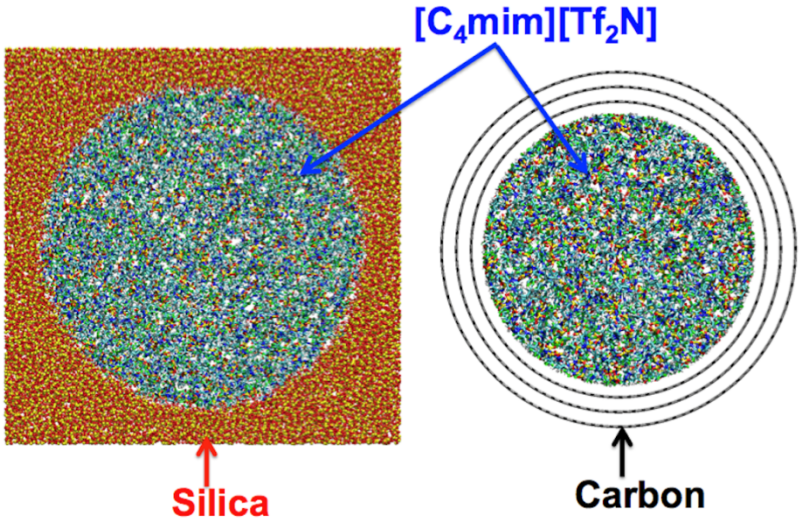

Figure 5.1. Cross-section view of the model silica and carbon mesopores filled with an ionic liquid.

The number of molecules in the fully-filled pore was determined according to the grand canonical simulations. The different loading ratios were achieved by removing the proper amount of RTILs inside the fully-filled pore to reach the specific volumetric ratio. After completing equilibration for 8 ns, 4-10 ns production run was generated. To investigate the temperature effects, the simulations were performed between 280 and 360 K with 20 K increments and 290K, 300K, 310K, 330K, 340K and 350K for RTILs confined by carbon mesopores.

The diffusion coefficient was calculated according to the Einstein relation.

$$D = \lim_{t\to\infty} \frac{1}{6t} \left\langle [r_i(t) - r_i(0)]^2 \right\rangle \qquad (5.1)$$

After linear fitting of the mean square displacement (MSD), the diffusion coefficient was obtained from the fitted slope divided by six. Note that in simulations the diffusion coefficient of C_4mim+ ions was calculated to represent the diffusion property of [C_4mim][Tf_2N] and compared with our experimental results, since NMR determined the diffusion of [C_4mim][Tf_2N] based on the C_4mim+ ions. For layer-by-layer diffusion, the confined RTILs [C_4mim][Tf_2N] in silica/carbon are divided into five layers with the identical thickness along the radial direction. According to the initial location of the center of mass of ions, each ion is labeled with a layer number (1, 2, 3, 4, 5). The MSD diffused by ions with a given layer number was calculated as function of time. The diffusion coefficients of ions in individual layers were then obtained using the aforementioned method, since the radial diffusion of ions in the first two adsorbed layers is negligible and the other layers in bulk-like regions share similar dynamics properties.

The number density profiles were calculated along the radial direction of silica mesopores. The van der Waals and electrostatic interaction potentials for silica confined [C_4mim][Tf_2N] were calculated based on van der Waals equation and Coulomb's Law, respectively. The cutoff distance was 1.1 nm. For carbon-confined [C_4mim][Tf_2N], the Buckingham exp-6 potential was used to represent van der Waals interactions.

5.3 Dynamics Properties of Ionic Liquids Confined in Silica and Carbon Mesopores

5.3.1 Influence of Temperature on Diffusion

As shown in Figure 5.1, the RTIL [C_4mim][Tf_2N] was confined in silica and carbon mesopores. The dynamics of confined [C_4mim][Tf_2N] were investigated over the temperatures range from 280 to 360 K. Although the silica and carbon mesopore sizes in the model are different, the focus in this work is on the solid-liquid interfacial regions

(silica/RTILs and carbon/RTILs) rather than the size effects. The diffusion coefficients of bulk and confined C_4mim+ as a function of temperature at different loading fractions are shown in Figure 5.2. Clearly, once confined, the diffusion of ions was slowed down in both mesopores, exhibiting similar trends seen in previous reports.[146-148] We also measured the diffusion properties of [C_4mim][Tf_2N] in bulk and confined in porous silica using the NMR technique. The trends obtained from NMR measurements are in a good agreement with the MD results.

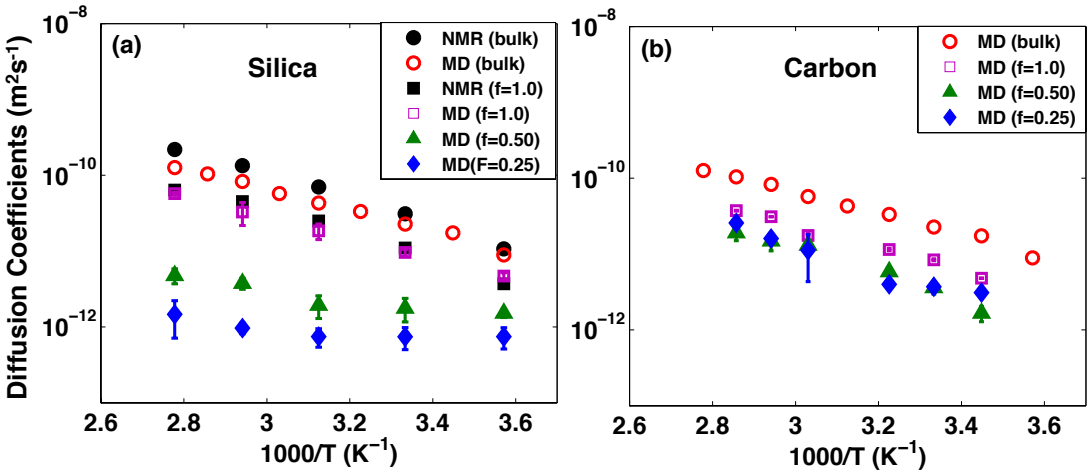

Figure 5.2. Diffusion coefficients of C_4mim+ confined in silica (a) and carbon (b) mesopores as a function of temperature at different loading fractions (f).

Moreover, as the loading fraction is decreased from 1.0 to 0.5 and then 0.25, the diffusion coefficients for silica mesopore-confined [C_4mim][Tf_2N] declined dramatically. The similar trend was observed for carbon confinement as well, though the magnitude of the change is attenuated, and is in accordance with previous studies.[148] Changes in temperature cause different responses for silica and carbon mesopores. At low loading fractions, the temperature dependence of diffusion for silica-confined [C_4mim][Tf_2N] is weakened compared to that in carbon-confined [C_4mim][Tf_2N]. The diffusion coefficient

of [C_4mim][Tf_2N] close to the silica surface is relatively insensitive to temperature variation. A similar change in slope is not observed for the temperature dependence of diffusion coefficient as a function of loading fraction in the carbon mesopore.

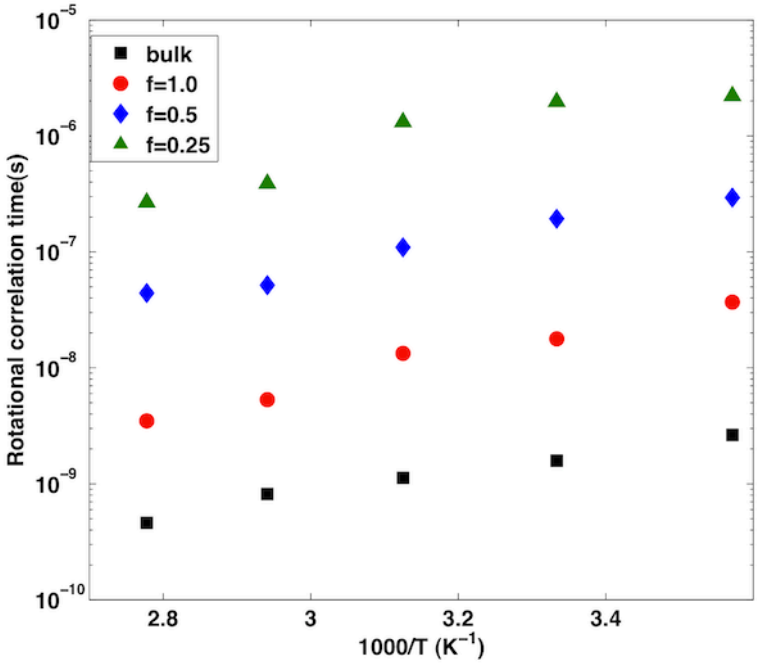

Figure 5.3. Rotational correlation time of cation C_4mim+ as a function of temperature for varying loading fractions in silica mesopores, from MD simulation.

In contrast to translational diffusion, the rotational motion of C_4mim+ in silica pore at low loading fraction exhibited significant temperature dependence, as shown in Figure 5.3. The rotational correlation time of silica-confined C_4mim+ increases as loading fraction decreases and increases as temperature declines.

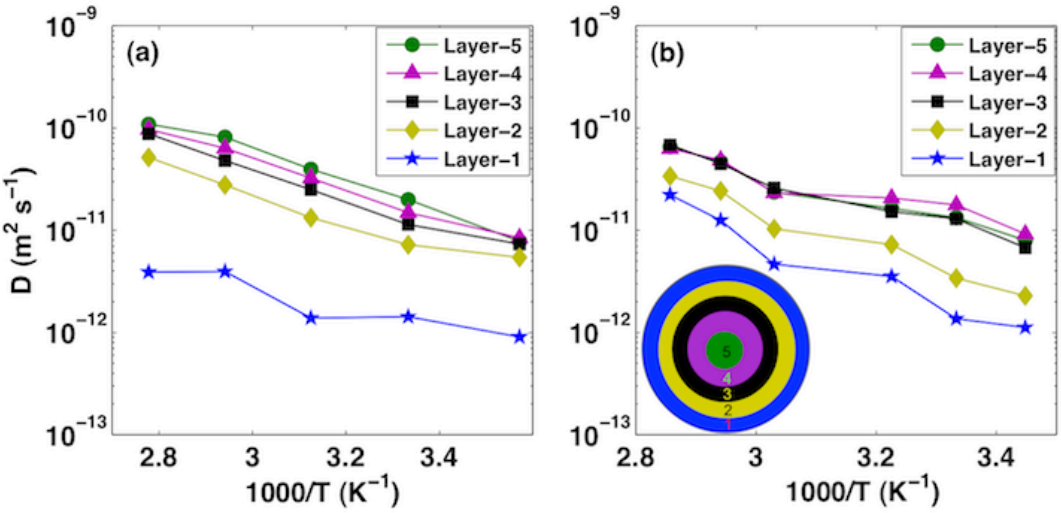

Figure 5.4. Layer-by-Layer diffusion coefficients for silica (a) and carbon (b) mesopores confined C_4mim+ as a function of temperature as predicted by MD simulation. The layer thickness is about 1.0 nm in (a) and 0.66 nm in (b).

The layer-by-layer analysis of the diffusion coefficients of [C_4mim][Tf_2N] in fully filled silica and carbon mesopores (Figure 5.4) revealed that ions in the central layers exhibit greater temperature dependence and higher diffusion coefficients compared to the layer closest to the silica walls (Layer-1, Figure 5.4a). In contrast, for [C_4mim][Tf_2N] confined in carbon, the ions exhibited similar temperature-dependent diffusion regardless of the layer they were located in. This suggests that the layer closest to the solid silica wall (*i.e.* Layer-1, Figure 5.4a) dominated the temperature dependence of diffusion at low loading fractions, where the mobility of the ions was restricted. To further investigate the origins of the different temperature dependence of diffusion in confined [C_4mim][Tf_2N], the interfacial microstructures of [C_4mim][Tf_2N] in silica and carbon mesopores were calculated and shown in Figure 5.5, respectively.

5.3.2 Interfacial Microstructure

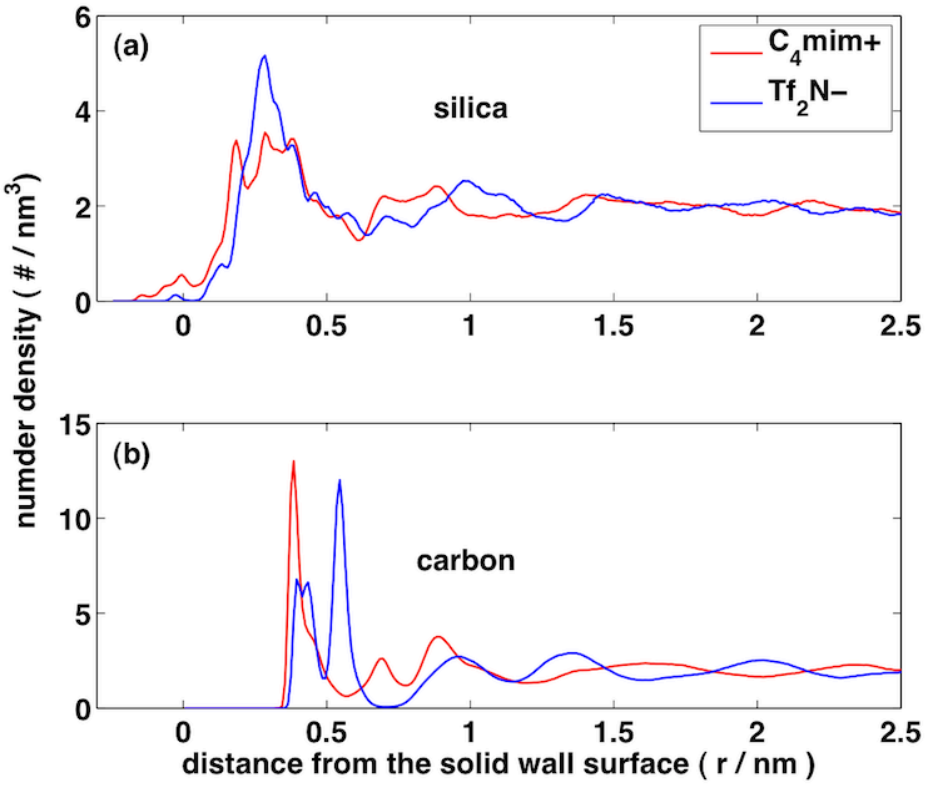

Figure 5.5. MD simulation result for the number density profile of [C_4mim][Tf_2N] (f=1.0) confined in silica (a) and carbon mesopores (b), respectively, at 300 K.

Figure 5.5 displays the number density profiles of confined C_4mim+ and Tf_2N- as a function of distance to the silica and carbon walls, respectively. The highest peak position for the cation of silica confined [C_4mim][Tf_2N] is approximately at 0.28 nm, which is closer to the solid walls compared to the peak position at 0.39 nm for cations and 0.56 nm for anions of carbon confined [C_4mim][Tf_2N]. This is also true for partially-loaded mesopores, which displays the decreasing number of ion layers near the silica or carbon surfaces as loading fraction is decreased. The first peak position is found to shift slightly toward the center of pore as the loading fraction decreases, which is probably attributable to the increased fraction/mobility of ions located in ion/vacuum interfaces. As the loading

fraction decreases, fewer ions are present near solid walls, resulting in an increasingly inhomogeneous distribution across/on the pore. The low density near the silica surface is probably due to the limited accessible volume for ions, and the oscillation of the density profile near silica surface is mainly due to the rough surface and non-uniform distribution of silica atoms. To describe the degree of surface roughness, the distribution of atoms as a function of distance along the axis of silica or carbon mesopore was calculated and is shown in Figure 5.6. The atom number density in a silica mesopore gradually increases from 0 at 4.4 nm to the average density typical for the silica matrix. The non-uniform distribution of silica atoms indicates the surface roughness of the silica walls. Compared to the heterogeneous silica surface, the carbon mesopores exhibit a constant number density located at three layers of carbon mesopore, which is an indication of a smooth homogeneous carbon surface.

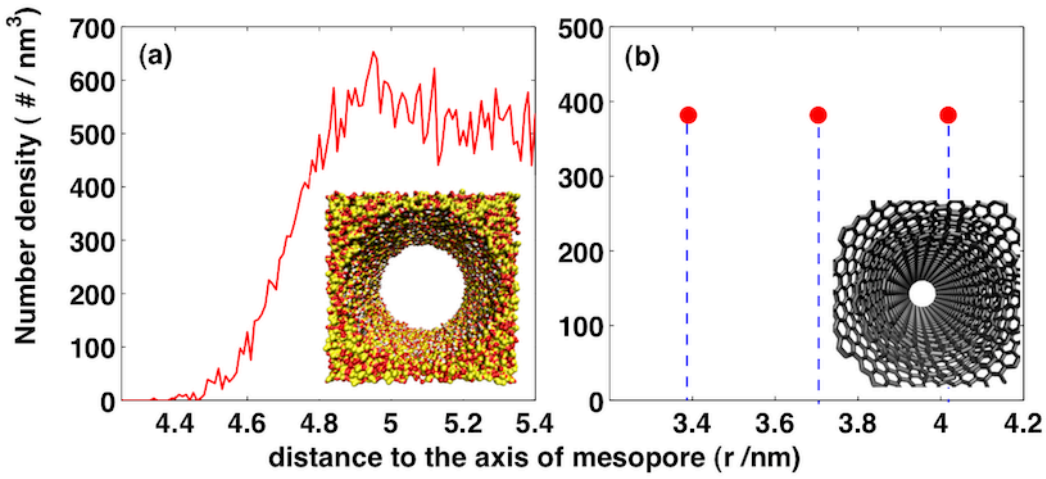

Figure 5.6. Number density distribution of atoms in silica (a) and carbon (b) mesopore as a function of the distance from the pore axis, from MD simulation.

Furthermore, there is an obvious gap in the number density profile between ions and carbon wall; for the silica mesopore, there is more accessible space for ions (also see

Figure 5.1), *i.e.* the ions penetrate into the small cavities in the surface driven by adsorption. This feature can be identified as solvophilic properties, which usually means the solid wall has high affinity for solvents. In contrast, the carbon mesopore is considered as solvophobic, which repels [C_4mim][Tf_2N] from its surface. The closer contact of water with a hydrophilic surface was observed in a recent simulation work.[156] It was also found that in the vicinity of a rough surface, water molecules filled voids created by removed atoms.[157] Fuchs *et. al.* investigated the structural properties of butane confined by smooth and corrugated walls with Monte Carlo simulations.[158] Their findings that the confined molecules are closer to a corrugated surface and the density near this surface is lower than near a smooth one were also inspected in N_2 adsorption onto solid walls in another density functional theory (DFT) study.[157] The effects of roughness play a similar role as surface hydrophilicity or solvophilicity, which enables the closer contact of confined fluids and a wider range of density distributions compared to smooth hydrophobic/solvophobic surfaces. However, in our study, the degree of roughness of silica is not as remarkable as the nanoscale corrugation in the aforementioned studies.[156-158] The surface corrugations of silica can be mainly attributed to terminating surface hydroxyl groups that broaden the local disorder, which is in the subnanometer size. Therefore, roughness effects may not be the major cause of the different microstructures of RTILs near silica and carbon mesopores; solvophilicity of silica and solvophobicity of carbon might play a bigger role in forming different interfacial structures of RTILs. The force profiles on hydrophilic and hydrophobic spheres from AFM measurements displayed a jump near a hydrophobic surface,[159] which may be related with the gap in the number density profile for carbon mesopores. Nevertheless, whether such a difference is

a result of the surface roughness or hydrophobicity is uncertain, and may be a joint effect of both.

5.3.3 Solid-Liquid Interaction Potential

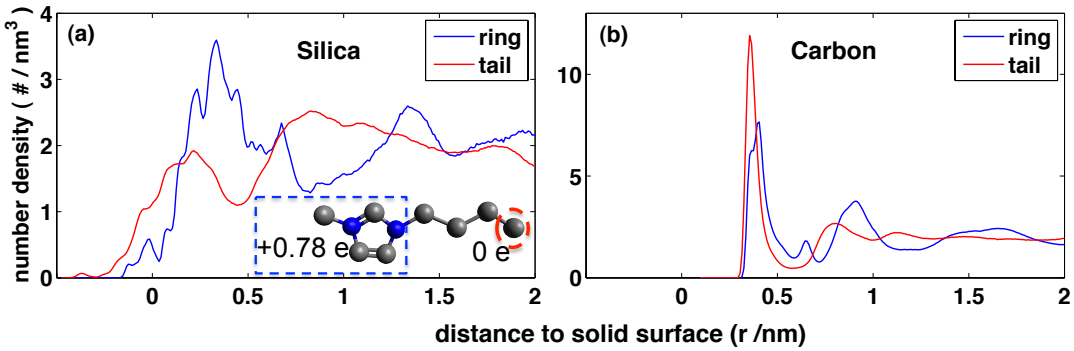

Figure 5.7. Number density profile of the center of mass of cation ring and the end carbon atom of the alkyl chain in cation confined in silica (a) and carbon mesopores (b) from MD simulation.

To explore the factors leading to distinctive structures of RTILs near silica and carbon surfaces, the interaction energy between ions and silica or carbon mesopore walls, respectively, was calculated. Due to the atomic partial charges at silica surfaces, the electrostatic potential plays a role and dominates the interaction between ions and silica walls. The domination of electrostatic interaction is evidenced by the number density profiles for the center of mass of cation imidazolium ring and the carbon atom in the end of a cation alkyl chain shown in Figure 5.7. For [C_4mim][Tf_2N] in silica mesopore (Figure 5.7a), the peak position for the highly positively charged ring is located at 0.33 nm, while the peak position shifts to 0.83 nm for the weakly charged alkyl tail. The difference of 0.5 nm approximates the distance from the center of ring to the end of the carbon alkyl tail in one cation. On the contrary, the carbon-confined number density peak position for the ring nearly overlapped with that of alkyl tail (Figure 5.7b). This suggests

that the electrostatic interaction drives the structuring near the silica walls and causes realignment of cation ring and alkyl chains, which is not the case for [C_4mim][Tf_2N] near carbon walls. It can be noted that alkyl chains diffuse deeper into the cavities in silica, which restrains the access of the relatively big cation rings. For carbon mesopores, in our MD simulations, only relatively weak van der Waals forces between ions and carbon walls contribute to the structuring of the [C_4mim][Tf_2N].

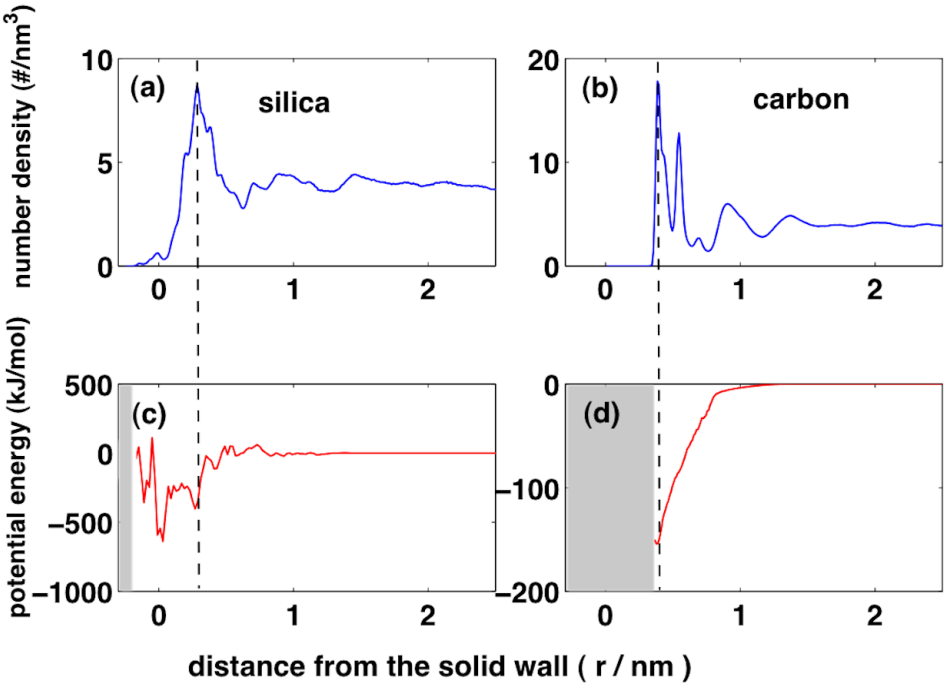

Figure 5.8. Total number density profile of [C_4mim][Tf_2N] confined by (a) silica and (b) carbon mesopores and the averaged interaction potential per ion as a function of distance towards the solid wall surface for (c) silica-confined and (d) carbon-confined [C_4mim][Tf_2N] from MD simulations. The shaded areas in (c) and (d) represent the ion-free space.

The peak in number density profile corresponds to the negative attraction potential in bottom figures of Figure 5.8. The dramatic fluctuation of the average interaction potential

between ions and silica walls demonstrates the alternating attraction and repulsion occurring near the surface and contrasts with the unidirectional attraction near the carbon interface. For $r < 0$, the rugged surface features a large number of smaller and larger cavities with different electrostatic potentials, which may be more or less energetically favorable for different charged particles. While some of the cavities may be energetically favored, as indicated by the negative values of the potential, the entropic forces of confinement limit further penetration of fluid particles deeper into silica. It is worthwhile to note that because the potential calculation is based on the binning method along the overall radial direction of the mesopore and the silica surface is not smooth, for the ions locating in cavities that are below the average height of the surface, the binning direction is not normal to the local cavity surfaces. Therefore, there are apparent negative attraction peaks for cavity atoms beneath the silica surface observed in Figure 5.8c for $r < 0$. The fluctuating potential profile ($r > 0$) near silica surface is analogous to the oscillatory force profile near hydrophilic surfaces measured in AFM expeirments[160]; the less oscillatory force profile near hydrophobic surface is observed as well in AFM[160,161] measurement and MD simulation.[161] Laria *et al.* observed the oscillating number density profile near hydrophilic and corrugated hydrophobic silica surfaces but less oscillating profile near hydrophobic silica surface,[162] which agrees with our potential profile near silica and carbon walls. It may indicate that the experimentally observed oscillatory number density profile is determined by the interfacial potential profile.

Although the corresponding attractive potential for $[C_4mim][Tf_2N]$ in silica is larger in magnitude than for $[C_4mim][Tf_2N]$ in carbon, it is noticed that the number density near silica is lower than that near the carbon surface. This probably can be attributed to the

potential fluctuation in silica-[C_4mim][Tf_2N] interface; in contrast, the smoothly unidirectional potential profile facilitates the accumulation of ions near carbon-[C_4mim][Tf_2N] interface. However, even though the peak of number density for silica confined [C_4mim][Tf_2N] is lower than that of carbon confined one, the total number of ions accumulated near silica surface is higher than that near carbon surface due to the increased accessible surface area of silica walls. Additionally, the number density for $r <$ 0.3 nm might be underestimated, resulting from the inaccurate estimation of volume close to silica walls due to the surface corrugation which is not taken into account during the number density calculation. Similar potential profiles for cations and anions near carbon surface are present; whereas distinct profiles are disclosed for those near silica surfaces. And the obvious attraction for cations and repulsion for anions around the silica surface (r=0) lead to increased number of cations and decreased anions as shown in the corresponding number density profiles, which, in another way, indicates the important influence of electrostatic potentials and surface roughness for silica pores.

It is known that surface heterogeneity and solvophobicity influence both the structural and the dynamic properties of confined fluids near solid surfaces. Jun *et al*. reported that the reduced diffusion coefficients of confined particles in a rough channel using the numerical lattice Boltzmann method.[163] Similar behavior was reported in MD simulations as well.[145] Enhanced viscosity near a hydrophilic surface from MD simulation was reported by Netz *et al*.[156] Therefore, both surface roughness and hydrophilicity/solvophilicity can result in decreased diffusion. Although this behavior has been previously reported, the weakened temperature dependence of diffusion near solvophilic and corrugated silica surface is reported here for the first time. It is reasonable

to correlate the weakened temperature dependence of diffusion near solid walls with the surface heterogeneity and solvophilicity, which might facilitate the formation of layers directly in contact with solid walls with decreased temperature sensitivity. This rationalization of the weak temperature dependence of diffusion is still waiting to be verified experimentally.

5.3.4 Conclusion

In summary, this study reports the influence of different types of solid walls on the structural and dynamic properties of confined RTIL [C_4mim][Tf_2N]. The following phenomena were noted: 1) The diffusion coefficients of [C_4mim][Tf_2N] confined in silica and carbon mesopores exhibited dissimilar temperature dependence as loading fraction changed; 2) more complicated interfacial microstructures of [C_4mim][Tf_2N] near solvophilic silica mesopores were observed; 3) an oscillatory interaction potential profile near silica surface was revealed, in contrast to a non-oscillatory potential profile near a smooth carbon surface; 4) both surface heterogeneity and features of the interaction potential for silica mesopore (*i.e.*, electrostatic interaction) might contribute to the distinctive interfacial microstructure and weakened temperature dependence of diffusion. The closer contact of [C_4mim][Tf_2N] with rough and solvophilic silica walls is in agreement with both theoretical and experimental reports. The observed oscillatory interaction potential profile near the silica surface coincides with the measured force profile from AFM measurements. The weakened temperature dependence of diffusion near silica surfaces at low loading fraction is observed herein for the first time, which may be attributed to the surface roughness and solvophilicity. We hope that this study may inspire further experimental research on RTILs near differently featured solid walls

as well as provide a baseline of neutral liquid-solid interfaces for the application of confined RTILs in the field of energy storage devices.

CHAPTER VI

IONIC LIQUIDS AS ELECTROLYTES IN SUPERCAPACITORS

In this chapter, the performance of ionic liquids as electrolytes in supercapacitors is presented. In Section 6.3, an equimolar mixture of 1-methyl-1-propylpyrrolidinium bis(trifluoromethylsulfonyl)imide ($[C_3mpy][Tf_2N]$), 1-methyl-1-butylpiperidinium bis(trifluoromethylsulfonyl)imide ($[C_4mpip][Tf_2N]$) is studied as electrolytes for onion-like carbon–based supercapacitors due to its lower melting point and higher conductivity than neat ionic liquids. The influence of temperature on the electric double layer is also taken into consideration in this study. The aim of this work is to interpret how the binary electrolytes at varying temperatures influence the EDL microstructure and the differential capacitance of OLC-based supercapacitors. This work is published as reference 14. Section 6.4. presents the interfacial structure and electrochemical performance of DILs $[C_n(mim)_2](BF_4)_2$ (n=3, 6, 9) and $[C_6(mim)_2](Tf_2N)_2$ in comparison with their monocationic counterparts. The influence of anion type on the capacitance-potential curve was also studied. This work provides the molecular insight into the electric double layer formed by DILs at OLC surfaces for the first time, which has been published in reference 19. Finally, Section 6.5 presents the influence of organic solvents acetonitrile (ACN) on EDL structure and capacitive performance of DIL electrolytes-based supercapacitors. The conductivities of a DIL (1-hexyl-3-dimethylimidazolium bis(trifluoromethyl)imide) $[C_6(mim)_2](Tf_2N)_2$ in ACN at varying concentrations as well as the EDL structures and C-V curves for neat $[C_6(mim)_2](Tf_2N)_2$ and $[C_6(mim)_2](Tf_2N)_2$/organic solvent mixture at a planar graphite electrode were investigated. This work is published in reference 20.

6.1 Introduction

Room temperature ionic liquids (RTILs) are promising electrolytes in energy storage devices. The application of RTILs in electrical double layer capacitors (EDLCs, also named supercapacitors) that store electric energy in the form of electrical double layer, has attracted increasing research interest due to its longer cycle life, higher power density and faster charging/discharging rates than organic or aqueous electrolytes.[164-167] The current utility of RTILs is restricted by the limited operating temperature range, which is mostly within 293-353 K. In order for supercapacitors to be used under severe cold weather conditions (specifically, temperatures as low as -50˚C, corresponding to the lower limit for automotive applications), ionic liquids with lower melting points are essential while retaining the capacitance. In this direction, binary mixture of RTILs exhibited reduced melting temperature than either of the neat RTILs and widened liquidus range,[168] thus favoring the low-temperature application of RTILs. These mixed RTILs with decreased melting points are also referred to as eutectic ionic liquids, since the concentrations chosen correspond to eutectic points on the phase diagram.

To achieve better electrochemical performance, electrolytes consisting of mixed RTILs have been used in lithium batteries[169] and dye-sensitized solar cells.[170] A recent study found that an equimolar mixture of piperidinium- and pyrrolidinium-based RTILs with the same anion bis(fluorosulfonyl)imide (FSI) as electrolytes near exohedral onion-like carbon (OLC) electrode exhibited a broadened operation temperature range and increased conductivity at low temperature.[16] Because of the implications of such eutectic mixtures for energy storage and conversion devices, understanding the molecular behavior near electrode surfaces with well-defined surface curvatures is of great importance for further progresses in this field. Hence, it is scientifically interesting to

understand the influence of temperature on the capacitive behavior of binary mixtures near the OLC electrode surface. Such electrodes have a simpler surface geometry than most porous carbons normally used as electrodes in supercapacitors. The nonporous OLC electrodes can be described as nearly spherical particles having a concentric fullerene shell structure and exhibiting a narrow particle size distribution. Thus, the simpler exohedral model describing the surfaces of OLCs offers a suitable reference for investigating the positive temperature issues associated to the eutectic mixtures of RTILs on carbon electrodes issue using molecular dynamics (MD) simulation. In addition, the OLC electrode has been reported as an excellent electrode material owning to high charging rate and power density.[171,172] Such electrodes possess a unique parallel capacitance-potential (C-V) curve rather than the common bell-, cameral- or concave-shaped curves.[13] This property greatly favors the stable performance of supercapacitors.

To date, the influence of temperature on the capacitance using RTIL electrolyte has been investigated both experimentally[17,18,173,174] and by computational[175-179] methods. Most of the experimental work[17,18,173,174] shows that the capacitance increases as temperature increases (positive temperature dependence), a trend also observed in high temperature molten salts.[180,181] However, the opposite trend (negative temperature dependence) was found for RTILs at a mercury electrode[182] and molten salts at liquid magnesium electrodes.[183] In contrast, theoretical studies have predicted negative temperature dependence for graphite electrodes in MD simulation[175] and RTILs near metal electrodes in Monte Carlo simulation of the restricted primitive model,[184] while Monte Carlo simulations,[176] density function theory (DFT),[178] and modified mean

spherical approximation (MSA) theory,[185] predict bell-shaped temperature dependence. So far a widely acceptable explanation for these phenomena has not been proposed.

Hence, Section 6.3 presents an atomistic MD simulation study, as previously reported for supercapacitors using RTIL electrolytes on flat graphite, and metallic electrode surfaces,[65,134,175] on pure and mixed RTILs as electrolytes near an OLC electrode as a function of temperature. The ionic liquid electrolytes used in this study are $[C_3mpy][Tf_2N]$, $[C_4mpip][Tf_2N]$ and the equimolar mixture of these two ionic liquids.

Section 6.4 presents the performance of dicationic ionic liquids (DILs), as electrolytes in OLC-based supercapacitors. DILs, consisting of two geminal cationic rings linked by alkyl chains at different lengths, can be used as catalysts,[85,186] solvents,[88] lubricants[89] and electrolytes,[91,92] similar to applications for monocationic ionic liquids (MILs). An increasing number of studies on DILs have been recently reported. For instance, Anderson *et al*. has reported a series of DILs exhibiting high stability.[83] So far, the structural and dynamic properties of bulk DIL have been reported using molecular dynamics (MD) simulations.[15,102,103,106] However, the interfacial structure and the performance of DILs electrolytes in supercapacitors have yet to be investigated in detail. Since the structure and the molecular orientations of ions in EDLs at the surface of an electrode material play an important role in determining the energy stored in electric double layer capacitors (EDLCs),[134,187] it is of great interest to explore the role of DILs on their EDL structure and capacitive performance in contrast to that of MILs. Due to the more concentrated charge density of DILs as multivalent electrolytes compared with their monocationic counterparts, the performance of DILs is assumed to be quite different

from MILs. In this work, the influences of alkyl chain length, ion size and specific adsorption of DILs are investigated and compared with MILs.

The effects of alkyl chain length of MILs on the capacitance of supercapacitors have been widely investigated using experimental[17,18,182,188-191] and computational techniques.[192,193] Fedorov *et al*. reported the transition of the differential capacitance-electric potential (C-V) curve from the bell- to camel-shaped with the increase of the alkyl chain in MILs at graphite electrode with a common anion using Monte Carlo simulation.[192] On the other hand, Vatamanu *et al*.'s MD simulation study[193] showed that the camel-shaped C-V curve obtained from planar graphite-based supercapacitors becomes less evident as the alkyl chain length increases, which is quasi-bell shaped. Although the C-V curve from experimental measurements varies depending on the electrode materials,[191] ion types,[191,194] temperature,[17,195] and ion size,[17,191,195] the overall differential capacitance is observed to decrease with the increase of the chain length due to the thicker EDL formed by cations with longer tails.[17,191] The transition in the shape of C-V curve had not been reported experimentally until the recent study by Su *et al*., in which the transition of the bell- to camel-shaped C-V curves for Au(100)/ imidazolium-based RTILs was observed.[188] However, the effects of chain length on the C-V curve of carbon/DILs are still elusive. Thus, in this work, the imidazolium-based DILs with varying alkyl chain lengths are taken into consideration.

The relative size of the cation/anion also influences the shape of the C-V curves,[196,197] because the cation and anion dominate the EDL structure near negatively and positively charged electrodes, respectively.[198] The asymmetry of the C-V curve due to the dissimilar ion sizes was reported using mean field theory, *i.e*., smaller anions enhanced the

capacitance at positive potential, and the increased capacitance at negative potential was observed for smaller cations.[197] Considering the asymmetric ion size of dications versus anions, the C-V curve for DILs is expected to be asymmetric as well. In addition, the C-V curve is also affected by the specific adsorption of ions on electrode surface. It was reported that the adsorption of anions raises the capacitance at negative potential, whereas the capacitance is improved at positive potential by cation adsorption.[197] Therefore, the shape of C-V curve is probably determined by the co-effect of ion size and specific adsorption. In this work, molecular dynamics (MD) simulation was used to investigate the EDL structure of 1-alkyl-3-dimethylimidazolium tetrafluoroborate ($[C_n(mim)_2](BF_4)_2$, n=3,6,9) and their C-V curves. Carbon nanomaterials are presently the most common electrode materials for EDLCs because of their high specific surface area and conductivity, low density, tunable surface chemistry, and electrochemical stability.[4,199,200] Onion-like carbon (OLC) was used as the electrode material in this study because of its high specific surface area and accessible surface stemming from its small particle size and exohedral structure,[201] which will help avoid mass transport effects found in nanoporous materials, especially at low temperature due to the high viscosity of electrolytes. To probe the influence of anion type on C-V curve, the interfacial behavior and capacitive performance of $[C_6(mim)_2](Tf_2N)_2$ at an OLC surface were studied. The monocationic counterparts near the OLC surface were also modeled for comparison with DILs.

It is known that DILs are more viscous, which greatly restricts their successful applications as electrolytes for high power density supercapacitors. To overcome the relative high viscosity, organic solvents such as acetonitrile (ACN), propylene carbonate

(PC) and acetone, are commonly used as additives of RTILs to improve their conductivity [202,203] as electrolytes for supercapacitors,[92,204,205] batteries [206,207] and solar cells.[208] PC was reported to exhibit a higher density, viscosity and dielectric constant than ACN.[209] And it displays a little bit strong polarity in contrast ACN. However, ACN was found to be the most suitable solvent of RTILs for carbon-based supercapacitors since ACN/RTILs electrolytes exhibit less electric resistance and nearly constant energy density with the increase of power density.[204] For instance, Chaban *et al.* reported that the ionic conductivity of RTILs was increased more than 50 times by addition of ACN with high diffusion coefficients and low viscosity using molecular dynamics simulation.[210] Experimentally, the excellent capacitive performance of DILs in contrast to MILs was solely observed in cyclic voltammetry at extremely slow scan rate.[211] Whereas, the addition of ACN or PC into DILs favors the higher capacitance of DILs than the counterparts MILs even at high scan rate (400 mV s^{-1}).[92]

Although the influence of organic solvents on the electric double layer (EDL) of MILs near carbon electrode has been reported,[212-215] the molecular insight into the EDLs formed by DILs/organic solvents near carbon electrode is still elusive. Merlet *et al.* reported that the organic solvent ACN reduced the layering of MILs in EDLs, facilitated the dissociation of cation-anion pairs and attenuated the dissymmetry between positive and negative potentials.[213] The capacitance of ACN/RTILs-based electrolytes in supercapacitors was slightly increased compared with neat RTILs-based supercapacitors in molecular dynamics (MD) simulations[214]; whereas density function theory (DFT) revealed an enhanced capacitance in carbon nanoslits once the organic solvents were involved.[215] However, despite the benefits of using ACN as a solvent for RTILs, the

influence of ACN solvent on the capacitance of DILs-based supercapacitors, especially on the shape of the differential capacitance – electric potential (C-V) curves is poorly understood. This study will be presented in Section 6.5.

6.2 Simulation Details

All the simulations in this work were performed using MD package Gromacs. Exp-6 force field is used for both pure and their binary mixture, which is the modified Atomistic Polarizable Potential for Liquids, Electrolytes and Polymers (APPLE&P) force field developed by Borodin.[155] The only modification applied herein is excluding the polarizability terms from APPLE&P force field in order to ensure its executability in MD package Gromacs without counterbalancing its accuracy. The force field used for dications $[C_n(mim)_2]$ (n = 3, 6, 9) was adapted from the all-atom force field developed by Yeganegi *et al.*,[106] which has been validated to reproduce the experimental density with high accuracy. The force fields for monocations and anions were taken from the study of Lopes's group.[107] The van der Waals interaction parameters for carbon of the OLC electrode were taken from Cornell *et al.*'s study.[216] The new six-site model was used for the simulation of acetonitrile (ACN) [217], which has been successfully used to model the mixture of ILs and ACN.[210] All the parameters for propylene carbonate (PC) in MD simulation were taken from generalized Amber force field (GAFF) [218] with optimized partial charges obtained from Yang *et al.*'s work.[219]

For diffusion and conductivity calculation, a cubic box consisting of 250 ions pairs were used with periodic boundary condition applied along all the directions. The PME method was used to calculate the electrostatic interaction with a cutoff of 1.1 nm. All the bonds were constrained using LINCS algorithm. Simulated annealing was conducted by

heating the system to 1000 K and then gradually decreased to required temperature within 4 ns. The simulation was conducted in NPT ensemble at 373 K, 323 K, 298 K, 273 K, 248 K and 223 K respectively. Noose-Hover thermostat was applied to control the temperature coupling. For all the aforementioned simulations, the pressure was maintained at 1 bar using Parrinello-Rahman barostat. For each system, three independent simulations with different initial configurations were performed to ensure statistical accuracy. The mean square displacement (MSD) of C_4mpip+ in neat [C_4mpip][Tf_2N] verified that systems were sufficiently equilibrated even in low temperature region. The conductivity (λ) was estimated using Nernst-Einstein approximation

$$\lambda = \frac{e^2}{Vk_BT}(n_+D_+ + n_-D_-) \qquad (6.1)$$

where e is unit electron, V is the volume of simulation box, k_B is Boltzmann constant, T is temperature; n_+, n_- represent number of cations and anions; D_+, D_- represent diffusioncoefficients for cations and anions, respectively.

In the simulation of the supercapacitor system, the simulation boxes containing bulk [C_3mpy][Tf_2N], [C_4mpip][Tf_2N] or 1:1 mixture were firstly equilibrated under NPT ensemble, respectively. The exohedral OLC (C_{720}) with the radius of 1.22 nm was then immersed into the geometrical center of the box. In order to acquire the bulk-like RTILs behavior beyond the electrode surface, the box size is set to no less than 8 nm. The system at varying temperature was further equilibrated under NPT with periodic boundary condition applied along all the directions. Throughout the simulation, the OLC is static in the center of box. After simulated annealing, the system was further equilibrated under NPT for 4 ns followed by another 4 ns production run. For simulation

at low temperature (248 K), additional equilibration time (approximately 20 ns) is required. The trajectory was saved every 50 fs for obtaining number /charge density profile by binning method. For charged electrode, the charge is evenly assigned to each carbon atoms of the OLC. The number of cations or anions is adjusted to keep the charge neutrality of the system. The electric potential ϕ_{EDL} is calculated by solving Poisson equation. The differential capacitance was calculated according to $C_d = \frac{d\sigma}{d\phi_{EDL}}$ by local fitting of the surface charge density (σ) as a function of electric potential (ϕ_{EDL}). Three individual runs with different initial configurations were performed for statistical accuracy.

For dicationic ionic liquids, the OLC electrode with a radius of 1.22 nm was fixed in the center of a cubic box filled with ~1000 ion pairs initially at low density. The equilibration was performed in the isobaric-isothermal ensemble at 1 bar and 800 K for 2 ns, followed by annealing the simulation to 450 K for $[C_n(mim)_2](BF_4)_2$ and 300 K for $[C_6(mim)_2](Tf_2N)_2$. The production runs were then conducted at 450 K in the NPT ensemble to ensure that $[C_n(mim)_2](BF_4)_2$ and $[C_6mim][BF_4]$ were in the liquid phase and the simulation was implemented at 300 K for $[C_6(mim)_2](Tf_2N)_2$ and $[C_6mim][Tf_2N]$ because of their low melting points. The timestep of 1 fs was applied and the trajectory was saved every 100 fs for computing the number and charge density profiles. The final box size is within 9-10 nm so that the ionic liquids far from the electrode surface exhibit bulk-like behavior. A 4-ns production run generated was used for further analysis.

For DILs/organic solvent electrolytes, the simulation is setup as follows: a distance of 7 nm between positively and negatively charged graphites was applied with a vacuum space of 28 nm (in length) in-between of the simulation cell. The three-layer graphite

electrode with the size of 4.18 nm × 4.25 nm was fixed during the simulation. The density of electrolytes in the central portion of a planar graphite cell is tuned to the bulk density. The equilibration was performed in the canonical ensemble at 300 K for 10 ns after annealing from 1000 K to 300 K. All the production runs were then conducted at 300 K. The timestep of 2 fs was applied and trajectory was saved every 100 fs for computing the number and charge density profiles. A 6-ns production run generated at 300 K was used for further analysis. Different electric potentials were created by partial charge uniformly distributed on the graphite layer in contact with electrolytes at varying charge densities. The potential drop was calculated using Poisson equation as in previous study [220].Energy density of supercapacitors is calculated using the following equation:

$$E = \frac{1}{2} C_{\text{int}} V_t^2 \qquad (6.2)$$

where C_{int} is integral capacitance and V_{t} is the total potential drop between positively and negatively charged electrodes.

6.3 Capacitive Behavior of Monocationic Ionic Liquids

6.3.1 Conductivity and Phase Transition Temperature of Mixture

The typical property of a eutectic mixture is the lowering of the melting (T_{m}) and glass transition temperature (T_g) in contrast to those of its individual components. The eutectic property of the 1:1 (by molar ratio) mixture of $[C_3mpy][Tf_2N]$ and $[C_4mpip][Tf_2N]$ was first examined by differential scanning calorimetry (DSC). The glass transition temperatures for $[C_3mpy][Tf_2N]$ and $[C_4mpip][Tf_2N]$ were approximately 276 K and 197 K, respectively. In contrast, the mixture exhibited a T_g of 190 K, slightly lower than the T_g of $[C_4mpip][Tf_2N]$. This result suggests that the binary mixture may solidify at a lower temperature than either pure RTIL, thus suggesting that the mixture will

exhibit higher diffusion and ionic conductivity at the same low temperature region as the pure fluids. The conductivity for the pure and mixed RTILs obtained from both experiment and MD simulation, is shown in Figure 6.1.

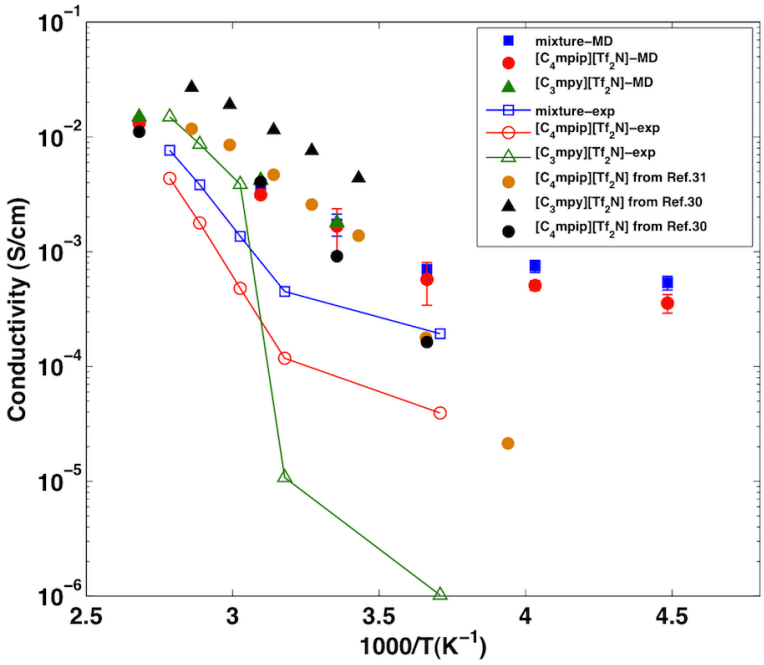

Figure 6.1. Conductivity obtained from experiment and MD simulation as a function of temperature for [C_3mpy][Tf_2N], [C_4mpip][Tf_2N] and their binary 1:1 mixture.

Due to experimental limitations for conductivity measurements, the temperature range for conductivity measurements was between 300 K and 360 K. In MD simulation, the conductivity was estimated using Nernst-Einstein approximation. The highest temperature applied was 373 K and the lowest temperature taken herein for each type of RTIL was above their T_g. For both, experiment and MD, it is seen that the conductivity decreases as temperature decreases. At a high temperature range, [C_3mpy][Tf_2N] exhibited higher conductivity than [C_4mpip][Tf_2N] and the equimolar mixture. As temperature decreases, the conductivity of [C_3mpy][Tf_2N] is dramatically reduced by 2-3 orders of magnitude (Figure 6.1). However, a less pronounced decrease in conductivity

for [C_4mpip][Tf_2N] and the binary mixture in the high temperature range were observed from both experiment and MD results. Due to the lower T_g, [C_4mpip][Tf_2N] and the binary mixture, remain in the liquid state at lower temperatures, thus exhibiting much higher conductivity than [C_3mpy][Tf_2N]. As the temperature decreased to 273 K in MD simulation, a more significant discrepancy between the conductivities of the binary mixture and that of [C_4mpip][Tf_2N] was observed, with the highest conductivities found for the former. Both MD and experiment point to the use of the binary mixture as a low-temperature electrolyte. According to Simon *et al.,*[16] the binary mixture of RTILs exhibited approximately 5-7 orders of magnitude higher conductivity compared to neat RTILs at low temperature ranges. In this study, at the lowest temperature of 223 K, the conductivity of the binary mixture is approximately 1.5 times of that of [C_4mpip][Tf_2N]. Additionally, while previous experimental conductivity measurements[221,222] showed a decrease of several orders for [C_4mpip][Tf_2N] as the temperature declined from 373 K to 250 K, our MD results exhibited only several times of magnitude reduction. These differences indicated that at high temperature, the simulation correctly predicts the conductivity, both qualitatively and quantitatively; at lower temperature, the simulation does not accurately estimate the quantitative changes, which likely reflect limitations of the force field at low temperatures.

6.3.2 EDL Microstructure and C-V curve

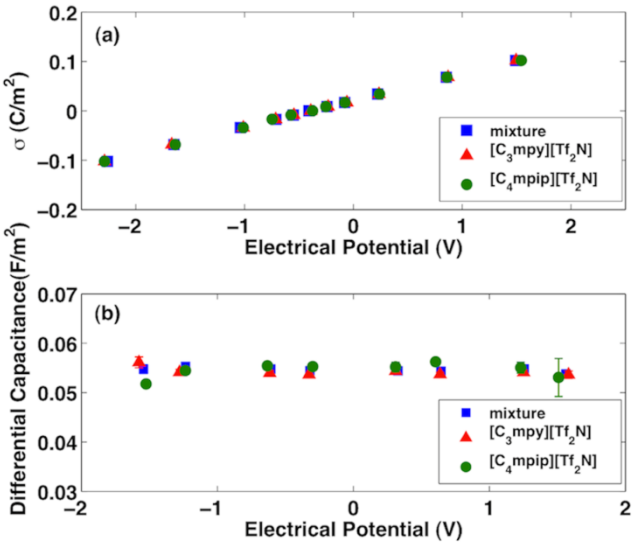

Figure 6.2. a) Surface charge density as a function of electrical potential drop for $[C_3mpy][Tf_2N]$, $[C_4mpip][Tf_2N]$ and their equimolar binary mixture at 373 K; b) The differential capacitance as a function of electrical potential for $[C_3mpy][Tf_2N]$, $[C_4mpip][Tf_2N]$ and their equimolar binary mixture at 373 K.

The differential capacitances (C_{EDL}) for $[C_3mpy][Tf_2N]$, $[C_4mpip][Tf_2N]$ and equimolar mixture were calculated, respectively. Their surface charge densities as a function of potential drop at 373 K are shown in Figure 6.2a. These exhibit a linear-like relationship with the potential drop for neat and mixed RTILs, indicating that their differential capacitances were equal throughout the potential according to the definition $C_d = \frac{d\sigma}{d\phi_{EDL}}$ (σ, surface charge density of the electrode; ϕ_{EDL}, potential drop across the EDL). Moreover, regardless of the potential applied, the differential capacitances were ~ 0.054 F/m^2. The differential capacitance for all investigated samples, shown in Figure 6.2b, further suggests that the differential capacitance was identical for both neat and mixed RTILs and is independent of the potential applied. A potential-independent

differential capacitance was also observed for 1-ethyl-3-methylimidazolium bis(trifluoromethylsulfonyl)imide ([emim][Tf_2N]) near OLC electrode.[223] Our results demonstrate that this is also applicable to piperidinium-based RTILs, pyrrolidinium-based RTILs, as well as their binary mixture. This phenomenon has been explained by the dominant role of the charging overscreening at curved electrode surface as the applied potential varies.[223] Recently, Yan *et. al*. proposed that specific adsorption led to the discrepancy of differential capacitance at positively and negatively charged electrodes, which indicates that the lack of specific adsorption may be another reason causing potential independent differential capacitance.[224] In the present study, [C_3mpy][Tf_2N] and [C_4mpip][Tf_2N] exhibited equivalent differential capacitance, revealing similar EDL structure near OLC. Furthermore, the number density profile for three types of electrolytes at 373 K near neutral and charged OLC shows that [C_3mpy+] is approximately 10% smaller than [C_4mpip+] in size, therefore, the number density in EDL of [C_3mpy][Tf_2N] is slightly higher than that of [C_4mpip][Tf_2N]. However, owing to the small differences in molecular weight and size between [C_3mpy][Tf_2N] and [C_4mpip][Tf_2N], their EDLs are very similar, resulting in similar EDL structure for their equimolar mixture.

6.3.3 Temperature Effects on Capacitance

To achieve extension of the operating temperature range for supercapacitors, the influence of temperature on the performance of supercapacitors requires in-depth investigation. In Figure 6.3a, a linear dependence of the surface charge density for the binary mixture as a function of the potential applied is presented at the temperatures of 248 K, 298 K and 373 K, respectively. The differential capacitance, obtained from the

slope of the linear fitting, increases with increasing temperature (*i.e.* 0.044 F/m^2 at 248 K, 0.051 F/m^2 at 298 K and 0.054 F/m^2 at 373 K). The differential capacitance for the binary mixtures at 248 K, 298 K and 373 K are shown in Figure 6.3b, which reveals the same trend in temperature dependence.

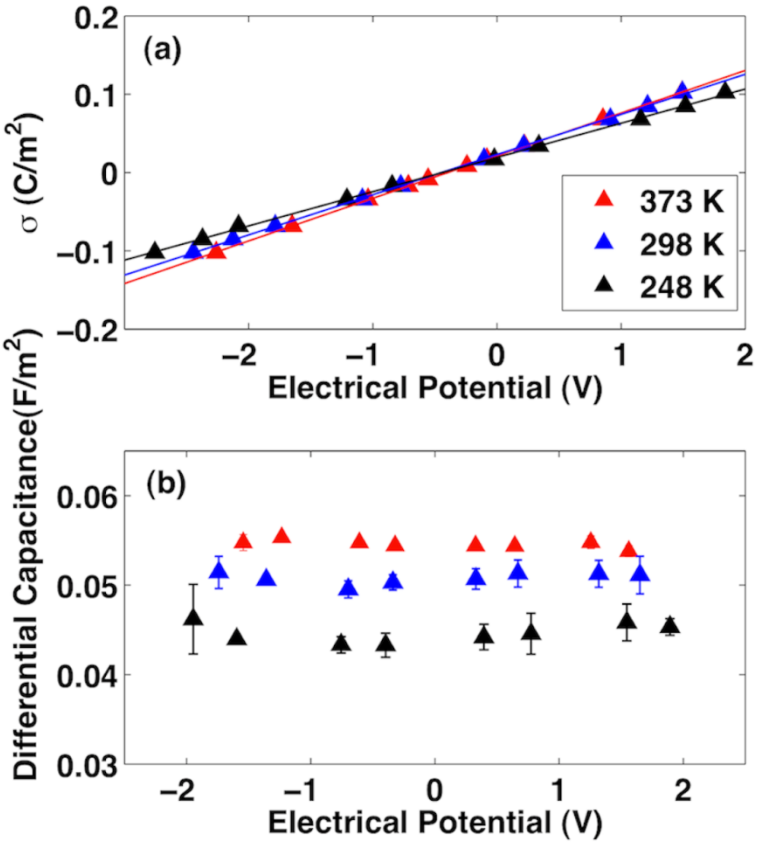

Figure 6.3. a) Surface charge density as a function of electrical potential drop for binary mixture at 248 K, 298 K and 373 K; b) The differential capacitance as a function of electrical potential for the binary mixture at 248 K, 298 K and 373 K.

The classical Gouy-Chapman theory predicts that the electrical capacitance decreases as temperature increases (referred to as negative temperature dependence).[185] However, a series of experiments using RTILs as electrolytes obtain the reverse trend.[17,18,173,174] High temperature molten salts were found to possess the positive temperature dependence of

capacitance as well.[180,181] Kornyshev has pointed out that the Gouy-Chapman model is not appropriate for highly condensed ionic liquids.[225] Computational studies using molecular dynamics simulation of RTILs electrolytes near planar graphite surfaces exhibit negative temperature dependence.[175] In contrast, MSA-MC theory discloses that at a low temperature range, the capacitance increases with temperature (positive temperature dependence), going through a point of maximum, beyond which the capacitance decreases with further temperature increase.[176,185] Even though positive temperature dependence was observed in several experiments using RTILs electrolytes, our results show the first observation of positive temperature dependence in MD simulations. To date, an acceptable explanation for this trend has not been proposed. Studies by Boda *et al*.[179,185] confirm that the positive temperature-dependent capacitance is more than a simple a density effect, being related to the ionic pairs association, whereas such ion association increases as temperature decreases. A possible interpretation for this phenomenon is that fast dissociation of ions at high temperature results in a thinner EDL thickness, hence increasing the capacitance.[191]

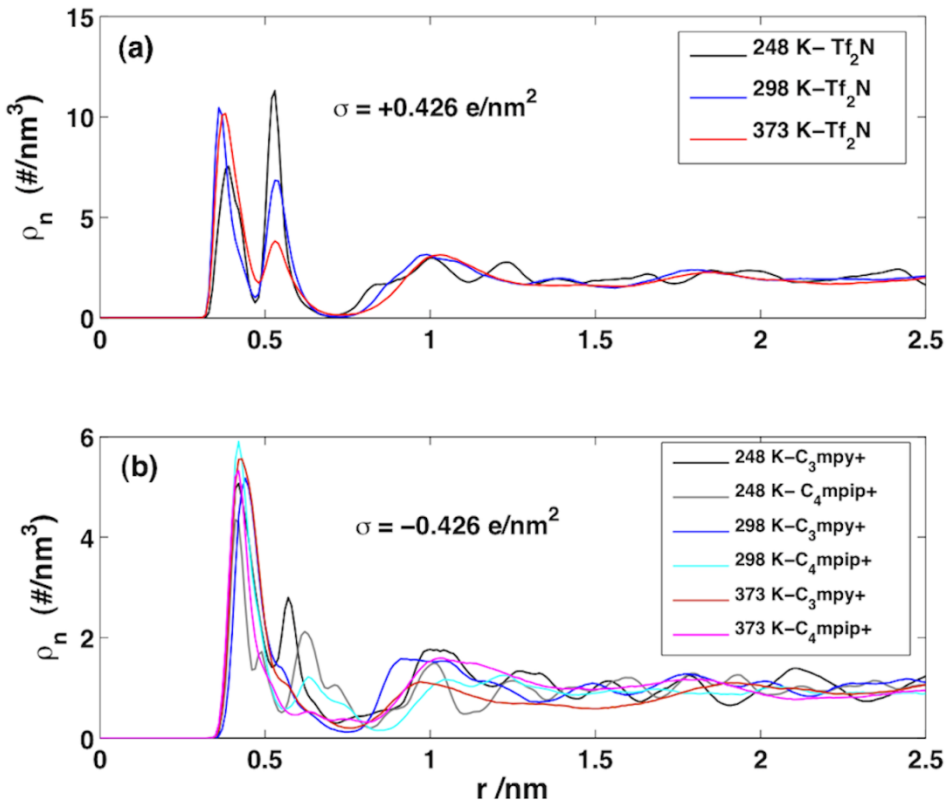

Figure 6.4. Number density profile for binary mixture at (a) positively charged and (b) negatively charged OLC at 248 K, 298 K and 373 K.

To illustrate the influence of temperature on the EDL thickness, Figure 6.4 shows the number density profile for counter-ions near a positively (Figure 6.4a) and a negatively (Figure 6.4b) charged OLC electrode. Previous investigations demonstrated that at charged surfaces, the EDL structure is dominated by the counter-ions rather than co-ions due to strong electrostatic attraction.[134] Due to the overscreening of counter ions near charged electrodes, alternating layers of counter-ions and co-ions form near the electrode to balance its net charge. Far from the electrode, there is no such layering formation owning to the weak electrostatic interaction between the electrode and and ions.[136] From Figure 6.4, the second layer of EDL becomes more evident as temperature decreases

from 373 K to 248 K, suggesting that the EDL thickness increases as temperature decreases.

To quantify the EDL thickness, the effective thickness d_{eff} is introduced, which is calculated using the formula derived from Ref. 136[136]:

$$d_{eff} = \frac{\int_{R}^{r} s^2 (s-R)\rho^{n}_{counter-ions}(s)ds}{\int_{R}^{r} s^2 \rho^{n}_{counter-ions}(s)ds} \qquad (6.3)$$

s is the distance between electrode surface and center of mass of ions; $\rho^{n}_{counter-ions}(s)$ is the number density profile of counter ions.

d_{eff} for binary mixture at 248 K, 273K, 298 K, 323 K and 373 K was calculated and shown in Figure 5a. Due to the near-flat differential capacitance as a function of applied potential, herein, d_{eff} is only shown at the potential of ~ 1.5 V .

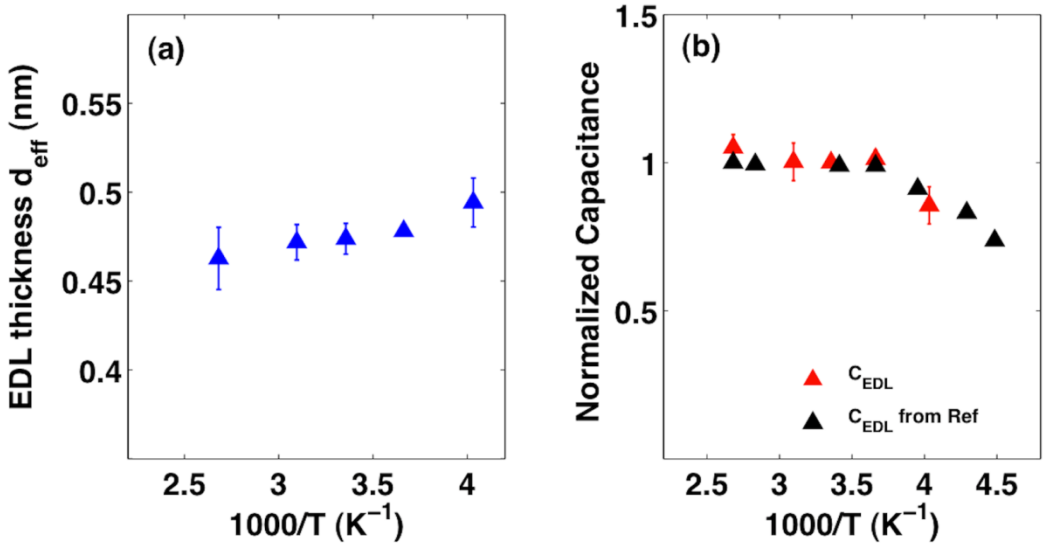

Figure 6.5. (a) EDL thickness (d_{eff}) as a function of temperature (b) and normalized capacitance ($C_{EDL}/C_{EDL,298K}$) for the binary mixture near OLC in comparison with normalized capacitance ($C_{EDL}/C_{EDL,293K}$) taken from Ref.16[16] as a function of temperature.

The capacitances of varying temperatures at σ = 0.426 *e/nm*^{2} were chosen due to the near-flat curve of capacitance versus electrical potential.

In OLC-based supercapacitors, the capacitance can be simplified as[226]

$$C_{EDL} = \varepsilon(\frac{1}{R} + \frac{1}{d_{eff}}) \qquad (6.4)$$

where ε is the dielectric constant of the EDL, R is the radius of the OLC (C_{720} herein) and d_{eff} is the thickness of the EDL structure. This formula reveals that at fixed temperature, the differential capacitance will increase as the size/radius of OLC decreases, which has been demonstrated in Ref. 13.[13] The effective thickness d_{eff} was found to increase with decreasing temperature, as shown in Figure 6.5a, demonstrating the positive temperature dependence. Currently, it is still difficult to experimentally measure the interfacial dielectric constant, though its temperature-dependence and effects on the EDL cannot be completely excluded. However, as shown in Figure 6.5b, the positive temperature-dependent normalized capacitance for the binary mixture as a function of temperature, which is in good agreement with experimental results,[16] despite different RTILs being studied. Furthermore, when the temperature was lowered from 373 K to 248 K, less than 20% of the differential capacitance was lost, showing that OLC-RTILs supercapacitors are suitable for low temperature use.

Although previous experimental work related the positive temperature dependence to the EDL thickness, the experimental or theoretical verification were pending. The present computational study demonstrates that the origin of the positive temperature dependence is correlated to the thinning of the EDL with increasing temperatures. Thus, these results

may allow for the future design and improvement of low-temperature operated supercapacitors and electrolytes without diminishing their capacitive performance.

6.3.4 Conclusion

In summary, this study demonstrated that the binary mixture of RTILs outperformed neat RTILs as supercapacitor electrolytes with widened operation temperature, higher conductivity and a near-flat differential capacitance as a function of electric potential. The positive temperature dependence of the differential capacitance dominated by the EDL thickness provides a theoretical model for interpreting the experimentally observed positive temperature dependence.

6.4 Capacitive Behavior of Dicationic Ionic Liquids

6.4.1 Electrical Double Layer Structure

The number density profiles based on the center of mass of cations and anions, respectively, in DILs as a function of the distance from the charged/uncharged OLC surface are presented in Figure 6.6. Layering of cations and anions near the OLC surface is present for both dicationic $[C_n(mim)_2](BF_4)_2$ (n = 3, 6, 9) and monocationic $[C_6mim][BF_4]$ regardless of the electrode's charge. In contrast to monocationic $[C_6mim][BF_4]$ (Fig 6.6d, h), the cation number density of $[C_n(mim)_2](BF_4)_2$ in the layer closest to OLC is evidently lower. Due to the large size and more concentrated charge density of dications, fewer are accumulated on the OLC surface, which is sufficient to counterbalance the opposite charges on the electrode surface. Moreover, a cation layer with twin peaks is formed near the neutral OLC surface for $[C_3(mim)_2](BF_4)_2$, whereas predominantly one dense layer of cations is observed for $[C_6(mim)_2](BF_4)_2$, $[C_9(mim)_2](BF_4)_2$ and monocationic $[C_6mim][BF_4]$. With the increase of the chain length,

fewer cations are observed in EDLs, which is due to the decreased packing efficiency of the bigger dications. Because of the more concentrated charge density in dications, more anions in DILs are accumulated in the layer near OLC surfaces. Such a trend is consistent with that reported in MILs.[227,228] For charged electrodes, the number of counter-ions in EDLs increases as the chain length decreases.

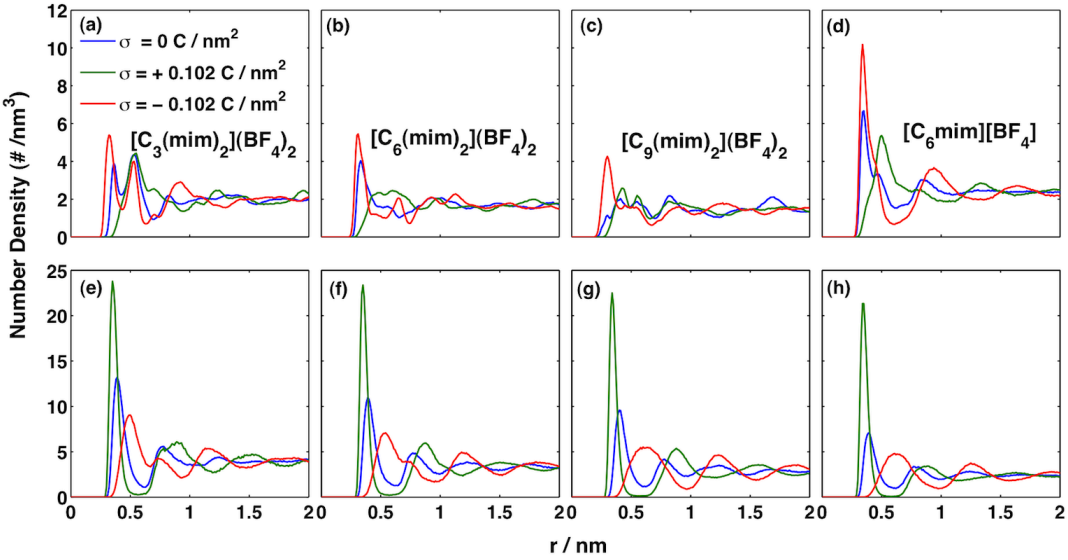

Figure 6.6. Number density profile for dicationic $[C_n(mim)_2](BF_4)_2$ (n = 3, 6, 9) and monocationic $[C_6mim][BF_4]$ ionic liquids at OLC surface, calculated from MD simulations. The top panel (a-d) is for cations and bottom panel (e-f) is for anions.

To disclose more details of the interfacial structure of dications near the OLC surface, the orientational order parameter of dications near charged/uncharged OLC surfaces was calculated using $\langle P_2 \rangle = \frac{1}{2}(3\cos^2\theta - 1)$ as shown in Figure 6.7. The orientational order parameter describes the distribution of angles formed by the cation chain or cation ring versus OLC surface (see cartoons in Figure 6.7). To describe the orientation of the cation chain, the angle was defined as angles formed by the linkage alkyl chain in DILs and the

normal of OLC surface. As shown in Figure 6.7a-c, the results suggested that the alkyl chains of cations in the first layer adsorbed on the OLC electrode tend to be parallel with the electrode surface regardless of the chain length or surface charge density, whereas those in the second layer tend to be perpendicular to the electrode surface. The latter is enhanced with the increase in negative charge density of the electrode except for $[C_9(mim)_2]$. The longer alkyl chain in $[C_9(mim)_2]$ with high flexibility may result in the more random arrangements relative to the electrode surface. For the cations beyond the second layer, there is no obvious orientational preference observed for the alkyl chains, consistent with observation of MILs.[228] To show how the cation ring is oriented, the angle defined is between the plane of the cation ring and the normal to the OLC surface. As shown in Figure 6.7d-f, at the OLC surface, the imidazolium plane tends to be parallel with the OLC surface, which facilitates the efficient packing of dications for better screening of the charged electrode. Meanwhile, the tendency of vertical imidazolium plane in the second layer of EDLs is inspected. These observations imply that the imidazolium rings of DILs adopt the similar orientation near carbon surface as reported for those in MILs.[227,229]

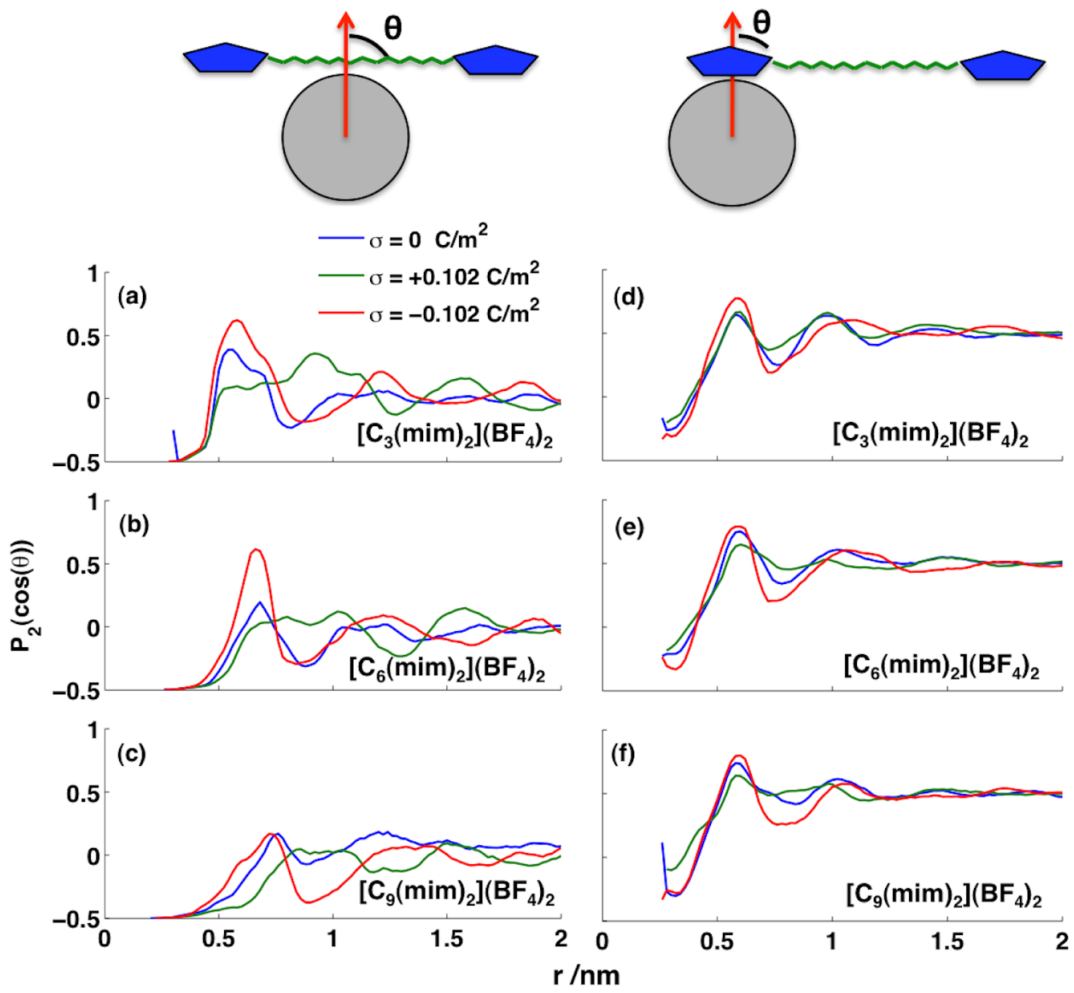

Figure 6.7. Orientational order parameter as a function of distance from OLC surface for the alkyl chain (a-c) and the imidazolium rings (d-f) in $[C_n(mim)_2](BF_4)_2$ (n = 3, 6, 9). The left panels (a-c) are for angles formed between the linkage alkyl chain in DILs and the normal to the OLC surface; the right panels (d-f) are for angles between the plane of the imidazolium ring and the normal to the OLC surface.

6.4.2 Capacitive Performance of $[C_n(mim)_2](BF_4)_2$

The C-V curves near OLC electrodes for DILs $[C_n(mim)_2](BF_4)_2$ (n=3, 6, 9) with varying linkage chain lengths are shown in Figure 6.8a. The near-flat C-V curve featured OLC/RTIL supercapacitor has been reported in our previous studies.[13,14] However, in this

work, differently shaped C-V curves were observed (Figure 6.8), where the differential capacitance at the negatively charged electrodes is higher than that at the positively charged electrodes. The shape of C-V curves is determined by multiple factors such as electrode materials, ion sizes, temperature, and different RTILs adopted.[13,14] In previous work, we chose RTILs (*i.e.* $[C_2mim][Tf_2N]$,[13] $[C_3mpy][Tf_2N]$,[14] $[C_4mpip][Tf_2N]$[14]) with cations and anions of similar sizes, which partially accounts for the near-flat C-V curve observed. In this study, the cation size is approximately 2-4 times that of the BF_4^- anion and the charges cation carries are twice of that for the anion. This feature causes the favorable adsorbing and desorbing of more anions than cations in the EDL at the same potentials, since smaller anions can fit in a given volume.[65] Lauw *et al*. used mean field theory to demonstrate that for RTILs with dissimilar cation/anion sizes, the shape of the C-V curve is dominated by the size of the counter-ions, *i.e*., the smaller counter-ion size leads to the enhanced differential capacitance.[197]

In addition, negative potential of zero charge (PZC) indicates affinity of anions towards an electrode while positive PZC suggests preferential specific adsorption of cations.[197] The values of PZC for $[C_n(mim)_2](BF_4)_2$ are +0.10 V (n = 3), +0.18 V (n = 6) and +0.20 V (n = 9) and the PZC of $[C_6mim][BF_4]$ is +0.30 V. Based on these values, cations are preferred to be adsorbed on OLC surface and the adsorption strength of dications increases with increasing chain length. Compared with dications, the adsorption of monocationic C_6mim+ is favorable for OLC, and this adsorption of cations suggests the enhanced capacitance at positive potentials.[197] The combined effects of specific adsorption and ion size can well explain the shape of the C-V curves with higher capacitance at positively charged electrode shown in Figure 6.8. Similarly, BF_4-

containing MILs have been reported to exhibit asymmetric C-V curves as well, due to the dissimilar cation/anion sizes.[182,230-232]

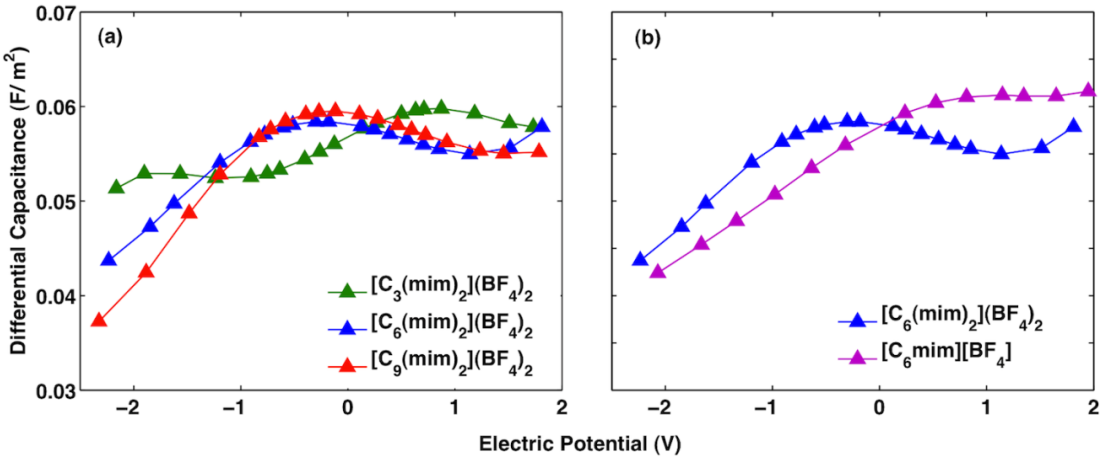

Figure 6.8. Differential capacitance-electrical potential (C-V) curves for $[C_n(mim)_2](BF_4)_2$ (n=3,6,9) (a) and dicationic $[C_6(mim)_2](BF_4)_2$ versus monocationic $[C_6mim][BF_4]$ (b) from MD simulation.

The comparison of the C-V curves of dicationic $[C_6(mim)_2](BF_4)_2$ and monocationic $[C_6mim][BF_4]$ shown in Figure 6.8b highlights the slightly higher capacitance of $[C_6(mim)_2](BF_4)_2$ than $[C_6mim][BF_4]$ at negative potential and the reverse trend at positive potentials. However, Tf_2N-containing DILs display higher capacitance than MILs throughout the potential applied, which will be discussed later. The trend of C-V curves for BF_4-containing DILs and MILs suggest the better screening of anions in DILs than MILs at negative potentials and the more efficient screening of monocations than dications at positive potentials. In general, there is no significant enhancement of capacitance for DILs compared with MILs, probably due to their similar screening efficiency, which is shown in Figure 6.9.

To evaluate the screening effects, a charge-screening factor is quantitatively defined by the equation below as,[13]

$$C_f(r) = -\int_R^r \frac{s^2}{R^2}\Delta\rho_e(s)ds/\sigma \qquad (6.5)$$

where s is the distance from the electrode, $\Delta\rho_e(s)$ is the change of charge density profile between charged and neutral electrode, R is the radius of OLC and σ is the electrode surface charge density. The charge screening factor for RTIL $[C_2mim][Tf_2N]$ is relatively constant with increasing surface charge density, and this factor was used to interpret the near-flat C-V curve for OLC-based supercapacitors in our previous work.[13] Herein, the calculated charge screening factors (C_f) for $[C_n(mim)_2](BF_4)_2$ at both positive and negative potentials are shown in Figure 6.9. The peak intensities in C_f decrease (longer chain, larger decrease) as the charge density/electric potential of the negative electrode increases, whereas a relatively insignificant variation in peak intensity is observed at the positive electrode. These trends agree with the decrease of differential capacitance (Figure 6.8) with increasing electric potential drop at negatively charged surfaces and the subtle variation in differential capacitance at positively charged surfaces. Such phenomena are related to the packing of counter-ions in EDLs near the OLC electrode. At a high potential on the negatively charged surface, the differential capacitance decreases with increasing chain length or cation size. This trend corresponds to the decreasing screening factors with the elongation of chain length (Figure 6.8). Moreover, the number of anions in EDLs near the positively charged electrode increases linearly with the surface charge density; therefore a near-constant screening factor was observed for the positively charged electrode. Conversely, for the negatively charged electrode, the number of cations does not increase linearly with the surface charge density, due to the

complicated geometry, large size and orientation of dications in EDLs. This observation is confirmed by examining the cumulative number density of ions, shown in Figure 6.10.

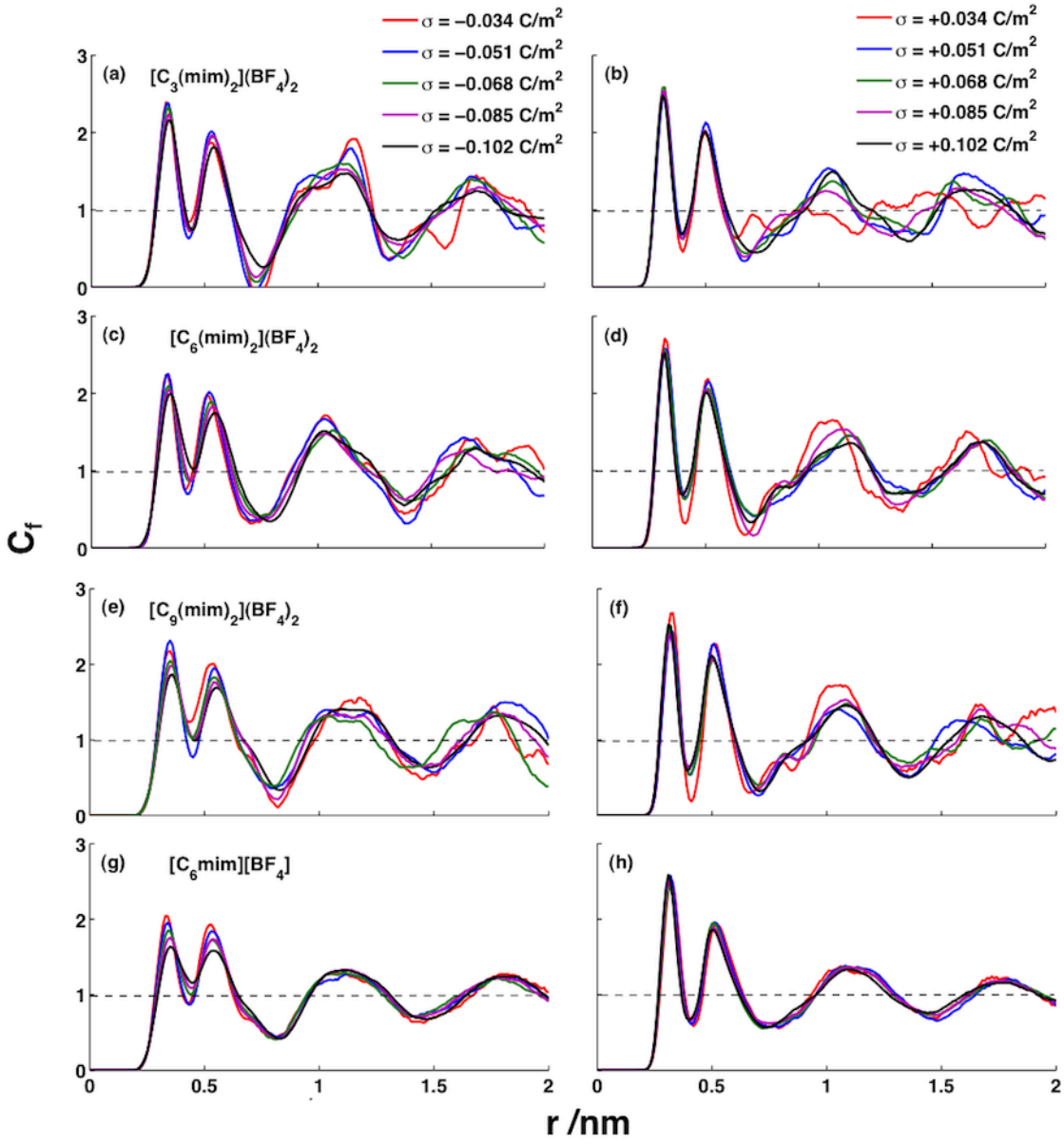

Figure 6.9. Charge screening factors for dicationic $[C_n(mim)_2](BF_4)_2$ (n=3, 6, 9) and monocationic $[C_6mim][BF_4]$ at varying charge densities of electrode surface. The left panel is for the negatively charged electrode corresponding to an electric potential between -0.5 ~ -2,0 V and the right panel is for the positively charged electrode at an electric potential between 0.5 ~ 2.0 V.

The cumulative number density of ions, *i.e.*, the number of ions per unit area of electrode within the first layer (0 ~ 0.7 nm) of EDLs, was calculated as shown in Figure 6.10. The results indicate that more anions of $[C_n(mim)_2](BF_4)_2$ than cations were found to accumulate in EDLs near the positively charged electrodes, which contributes to the more efficient screening of smaller-sized anions. This is also reflected in the number density profile of Figure 6.6, which demonstrates that the anions are packed denser than the cations at either neutral or charged OLC surfaces. Moreover, the number of anions accumulated in EDLs exhibits a linear-like relationship with increasing electric potential at the positive electrodes, but not for cations at the negative electrodes, which is consistent with the variation of screening factors. On the other hand, the effect of the linkage chain length on the differential capacitance (*i.e.*, in Figure 6.8a, the C-V curve for $[C_3(mim)_2](BF_4)_2$, $[C_6(mim)_2](BF_4)_2$ and $[C_9(mim)_2](BF_4)_2$) can be deduced from the cumulative number density. First, the bell-to-camel shape transition of the C-V curve is not observed with an increase in the linkage chain length. Compared with the MD simulation study by Vatamanu *et al.*,[193] however, the obtained C-V curves in Figure 6.8 cannot be classified into bell-, camel- or U-shaped. The replacement of BF_4 anions used in this study with larger-sized anions may change the C-V curve shapes, and this was verified in the C-V curve of $[C_6(mim)_2](Tf_2N)_2$ (Figure 6.11a).

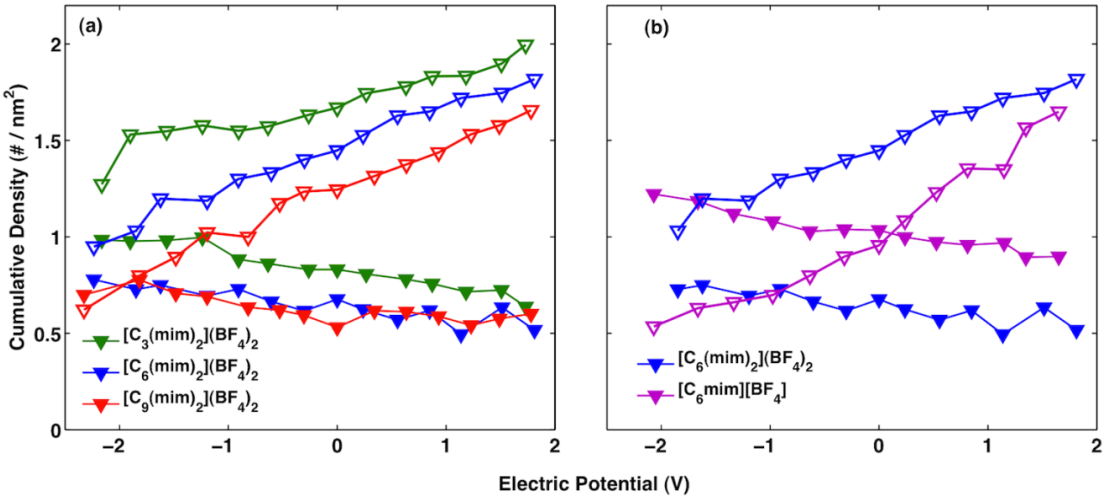

Figure 6.10. Cumulative density of ion's center-of-mass in the electric double layer as a function of electric potential applied from MD simulation for $[C_n(mim)_2](BF_4)_2$ (a) and $C_6(mim)_2](BF_4)_2$ versus monocationic $[C_6mim][BF_4]$ (b). The solid symbols denote cations and hollow symbols are for anions.

Comparing the C-V curve of monocationic $[C_6mim][BF_4]$ with that of dicationic $[C_6(mim)_2](BF_4)_2$, the higher anion density of EDLs in DILs compared to that of MILs, shown in Figure 6.10b, causes a more efficient screening by the positively charged electrode. The cumulative number densities of $[C_6(mim)_2](BF_4)_2$ and $[C_6mim][BF_4]$ at varying potentials indicate that more anions of $[C_6(mim)_2](BF_4)_2$ are adsorbed in EDLs compared to those in monocationic $[C_6mim][BF_4]$, which is also the case for $[C_6(mim)_2](Tf_2N)_2$ and $[C_6mim][Tf_2N]$. For the cumulative number density of cations, although a smaller amount of dication $[C_6(mim)_2]$ is accumulated in EDLs, there is a higher concentration of positive charges in EDLs of $[C_6(mim)_2](BF_4)_2$ than in monocationic $[C_6mim][BF_4]$. From Figure 6.10, it is concluded that anions accumulate more rapidly than cations with increasing electric potential, which results in a higher

differential capacitance at the positively charged electrode than at the negatively charged one.

6.4.3. C-V curves of $[C_6(mim)_2](Tf_2N)_2$ versus $[C_6mim][Tf_2N]$

To investigate the role of anions in EDLs, we replaced the anion of BF_4- with Tf_2N- and observed a different collection of C-V curves, as shown in Figure 6.11. Compared with MIL $[C_6mim][BF_4]$, a relative flatter C-V curve is observed in $[C_6mim][Tf_2N]$, which is also similar to previous studies[13,14] and explained by the relatively constant screening factors at both positively and negatively charged electrodes. Moreover, like $[C_n(mim)_2](BF_4)_2$, differential capacitance decays at high negative potential for $[C_6(mim)_2](Tf_2N)_2$. Lauw *et al.*'s mean field theory has demonstrated that not only ion size but also specific adsorption contributes to the asymmetry of the C-V curve; smaller anions raise the capacitance at positive potential and specific adsorption of anions increases the capacitance at -1.2 ~ -0.3 V for ILs with cations and anions of equal size.[60,197]

As discussed above, the affinity of the ions toward the electrode also plays a role.[197] The values of PZC for $[C_6(mim)_2](Tf_2N)_2$ and $[C_6mim][Tf_2N]$ are -0.2 V, and -0.1 V, respectively. This indicates that Tf_2N- is preferentially adsorbed on the OLC surface and the adsorption strength of cations on the OLC surface is in the order: C_6mim+ > $C_6(mim)_2+$. Combining the ion size effect and specific adsorption in the case of $[C_n(mim)_2](BF_4)_2$, both the smaller size of anions and the stronger specific adsorption of cations enhance the capacitance at positive potentials. In Tf_2N-containing ILs, the Tf_2N- anion, which is larger than BF_4-, reduces the capacitance at positive potentials, and the strong adsorption of Tf_2N- raises the capacitance at negative potentials, thus yielding the

near-flat C-V. Additionally, the size ratios of $C_6(mim)_2$+ : Tf_2N- and C_6mim+:Tf_2N- are 7:4 and 5:4, respectively, while the PZCs are -0.2 V and -0.1 V respectively. As a result, both the ion size and specific adsorption effects are more evident in dicationic $[C_6(mim)_2](Tf_2N)_2$ than monocationic $[C_6mim][Tf_2N]$. It is noteworthy that multiple factors may influence the shape of C-V curves aside from ion size and specific adsorption; therefore the C-V curve may be IL-specific depending on the ion chemistry, ion shape, orientation, and affinity towards electrode.[191,194,233]

On average, dicationic $[C_6(mim)_2](Tf_2N)_2$ exhibits higher differential capacitance than monocationic $[C_6mim][Tf_2N]$ (-2.0 V ~ 2.0 V), which is not the fact for BF_4-containing DILs and MILs. The screening factors displayed higher screening factors of $[C_6(mim)_2](Tf_2N)_2$ at both positive and negative potentials than those of $[C_6mim][Tf_2N]$, which could probably explain the observed different trends of capacitance between DILs and MILs with Tf_2N- and BF_4- as anions.

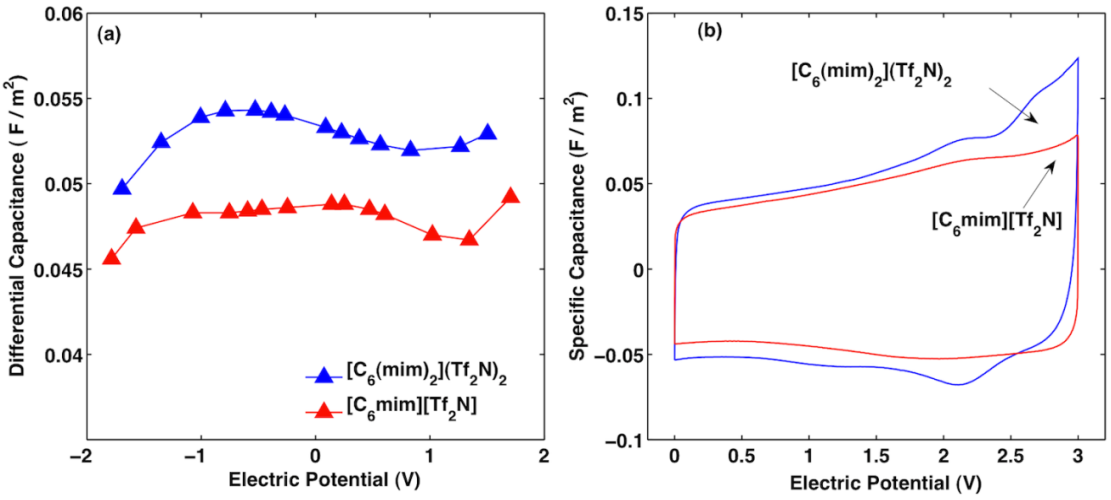

Figure 6.11. Differential capacitance as a function of electric potential obtained from MD simulation (a) and normalized cyclic voltammogram showing specific capacitance as a

function of electric potential at a scan rate of 0.5 mV/s (b), for dicationic $[C_6(mim)_2](Tf_2N)_2$ and monocationic $[C_6mim][Tf_2N]$.

The enhanced capacitance in $[C_6(mim)_2](Tf_2N)_2$ is also verified experimentally by cyclic voltammetry shown in Figure 6.11b. However, this trend is only observed experimentally for cyclic voltammogram curves under a scan rate of 0.5 mV/s (synonymous with charge-discharge rate), since MD simulations were performed at equilibrium state, which is close to the measurement at very low scan rate. At high scan rate (e.g., 50 mV/s), monocationic $[C_6mim][Tf_2N]$ displays a higher capacitance than $[C_6(mim)_2](Tf_2N)_2$. The accumulation of counter-ions in EDLs is a kinetic process: the faster motion of small ions counterbalances the electrode surface charges (the charging/discharging) within shorter times, whereas for larger ions, the slower kinetics do not balance the electrode surface charge, resulting in a lower capacitance.[234] At low scan rates, there is sufficient time for both large and small ions to accumulate in EDLs, *i.e.*, both the electrode surfaces are well balanced by counter-charges, leading to DILs with higher packing density and screening efficiency exhibiting a higher capacitance.

6.4.4 Conclusion

In this study, the interfacial structure and the capacitive performance of DILs $[C_n(mim)_2](BF_4)_2$ with varying chain lengths and $[C_6(mim)_2](Tf_2N)_2$ near the OLC electrodes are investigated for the first time using MD simulations. The distinct interfacial structure of DILs was observed in comparison with their monocationic counterparts. Higher concentrations of DIL anions are found near the OLC surface regardless of the electrode's charge since each dication needs charge balance by two anions. The orientation of the dication near an OLC surface is similar to that of MILs.

Moreover, regarding the capacitive performance of $[C_n(mim)_2](BF_4)_2$, the average capacitance at positively charged potential is higher than that at negatively charged electrode, which is mostly attributed to the larger size of the dications compared to the BF_4 anions. At negatively charged electrodes, the differential capacitance decreases with increasing chain length. It is also found that fewer counter-ions accumulate in EDLs for long-chain DILs based on the cumulative number density profiles. The C-V curve is substantiated to correspond to the variation of charge screening factor as a function of surface charge densities.

A near-flat C-V curve was observed for $[C_6mim][Tf_2N]$ as reported in previous studies,[13,14] and attributed to the constant charge screening factors with the variation of charge screening density. Both ion size and specific adsorption may influence the shape of C-V curves. The increased capacitance in $[C_6(mim)_2](Tf_2N)_2$ compared with $[C_6mim][Tf_2N]$ was observed via both MD and cyclic voltammetry and is due to the more efficient screening of electrode surface charges. Such enhancement was only found at low scan rates because of the different dynamics for small-sized monocations and large-sized dications; slower motion of dications requires a longer time to balance the charges on the electrode surfaces. Since the use of DIL electrolytes in supercapacitors is impeded by their slow kinetic characteristics, in order to facilitate the use of DILs electrolytes in supercapacitors without compromising the power density, organic solvents such as propylene carbonate and acetonitrile were adopted to enhance the conductivity and charge/discharge rate.[92] However, the mechanism of the enhanced performance of DILs-based supercapacitors due to organic solvents is waiting to be investigated, which will be addressed in our future work.

6.5 Capacitive Behavior of Dicationic Ionic Liquids in Organic Solvents

6.5.1 Conductivity of DILs at Varying Concentrations in the Presence of Organic Solvents

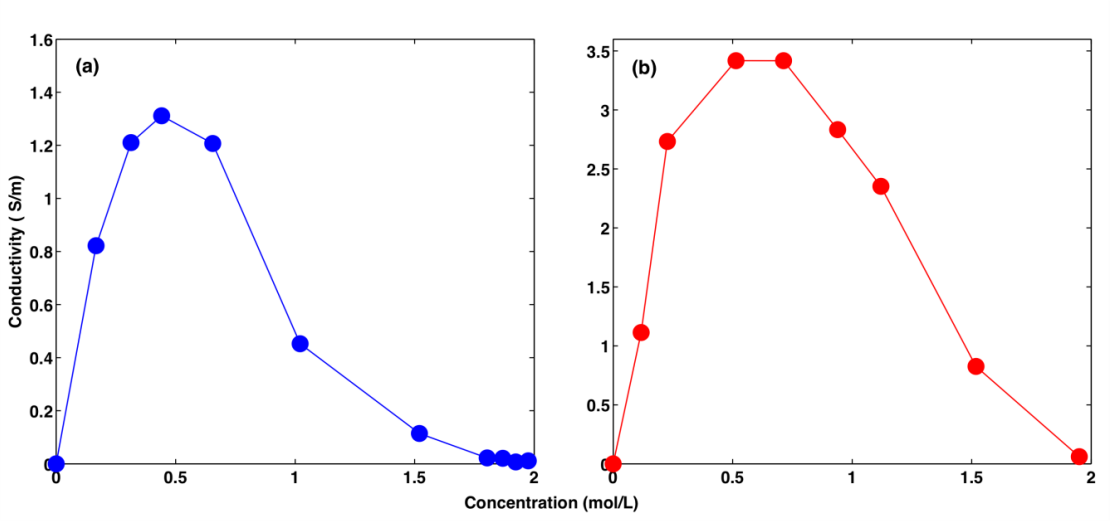

Figure 6.12. Conductivity of $[C_6(mim)_2](Tf_2N)_2$ as a function of molar concentrations in ACN solvents obtained from MD simulations (a) and experimental measurement (b).

The conductivity enhancement of ionic liquids by organic solvent ACN was firstly investigated by both MD simulation and experimental measurement as shown in Figure 6.12. It is obvious that the conductivity of $[C_6(mim)_2](Tf_2N)_2$/ACN solution exhibits a DIL-concentration dependence. With the decrease of the DIL concentration, the conductivity is dramatically increased until a limiting concentration, below which, the conductivity reduction is observed due to the smaller amount of ions present in solution, which was evidenced in both MD (Figure 6.12a) and experimental measurement (Figure 6.12b). The highest conductivity of $[C_6(mim)_2](Tf_2N)_2$/ACN is inspected at the concentration of 0.5 mol/L, which is approximately 50 times higher than that of neat $[C_6(mim)_2](Tf_2N)_2$. The conductivity enhancement for monocationic ionic liquids (MILs)/ACN has been reported in another MD simulation,[210] in which similar trend was

observed. Our previous study has demonstrated that the outperformance of DILs in contrast to MILs electrolyte in supercapacitors can only be observed at low scan rates, [188] which suggests the determining role of dynamic properties of electrolytes. Consequently, the increased diffusion of DILs in ACN indicates the better capacitive performance of DILs electrolytes at high scan rates, thus leading to enhanced power density.

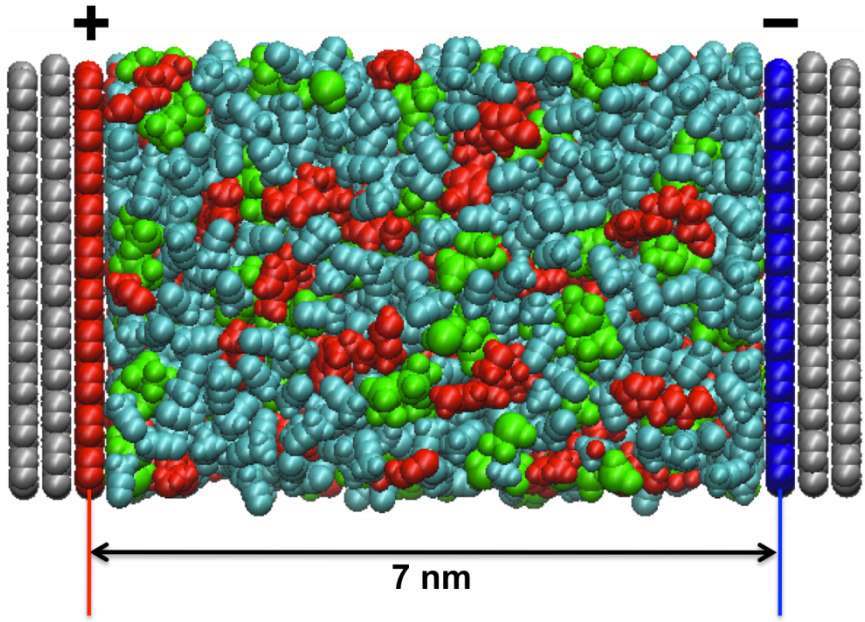

Figure 6.13. Simulation setup for a supercapacitor cell consisting of two opposite there-layer graphites with uniformly distributed positive and negative charges on the innermost layers. The red, green and cyan spheres represent cations, anions and organic solvent molecules between two electrodes, respectively.

6.5.2 Electric Double Layer Structure in the Presence of Organic Solvents

To investigate the capacitive performance of neat DILs, DILs/ACN and DILs/PC electrolytes (5% DILs in molar ratio), respectively, the three electrolytes were employed in graphite-based supercapacitors. The simulation model for supercapacitors was shown in Figure 6.13. The distance between two electrodes is 7 nm, which is sufficiently distant

for electrolytes in the middle to exhibit bulk-like behavior. Once the innermost layers were uniformly charged with opposite charges, an electric potential was applied along the normal direction of graphites, resulting in a densely packed adsorbed layer consisting mostly of counter-ions and a small amount of co-ions. Such an adsorbed layer is also named electric double layer (EDL), which is the key determining the energy storage density in supercapacitors. The effects of organic solvents on the structures of EDLs formed by three electrolytes near neutral and charged electrode surfaces were analyzed and shown in Figure 6.14.

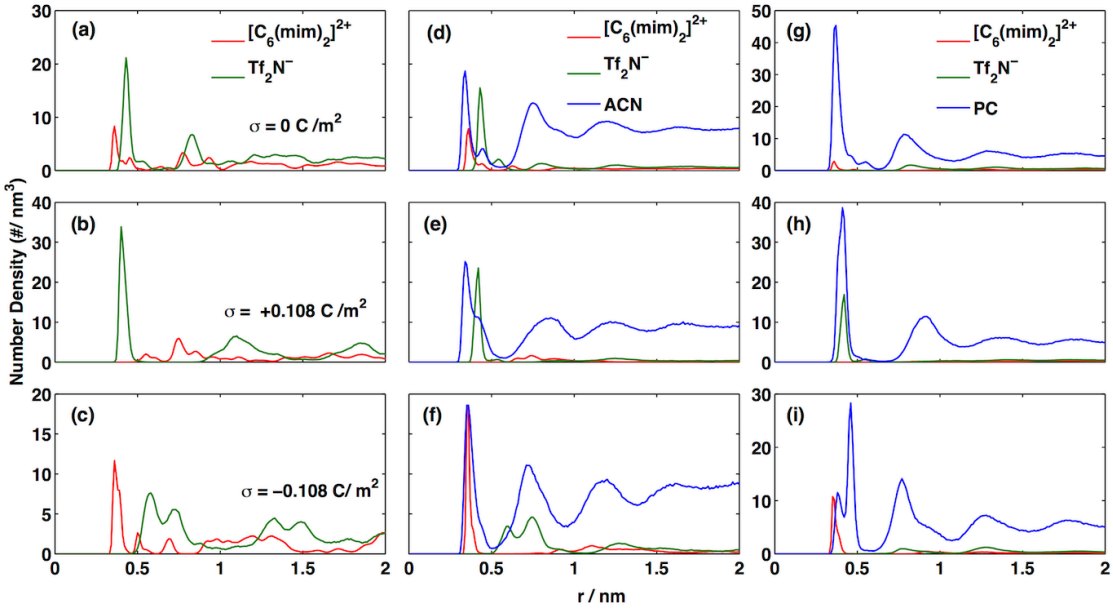

Figure 6.14. Number density profile for cations, anions, ACN and PC molecules at uncharged and charged graphite electrodes. Left panels (a, b, c) are the number density profiles for neat DIL $[C_6(mim)_2](Tf_2N)_2$. Middle panels (d, e, f) and right panels (g, h, i) are the number density profiles for $[C_6(mim)_2](Tf_2N)_2$/ACN and $[C_6(mim)_2](Tf_2N)_2$/PC at the molar ratio of 5%.

Comparing the ion density of neat $[C_6(mim)_2](Tf_2N)_2$ with that of $[C_6(mim)_2](Tf_2N)_2$/ACN and $[C_6(mim)_2](Tf_2N)_2$/PC at uncharged/charged electrodes, the layering of ions in neat DIL is more pronounced and more ions of neat DILs are accumulated near electrodes than those of DILs/ACN or DILs/PC. At charged electrode, fewer counter-ions are present in the EDLs of DILs/ACN and DILs/PC in contrast to those of neat DILs, indicating the decreased charge compensation. It was found that the presence of ACN or PC caused the strong expulsion of co-ions from EDLs. Similar phenomenon was reported in an MD study of MILs/ACN electrolytes-based supercapacitors.[213] The expulsion of co-ions is probably because of the weakened cation-anion coupling and/or reduced electrode-ion interaction in ILs/ACN due to the presence of polar solvents compared with that in neat IL, leading to the lower energy barrier for co-ions to move away from electrode surface. The decreased free energy between electrode and ions in IL/ACN has been verified in Merlet *et al.*'s study.[213] The calculated coordination number at interface, *i.e.*, the coordination number of anions surrounding cations located within the first adsorbed layer(r= 0.0 -0.6 nm), is 4.75 for neat DILs and 2.19 for DILs/ACN, suggesting that ACN molecules facilitate the dissociation of ion pairs, similar to previous investigation.[213] Therefore, ACN does not only weaken the electrode-ion interaction but also enhance the dissociation of cation-anion pairs in the adsorbed layer near electrode surface.

On the other hand, when comparing the influences of ACN and PC on the EDL structures, it is found that there are a large amount of PC molecules adsorbed on the graphite in contrast to ACN. The expulsion of co-ions from EDLs becomes more evident in PC-containing electrolytes. The calculated coordination number of anions surrounding

cations in the EDL formed by $[C_6(mim)_2](Tf_2N)_2$/PC is close to 1.20 in contrast to 2.17 for $[C_6(mim)_2](Tf_2N)_2$/ACN. Such a big discrepancy is attributed to the dissimilar interaction potentials of ACN/graphite and PC/graphite. The interaction potential energy, shown in Figure 6.15, suggests that there is stronger attraction between PC molecules and graphites compared with ACN/graphite, which leads to a significant accumulation of PC at graphite. It is also observed that for DIL/PC electrolytes, cations are more preferably adsorbed on graphite rather than anions; for DIL/ACN electrolytes, the difference between the interactions of cation-graphite and anion-graphite is less evident, which coincides with their number density profiles shown in Figure 6.14d and 6.14g.

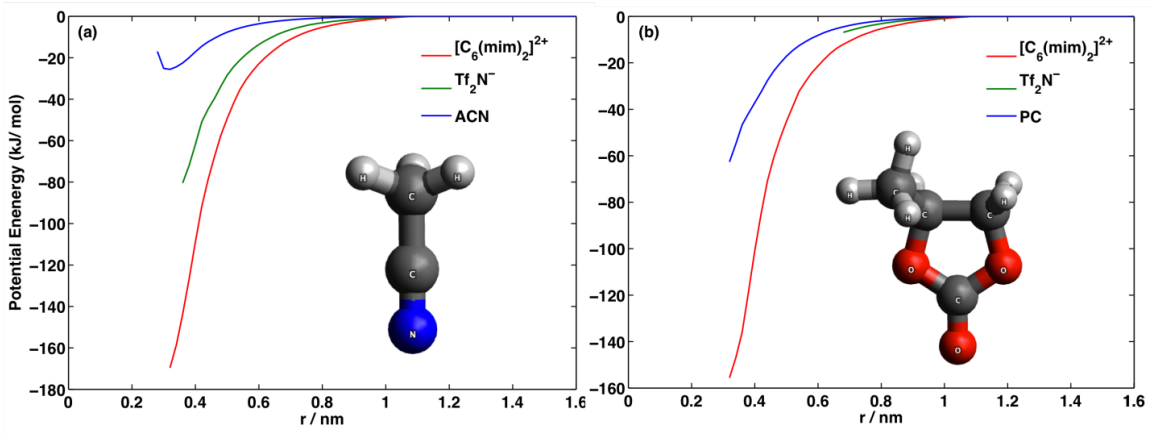

Figure 6.15. Comparison of averaged interaction potential energy per molecule as a function of distance toward electrode for (a) $[C_6(mim)_2](Tf_2N)_2$/ACN and (b) $[C_6(mim)_2](Tf_2N)_2$/PC between ions/organic solvents and neutral graphite electrode. Light and dark gray spheres represent hydrogen and carbon, respectively. Blue spheres represent nitrogen, and red spheres represent oxygen atoms

Moreover, to disclose more details of the interfacial structure of EDLs, the orientational order parameter of ACN and PC near charged/uncharged graphite surfaces

was calculated using $\langle P_2 \rangle = \frac{1}{2}(3\cos^2\theta - 1)$ as shown in Figure 6.16. The orientational order parameter describes the distribution of angles formed by the surface normal of graphite and the vector pointing from C atom of methyl group to N atom in ACN and those formed by the surface normal of graphite with the plane determined by two O atoms and one C atom in-between of five-member ring in PC. The results show that ACN in the first adsorbed layer is preferable to parallelize with graphite surface, which is not obviously influenced by the presence of surface charges. However, the orientation of PC molecules at graphite surface is more sensitive to the surface charge. They tend to tilt at an angle of 50° and 35° with graphite surfaces at neutral and negatively charged graphite, respectively, and as the electrode is positively charged, PC becomes vertically oriented to the graphite surface. This indicates an evident reordering of PC molecules at graphite with the variation of surface charges due to the complicated structure and big size of PC compared with linear smaller-sized ACN.

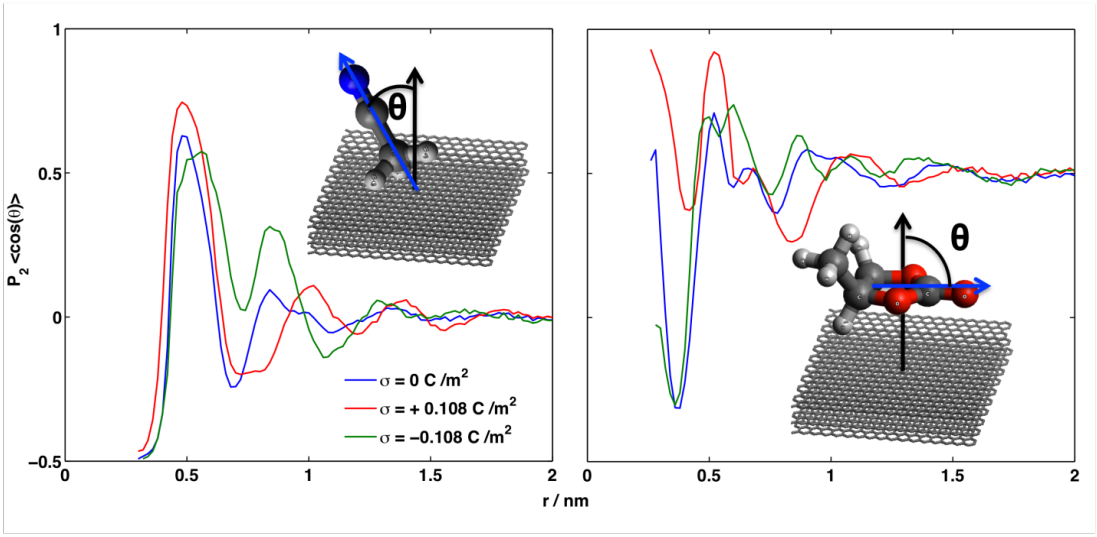

Figure 6.16. Orientational order parameter of angles formed by the surface normal of graphite with the vector shown in ACN (a) and the plane of PC (b) as a function of distance to graphite surfaces.

The orientations of dications in DILs/ACN, DILs/PC and neat DILs were compared as well (Figure 6.17). The imidazolium ring of dications in neat DIL in the first adsorbed layer tend to parallelize to the neutral electrode surface, whereas the dications in its neighboring region are opt to be perpendicular to electrode surfaces. Such well-ordered organization of dications in the adsorbed layers was not influenced by the presence of ACN or PC, which can be probably attributed to the stronger interaction between electrodes and dications in comparison with anions and ACN or PC (Figure 6.15). At the negatively charged electrode, the dominant columbic interaction between electrodes and counter-ions re-orientates the dications in order to efficiently overcompensate the surface charges on electrode, which is almost not affected by the presence of ACN or PC.

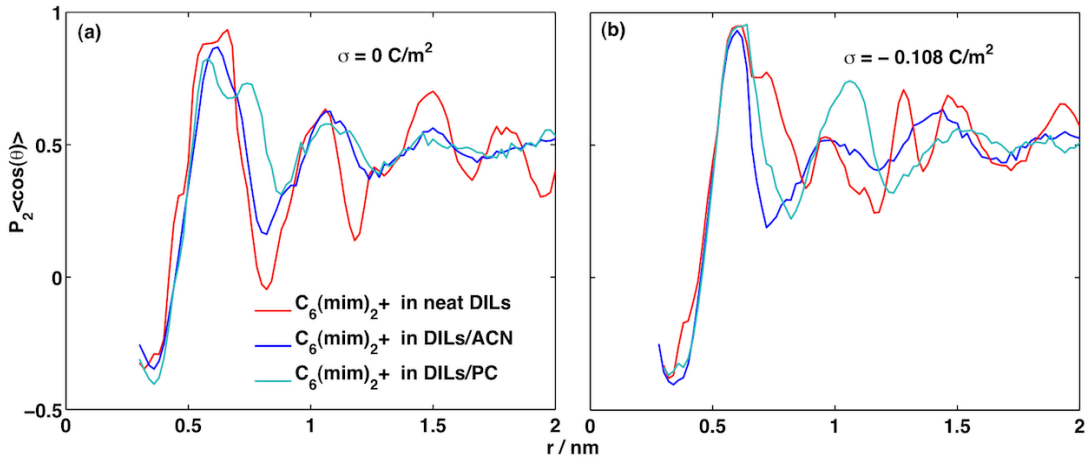

Figure 6.17. Orientational order parameter for the angle formed by the imidazolium plane of dictaions and the surface normal of graphite electrodes.

6.5.3 Influence of Organic Solvents on Capacitance

Then, how will organic solvents influence the differential capacitance-electric potential (C-V) curve? Merlet *et al.*'s coarse-grained MD simulation has revealed that organic solvent ACN attenuated the dissymmetry of C-V curves obtained from neat MILs-based supercapacitors.[213] In this study, such trend is not observed, probably due to the different ions and ion models (all-atom model vs. coarse-grained model) used, since BF_4-containing ILs used in their study is usually accompanied with an asymmetric C-V curve. For dicationic $[C_6(mim)_2](Tf_2N)_2$ adopted herein, a typical bell-shaped C-V curve is exhibited (Figure 6.18), similar to reported results for MILs.[187] Although the bell-shaped C-V curve is not altered by the presence of organic solvent ACN, the belled curve is flattened, which means the decreasing of differential capacitance with the increase of electric potential is slowed down. And the overall differential capacitance throughout the potential range is increased by 15% in contrast to neat $[C_6(mim)_2](Tf_2N)_2$ (0.039 F /m^2 for neat DIL and 0.045 F /m^2 for DIL/ACN), in agreement with previous report for MILs/ACN.[213]

Although PC exhibits stronger adsorption on graphite and more obvious expulsion of co-ions from the EDL, DIL/PC displays almost the same shape of C-V curve with DIL/ACN except a slight rise at negative potentials and a subtle decrease at positive potentials. The overall differential capacitance throughout the potential range is very similar to that of DIL/ACN (0.044 F /m^2 for DIL/PC versus 0.045 F /m^2 for DIL/ACN). Further explanation is provided later.

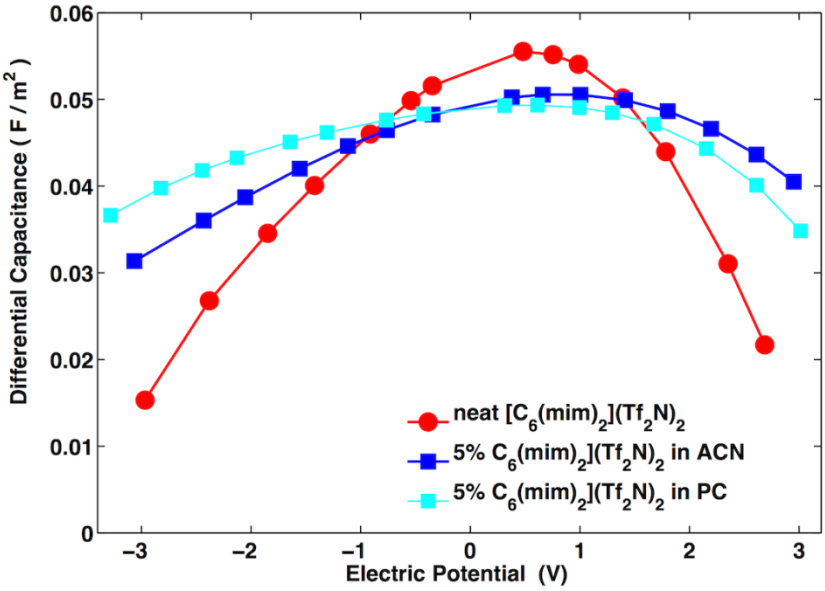

Figure 6.18. (a) Differential capacitance as a function of electric potential applied for neat dicationic $[C_6(mim)_2](Tf_2N)_2$, $[C_6(mim)_2](Tf_2N)_2$/ACN and $[C_6(mim)_2](Tf_2N)_2$/PC electrolytes at the IL ratio of 5%.

The cumulative number density per unit surface area of electrode (Figure 6.19a) also provides the molecular insight into the enhanced capacitance by the presence of ACN. More concentrated ions in EDLs of neat DIL than those of DIL/ACN are observed at both positive and negative potentials. The expulsion of co-ions from EDLs of DIL/ACN is clearly demonstrated in Figure 6.19a, in which the number of co-ions in EDL is decreased more rapidly than those of neat DIL with the increase of potential. The depletion of co-ions with increasing potentials is inspected for both neat DIL and DIL/ACN, however the depletion is achieved at a lower potential than that for neat DIL, indicating the favorable co-ion expulsion in the presence of ACN. Figure 6.19b shows the cumulative number density normalized by the density at potential of zero charge (PZC) or neutral electrode, n_σ / n_{pzc}, as a function of potential reveals the different change rates

of cumulative number densities for counter-ions and co-ions with the variation of electric potential.

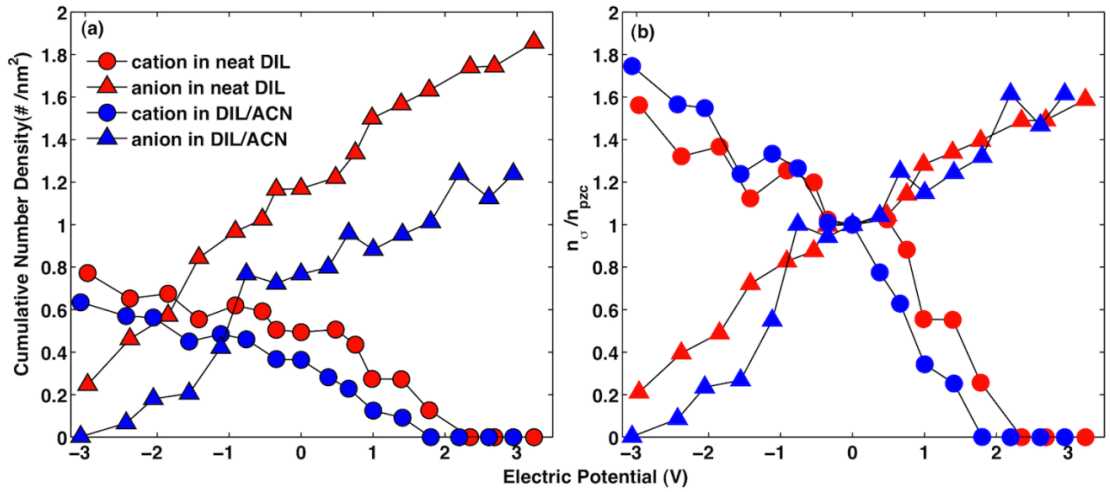

Figure 6.19. (a) Cumulative number density of cations and anions in electric double layer (EDL) as a function of electric potential applied for neat dicationic $[C_6(mim)_2](Tf_2N)_2$ and $[C_6(mim)_2](Tf_2N)_2$ /ACN solution at the IL ratio of 5%; (b) the ratio of ion number in EDLs near charged electrodes to that at PZC or neutral electrode.

At positive potentials, the n_σ / n_{pzc} of counter-ions (anions) increases with increasing potentials in order to compensate the surface charges of electrode; the n_σ / n_{pzc} of co-ions (cations) in DIL/ACN is decreased from 1 at PZC to 0 at ~1.8 V, whereas that in neat DIL starts to decrease from 1 at approximately 0.5 V to 0 at 2.4 V. At negative potentials, counter-ions (cations) exhibit higher increase rate for DIL/ACN in contrast to neat DIL; the number of co-ions (anions) in DIL/ACN is reduced more quickly from -0.8 V than that of neat DILs and the depletion of co-ions is only observed in DIL/ACN at -3.0 V. In both positive and negative potentials, the quantity of co-ions in EDL is smaller than that of neat DIL. And the number of co-ions decreases faster with the increasing potential in DIL/ACN due to the facilitated dissociation of ion pairs in the presence of ACN,

indicating that the slightly increased capacitance in DIL/ACN –based supercapacitors is most probably ascribed to the strong expulsion of co-ions from EDLs.

Another interesting observation is that cations as co-ions are depleted at lower absolute values of potentials than anions for both neat DILs (+2.4 V for cations versus < -3 V for anions) and DIL/ACN (+1.8 V for cations versus -3.0 V for anions). This is probably attributed to the concentrated charge density and bulky size of dications, which associate with two anions. With the increasing electric potentials, the repulsion between positively charged electrode and dications becomes stronger than that between negatively charged electrode and anions, because the charges in dications are twice of that in anions. Moreover, dications with the size nearly twice of anions (258 $Å^3$ in volume size for dicationic $[C_6(mim)_2]^{2+}$ and 148 $Å^3$ for Tf_2N^-) occupy more space in EDLs. In order for effectively screening the positive charges on electrodes, more and more anions were accumulated in EDLs, leading to overscreening or overcompensation of counter-charges on electrodes. Eventually, the number of anions in EDLs of positively charged electrode is more than twice of dications in the EDLs of negatively charged electrodes at the same absolute values of potentials (e. g., the number of anions in EDLs is 1.75 at +2.4 V and the number of cations is 0.65 at -2.4 V), which requires more space for anions at positively charged electrode. Therefore, dications as co-ions are favorable to be expelled from EDLs at positive potentials compared with anions at negative potentials, which may be a feature of DILs.

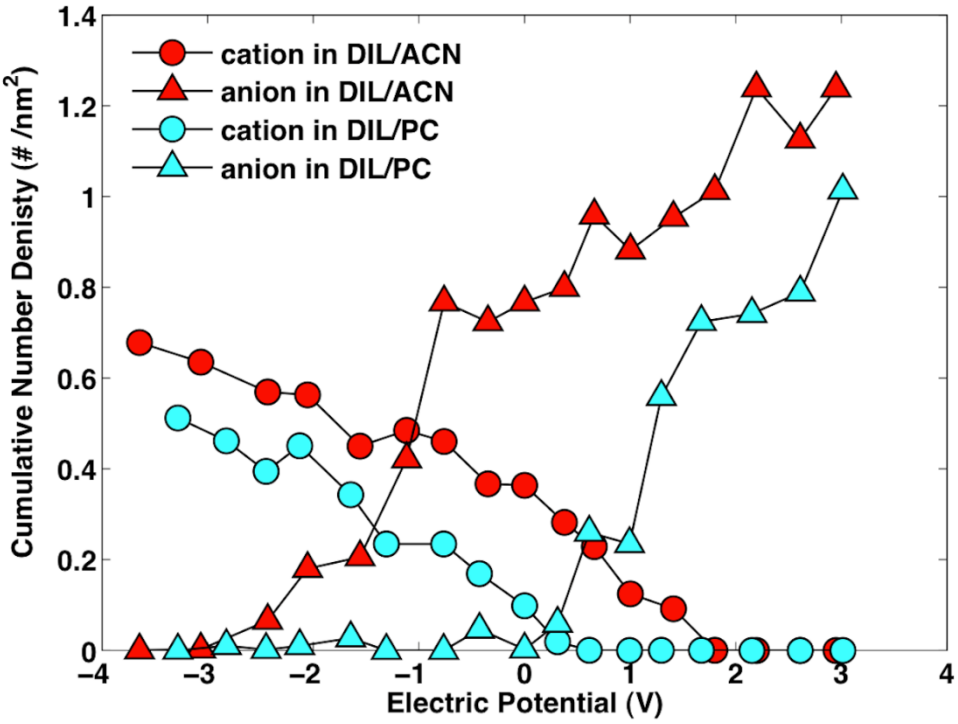

Figure 6.20. Comparison of the cumulative number density of cations and anions in the EDL as a function of electric potential applied for $[C_6(mim)_2](Tf_2N)_2$/ACN and $[C_6(mim)_2](Tf_2N)_2$/PC solution at the IL ratio of 5%.

Comparison of the cumulative number densities of cations and anions in EDLs formed by $[C_6(mim)_2](Tf_2N)_2$/ACN and $[C_6(mim)_2](Tf_2N)_2$/PC is shown in Figure 6.19. The interesting observation is that co-ions depletion occurs at the very low potentials for $[C_6(mim)_2](Tf_2N)_2$/PC, indicating the outstanding co-ion expulsion capability of PC. It is probably due to that the strong adsorption of PC molecules on graphite, which occupy a large fraction of space in EDLs, weakens the association of cation-anion pairs and facilitates the exclusion of co-ion from EDLs. Although the stronger co-ion expulsion is observed in $[C_6(mim)_2](Tf_2N)_2$/PC electrolytes, the differential capacitance is not obviously increased compared with $[C_6(mim)_2](Tf_2N)_2$/ACN electrolytes. This is possibly attributed to the fewer counter-ions accumulated in EDLs formed by

$[C_6(mim)_2](Tf_2N)_2$/PC, therefore the net charges in EDLs of $[C_6(mim)_2](Tf_2N)_2$/ACN and $[C_6(mim)_2](Tf_2N)_2$/PC are similar to each other with respect to a response of potential change, leading to comparable differential capacitance.

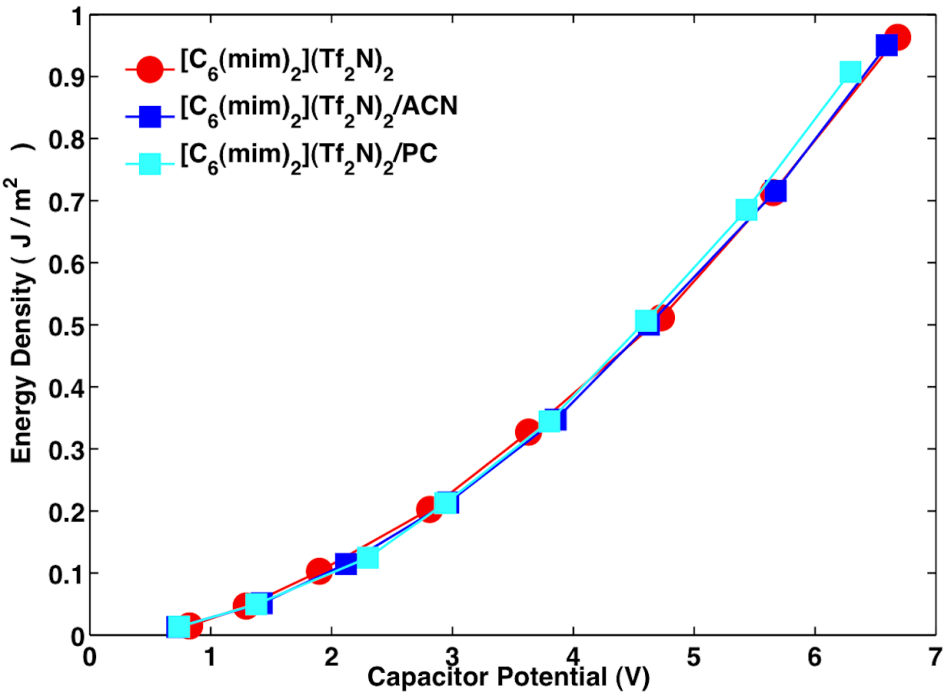

Figure 6.21. The energy density of capacitors as a function of potential difference between two electrodes for neat $[C_6(mim)_2](Tf_2N)_2$, $[C_6(mim)_2](Tf_2N)_2$/ACN and $[C_6(mim)_2](Tf_2N)_2$/PC electrolytes.

Although the conductivity of $[C_6(mim)_2](Tf_2N)_2$/ACN electrolytes are greatly enhanced, suggesting the improved power density, the concern that whether the presence of ACN will compromise the energy density of supercapacitors is still haunting. We calculated the energy densities (Figure 6.21) as a function of absolute potential drop between cathode and anode for supercapacitors with neat $[C_6(mim)_2](Tf_2N)_2$, $[C_6(mim)_2](Tf_2N)_2$/ACN and $[C_6(mim)_2](Tf_2N)_2$/PC as the electrolyte, respectively. The result demonstrates that the presence of organic solvent ACN or PC in electrolytes does

not reduce the stored energy density of supercapacitors compared with the neat ionic liquids electrolytes without organic solvents. Thus, adding organic solvents into dicationic ionic liquids electrolytes of supercapacitors provides enhanced conductivity and charge/discharge rate without losing energy density stored.

6.5.4 Conclusion

In summary, this work investigates the influence of organic solvents ACN and PC on the conductivity of dicationic ionic liquid electrolyte $[C_6(mim)_2](Tf_2N)_2$, their EDL structure and C-V curve of $[C_6(mim)_2](Tf_2N)_2$ -based supercapacitors using MD simulations. The greatly enhanced conductivity by ACN addition is observed in both MD and experimental measurement. There are more cations and anions in the EDLs of neat $[C_6(mim)_2](Tf_2N)_2$ than in those of $[C_6(mim)_2](Tf_2N)_2$/organic solvents. The presence of organic solvents is also found to facilitate the dissociation of cation-anion pairs in EDLs, leading to the expulsion of co-ions from EDLs at charged electrodes. PC exhibits outstanding co-ion expulsion capability due to its stronger adsorption on graphite in contrast to ACN. Furthermore, the bell-shaped C-V curve inspected in neat DIL-based supercapacitor becomes flattened in DIL/ACN-based one and the capacitance is slightly increased due to the presence of ACN. Similar C-V curve was observed for DIL/PC. The cumulative number density in EDLs is used to explain the discrepancy of C-V curves of DIL- and DIL/ACN-based supercapacitors. The energy density stored in supercapacitor changes little with the presence of ACN or PC in dicationic ionic liquid electrolyte.

Besides all of the aforementioned advantages of suing organic solvents as additives to DILs, the former can potentially reduce the cost of the DIL-based supercapacitors, which is crucial for commercial applications. For instance, ionic liquids are relatively

inexpensive to prepare in small laboratory scale. However, the costs associated to their large-scale preparation, and in high purity, could make these cost prohibitive for commercialization. By using organic solvents such as ACN, which is already used in commercial supercapacitors, the increase in power and energy density granted by the DIL/ACN electrolytes can be achieved at a reasonable cost.

CHAPTER VII

CONLUSION AND FUTURE WORK

7.1 Conclusion

Molecular dynamics (MD) simulation has been used to provide the new molecular insight into the structural organization, dynamics and capacitive performance of RTILs in this dissertation. These findings help lay the foundation for understanding the behaviors of RTILs in either bulk or confinements, especially for novel type of ionic liquids, such as pyrrolidinium-based RTILs and DILs, which may inspire research interests in this field and facilitate the rational design and application of RTIL electrolytes in energy storage devices. The methodology used in this dissertation will aid further investigation on different types of RTILs and their performance in supercapacitors.

Specifically, Chapter IV concentrates on spatial heterogeneity in RTILs using MD simulation. Similar to experimentally obtained results, the calculated structure factors present a featured prepeak at low Q region with the prolongation of alkyl chain in cations, which is related to the enhanced segregation of polar and nonpolar groups in RTILs. The presence of prepeak in structure factor is essentially contributed by the enhanced anion-anion correlation, which has been evidenced in many theoretical studies. The variation of temperature causes the rearrangement of polar cation head/anion and nonpolar alkyl tails in RTILs, which gives rise to the shift of prepeak in structure factors. Our first study on comparison of the spatial heterogeneity in DILs and MILs reveals a less heterogeneous distribution of ions in DILs in contrast to MILs, which is further evidenced by low heterogeneity order parameter (HOP) value in DILs and high HOP in MILs. The micelle-

like model for MILs and straight-chain model for DILs provide a theoretical understanding towards the dissimilar structure organization in DILs and MILs.

The confinement effects on RTILs in silica and carbon mesopores are presented in Chapter V. It is known that the properties of confined RTILs are changed in confined space in comparison with those in bulk. The influence of solid mesoporous materials on the interfacial structure and dynamic properties of RTILs is studied. The weak temperature dependence of translational diffusion in the adsorbed layer at silica mesopore is for the first time reported in contrast to the evident temperature dependent diffusion of RTILs in carbon mesopores. Importantly, ions of RTILs are more closely adsorbed in silica walls due to the silica surface roughness and stronger interaction between ion-silica walls, which may be the cause for the weak temperature dependence of RTILs in silica mesopore. In addition, the number density profile and interaction potential profile for silica confined RTILs exhibit more oscillations, which matches AFM measured force profile as well.

The role of RTILs as electrolytes in sueprcapacitors is addressed in Chapter VI, including the binary mixture of RTILs electrolytes and dicatinioc ionic liquids (DILs) electrolytes. An equimolar mixture of 1-methyl-1-propylpyrrolidinium bis(trifluoromethylsulfonyl)-imide ($[C_3mpy][Tf_2N]$), 1-methyl-1-butylpiperidinium bis(trifluoromethylsulfonyl)imide ($[C_4mpip][Tf_2N]$) was investigated by classic MD simulation. Differential scanning calorimetry (DSC) measurements verified that the binary mixture exhibited lower glass transition temperature than either of the pure RTILs. Moreover, the binary mixture gave rise to higher conductivity than the neat RTILs at lower temperature range. In order to study its capacitive performance in supercapacitors,

simulations were performed of the mixture and the neat RTILs used as electrolytes near an onion-like carbon (OLC) electrode at varying temperatures. The differential capacitance exhibited independence of the electrical potential applied for three electrolytes, which is in agreement with previous work on OLC electrode in a different RTIL. Positive temperature dependence of the differential capacitance was observed and it was dominated by the electrical double layer (EDL) thickness, which is for the first time substantiated in MD simulation. Such finding provides the theoretical understanding in positive temperature dependence observed in may experiments.

EDL structure formed by ions at a charged surface, which is the key to determining the performance of supercapacitors, has been extensively studied for monocationic ionic liquids (MILs). However, it is not known what effect replacing MILs with dicationic ionic liquids (DILs) will have on the EDL structure. The first MD study on DIL electrolyte in OLC-based supercapacitors are performed and the details are provided in Section 6.4. The interfacial structure and electrochemical performance of DILs $[C_n(mim)_2](BF_4)_2$ (n=3, 6, 9) and $[C_6(mim)_2](Tf_2N)_2$ were investigated using classical molecular dynamics (MD) simulation for comparison with their monocationic counterparts. Different EDL structures formed by DILs and MILs near an onion-like carbon (OLC) electrode were observed. The interfacial orientation of the imidazolium plane in dications was verified to be similar to that of monocations. Moreover, the dissimilar sizes of the cation/anion and the specific ion adsorption on OLC were found to contribute to the distinctive shape of the differential capacitance-electric potential (C-V) curves, which were also dependent on the type of anions. Increased capacitance in BF_4-containing DILs was not observed in comparison with their counterpart MILs, whereas

dicationic $[C_6(mim)_2](Tf_2N)_2$ yielded higher differential capacitance in contrast to monocationic $[C_6mim][Tf_2N]$, which was substantiated by cyclic voltammetry measurements as well. This work provides molecular insights into the EDL structure and C-V curves of imidazolium-based DILs in OLC-based supercapacitors.

The use of DILs electrolytes in supercapacitors is impeded by the slow dynamics of DILs, whereas, the addition of organic solvents into DIL electrolytes improves ion transport and then enhances the power density of supercapacitors. In Section 6.5, the influences of organic solvents on the conductivity of DILs and their EDLs of DILs-based supercapacitors are investigated using classical molecular dynamics simulation (MD). Two types of organic solvents: acetonitrile (ACN) and propylene carbonate (PC) were used to explore the effects of different organic solvents on the EDL structure and capacitance of DIL/organic solvents-based supercapacitors. Firstly, it was found that the conductivity of DILs electrolyte was greatly enhanced in the presence of organic solvent ACN. Secondly, stronger adsorption of PC on graphite results in different EDL structures formed by DIL/ACN and DIL/PC electrolytes. The expulsion of co-ions from EDLs was observed in DIL/organic solvent electrolytes rather than neat DILs and such feature is more evident in DIL/PC. Furthermore, the bell-shaped differential capacitance-electric potential (C-V) curve was not essentially changed by the presence of organic solvents. Comparing DIL/organic solvent electrolytes with neat DILs, the capacitance is slightly increased by organic solvents, which is in agreement with experimental observation.

7.2 Recommendation for Future Work

7.2.1 Spatial Heterogeneity of RTILs in Confinement

The spatial heterogeneity of RTILs in bulk has been extensively studied using both experimental and theoretical methods.[9,11,48] Chapter IV presents the structural segregation of bulk RTILs by MD simulation in comparison with experimental results from SAXS. However, the spatial heterogeneity for RTILs in confined space has been rarely reported. With the development of porous carbon electrode materials, such as carbide derived carbon,[235] mesoporous carbon[236] and carbon nanotubes, it is of great importance to understand the organization of RTILs at molecular level in these porous materials, which will influence the observed experimental phenomena, such as the structure factor from SAXS[7] and dynamic heterogeneity measured from neutron spin echo technique.[237] How does the alkyl chain length affect the structural organization of RTILs in confinement? How does the spatial heterogeneity of RTILs change at solid-liquid interfaces? What structure factor do the confined RTILs present and how is it compared with the experimental results? MD simulation may be useful to answer these questions with more realistic model to gain insight into the nanoscale structure and dynamics properties in confinement.

7.2.2 Capacitive Performance of RTILs Electrolytes with Realistic Carbon Electrode Model

Currently investigated carbon electrode models are all in regular geometry with uniform surface properties, such as planar graphite,[134] spherical onion-like carbon[13,14] and cylindrical carbon nanotube.[238] In Chapter V, the mesoporous carbon/silica is modeled using cylindrical nanotubes. Chapter VI presents the study on the RTILs-based supercapacitors using onion-like carbon and planar graphite as electrodes. In practice,

electrode materials consist of multiple-scale and irregular-shaped meso/nanopores with high surface area,[4] which will enhance the energy density stored in supercapacitors. And most realistic electrodes have various defects or functionalized groups, which complicates the simulation of supercapacitors with realistic models. To accurately predict the performance of RTILs in supercapacitors, the realistic electrode models are required. In addition, all the electrodes in current simulations are rigid. In order to introduce the flexibility of electrode model, more computational time is also needed. However, there are still lots of challenges for modeling realistic electrode. For instance, the reactivity of defected or functionalized electrodes with RTILs may have to be taken into account, which requires reactive force field.

7.2.3 Charging/discharging Dynamics of RTILs

Another possible goal to pursue is the charging/discharging dynamics of RTILs. Most studies on RTILs-based supercapacitors focused on energy density. Power density is another important parameter evaluating the performance of supercapacitors, which determines how fast the supercapacitor will be charged/discharged.[239,240] Although charging/discharge process has been widely investigated in a series of experiments such as cyclic voltammetry,[241] it has not been extensively studied computationally in molecular level. How will different RTILs electrolytes and electrode materials influence charging/discharge dynamics? And in this process, how the structure and orientation of RTILs changes, especially the electric double layer structure. MD simulation is the suitable tool to reveal the mechanism of ion mobility in the confined geometry during charging/discharging in molecular level in contrast to numerical calculation. The obtained molecular level insight will be used to optimize the design and selection of

electrolyte/electrode combinations to achieve enhanced not only energy density but also power density in EDLCs.

REFERENCES

(1) Johnson, K. E. What's an Ionic Liquid? *Electrochem. Soc. Interface* **2007**, *16*, 38-41.

(2) Castner, E. W.; Wishart, J. F. Spotlight on Ionic Liquids. *J. Chem. Phys.* **2010**, *132*, 120901.

(3) Weingaertner, H. Understanding Ionic Liquids at the Molecular Level: Facts, Problems, and Controversies. *Angew Chem. Int. Ed.* **2008**, *47*, 654-670.

(4) Zhang, L. L.; Zhao, X. S. Carbon-Based Materials as Supercapacitor Electrodes. *Chem. Soc. Rev.* **2009**, *38*, 2520-2531.

(5) Davis, J. H. Task-Specific Ionic Liquids. *Chem. Lett.* **2004**, *33*, 1072-1077.

(6) Wang, Y.; Voth, G. A. Unique Spatial Heterogeneity in Ionic Liquids. *J. Am. Chem. Soc.* **2005**, *127*, 12192-12193.

(7) Bradley, A. E.; Hardacre, C.; Holbrey, J. D.; Johnston, S.; McMath, S. E. J.; Nieuwenhuyzen, M. Small-Angle X-Ray Scattering Studies of Liquid Crystalline 1-Alkyl-3-Methylimidazolium Salts. *Chem. Mater.* **2002**, *14*, 629-635.

(8) Hardacre, C.; Holbrey, J. D.; Mullan, C. L.; Youngs, T. G.; Bowron, D. T. Small Angle Neutron Scattering from 1-Alkyl-3-Methylimidazolium Hexafluorophosphate Ionic Liquids ($[C_nMim][PF_6]$, N=4, 6, and 8). *J. Chem. Phys.* **2010**, *133*, 074510.

(9) Santos, C. S.; Murthy, N. S.; Baker, G. A.; Castner, E. W., Jr. Communication: X-Ray Scattering from Ionic Liquids with Pyrrolidinium Cations. *J. Chem. Phys.* **2011**, *134*, 121101.

(10) Perkin, S. Ionic Liquids in Confined Geometries. *Phys. Chem. Chem. Phys.* **2012**, *14*, 5052-5062.

(11) Li, S.; Banuelos, J. L.; Guo, J.; Anovitz, L.; Rother, G.; Shaw, R. W.; Hillesheim, P. C.; Dai, S.; Baker, G. A.; Cummings, P. T. Alkyl Chain Length and Temperature Effects on Structural Properties of Pyrrolidinium-Based Ionic Liquids: A Combined Atomistic Simulation and Small-Angle X-Ray Scattering Study. *J. Phys. Chem. Lett.* **2012**, *3*, 125-130.

(12) Li, S.; Han, K. S.; Feng, G.; Hagaman, E. W.; Vlcek, L.; Cummings, P. T. Dynamic and Structural Properties of Room-Temperature Ionic Liquids near Silica and Carbon Surfaces. *Langmuir* **2013**, *29*, 9744-9749.

(13) Feng, G.; Jiang, D. E.; Cummings, P. T. Curvature Effect on the Capacitance of Electric Double Layers at Ionic Liquid/Onion-Like Carbon Interfaces. *J. Chem. Theory Comput.* **2012**, *8*, 1058-1063.

(14) Li, S.; Feng, G.; Fulvio, P. F.; Hillesheim, P. C.; Liao, C.; Dai, S.; Cummings, P. T. Molecular Dynamics Simulation Study of the Capacitive Performance of a Binary Mixture of Ionic Liquids near an Onion-Like Carbon Electrode. *J. Phys. Chem. Lett.* **2012**, *3*, 2465-2469.

(15) Li, S.; Feng, G.; Banuelos, J. L.; Rother, G.; Fulvio, P. F.; Dai, S.; Cummings, P. T. Distinctive Nanoscale Organization of Dicationic Versus Monocationic Ionic Liquids. *J. Phys. Chem. C* **2013**, *117*, 18251-18257.

(16) Lin, R. Y.; Taberna, P. L.; Fantini, S.; Presser, V.; Perez, C. R.; Malbosc, F.; Rupesinghe, N. L.; Teo, K. B. K.; Gogotsi, Y.; Simon, P. Capacitive Energy Storage from -50 to 100 Degrees C Using an Ionic Liquid Electrolyte. *J. Phys. Chem. Lett.* **2011**, *2*, 2396-2401.

(17) Lockett, V.; Sedev, R.; Ralston, J.; Horne, M.; Rodopoulos, T. Differential Capacitance of the Electrical Double Layer in Imidazolium-Based Ionic Liquids: Influence of Potential, Cation Size, and Temperature. *J. Phys. Chem. C* **2008**, *112*, 7486-7495.

(18) Costa, R.; Pereira, C. M.; Silva, F. Double Layer in Room Temperature Ionic Liquids: Influence of Temperature and Ionic Size on the Differential Capacitance and Electrocapillary Curves. *Phys. Chem. Chem. Phys.* **2010**, *12*, 11125-11132.

(19) Li, S.; Van Aken, K. L.; McDonough, J. K.; Feng, G.; Gogotsi, Y.; Cummings, P. T. The Electrical Double Layer of Dicationic Ionic Liquids at Onion-Like Carbon Surface (in revision). *J. Phys. Chem. C* **2013**.

(20) Li, S.; Zhang, P.; Fulvio, P.; Hillesheim, P.; Feng, G.; Dai, S.; Cummings, P. Enhanced Performance of Dicationic Ionic Liquid Electrolytes by Organic Solvents(accpeted). *J. Phys.: Cond. Matt.* **2014**.

(21) Walden, P. Molecular Weights and Electrical Conductivity of Several Fused Salts. *Bull. Russian Acad. Sci.* **1914**, *1800*, 405–422.

(22) Kumar, A.; Singh, G. Ionic Liquids: Physico-Chemical, Solvent Properties and Their Applications in Chemical Processes. *Indian J. Chem. A* **2008**, *47*, 495-503.

(23) Compton, R. G.; Silvester, D. S. Electrochemistry in Room Temperature Ionic Liquids: A Review and Some Possible Applications. *Z. Phys. Chem.* **2006**, *220*, 1247-1274.

(24) Reisinger, A. Contract Research & Development at Iolitec. **2007**, 3.

(25) Tsuda, T.; Hussey, C. L. Electrochemical Applications of Room-Temperature Ionic Liquids. *Electrochem. Soc. Interface* **2007**, *16*, 42-49.

(26) Prausnitz, J. M.; Papaiconomou, N.; Salminen, J.; Lee, J. M. Physicochemical Properties of Hydrophobic Ionic Liquids Containing 1-Octylpyridinium, 1-Octyl-2-Methylpyridinium, or 1-Octyl-4-Methylpyridinium Cations. *J. Chem. Eng. Data* **2007**, *52*, 833-840.

(27) Davis, J. H. Task-Specific Ionic Liquids. *Chem. Lett.* **2004**, *33*, 1072-1077.

(28) Xiao, D.; Hines, L. G.; Li, S. F.; Bartsch, R. A.; Quitevis, E. L.; Russina, O.; Triolo, A. Effect of Cation Symmetry and Alkyl Chain Length on the Structure and Intermolecular Dynamics of 1,3-Dialkylimidazolium Bis(Trifluoromethanesulfonyl)Amide Ionic Liquids. *J. Phys. Chem. B* **2009**, *113*, 6426-6433.

(29) Seddon, K. R.; Stark, A.; Torres, M. J. Viscosity and Density of 1-Alkyl-3-Methylimidazolium Ionic Liquids. *Clean Solvents* **2002**, *819*, 34-49.

(30) Tokuda, H.; Hayamizu, K.; Ishii, K.; Susan, M. A.; Watanabe, M. Physicochemical Properties and Structures of Room Temperature Ionic Liquids. 2. Variation of Alkyl Chain Length in Imidazolium Cation. *J. Phys. Chem. B* **2005**, *109*, 6103-6110.

(31) Russina, O.; Beiner, M.; Pappas, C.; Russina, M.; Arrighi, V.; Unruh, T.; Mullan, C. L.; Hardacre, C.; Triolo, A. Temperature Dependence of the Primary Relaxation in 1-Hexyl-3-Methylimidazolium Bis{(Trifluoromethyl)Sulfonyl}Imide. *J. Phys. Chem. B* **2009**, *113*, 8469-8474.

(32) Yamaguchi, T.; Mikawa, K.-i.; Koda, S.; Fujii, K.; Endo, H.; Shibayama, M.; Hamano, H.; Umebayashi, Y. Relationship between Mesoscale Dynamics and Shear Relaxation of Ionic Liquids with Long Alkyl Chain. *J. Chem. Phys.* **2012**, *137*, 104511.

(33) Bhargava, B. L.; Balasubramanian, S. Dynamics in a Room-Temperature Ionic Liquid: A Computer Simulation Study of 1,3-Dimethylimidazolium Chloride. *J. Chem. Phys.* **2005**, *123*, 144505.

(34) Sarangi, S. S.; Zhao, W.; Müller-Plathe, F.; Balasubramanian, S. Correlation between Dynamic Heterogeneity and Local Structure in a Room-Temperature Ionic Liquid: A Molecular Dynamics Study of [Bmim][PF_6]. *ChemPhysChem* **2010**, *11*, 2001-2010.

(35) Hu, Z.; Margulis, C. J. Heterogeneity in a Room-Temperature Ionic Liquid: Persistent Local Environments and the Red-Edge Effect. *Proc. Natl. Acad. Sci. U. S. A.* **2006**, *103*, 831-836.

(36) Padua, A. A. H.; Lopes, J. N. A. C. Nanostructural Organization in Ionic Liquids. *J. Phys. Chem. B* **2006**, *110*, 3330-3335.

(37) Triolo, A.; Russina, O.; Fazio, B.; Triolo, R.; Di Cola, E. Morphology of 1-Alkyl-3-Methylimidazolium Hexafluorophosphate Room Temperature Ionic Liquids. *Chem. Phys. Lett.* **2008**, *457*, 362-365.

(38) Wang, Y.; Voth, G. A. Unique Spatial Heterogeneity in Ionic Liquids. *J Am Chem Soc* **2005**, *127*, 12192-12193.

(39) Wang, Y.; Voth, G. A. Tail Aggregation and Domain Diffusion in Ionic Liquids. *J. Phys. Chem. B* **2006**, *110*, 18601-18608.

(40) Margulis, C. J. Computational Study of Imidazolium-Based Ionic Solvents with Alkyl Substituents of Different Lengths. *Mol Phys* **2004**, *102*, 829-838.

(41) Lopes, J. N. A. C.; Padua, A. A. H. Nanostructural Organization in Ionic Liquids. *J Phys Chem B* **2006**, *110*, 3330-3335.

(42) Glatter, O.; Kratky, O. *Small Angle X-Ray Scattering*; Academic Press: London ; New York, 1982.

(43) Bradley, A. E.; Hardacre, C.; Holbrey, J. D.; Johnston, S.; McMath, S. E. J.; Nieuwenhuyzen, M. Small-Angle X-Ray Scattering Studies of Liquid Crystalline 1-Alkyl-3-Methylimidazolium Salts. *Chem Mater* **2002**, *14*, 629-635.

(44) Russina, O.; Triolo, A.; Gontrani, L.; Caminiti, R.; Xiao, D.; Jr, L. G. H.; Bartsch, R. A.; Quitevis, E. L.; Plechkova, N.; Seddon, K. R. Morphology and Intermolecular Dynamics of 1-Alkyl-3-Methylimidazolium Bis{(Trifluoromethane)Sulfonyl}Amide Ionic Liquids: Structural and Dynamic Evidence of Nanoscale Segregation. *J. Phys.: Condens. Matter* **2009**, *21*, 424121.

(45) Triolo, A.; Russina, O.; Bleif, H. J.; Di Cola, E. Nanoscale Segregation in Room Temperature Ionic Liquids. *J Phys Chem B* **2007**, *111*, 4641-4644.
(46) Santos, C. S.; Annapureddy, H. V. R.; Murthy, N. S.; Kashyap, H. K.; Castner, E. W.; Margulis, C. J. Temperature-Dependent Structure of Methyltributylammonium Bis(Trifluoromethylsulfonyl) Amide: X Ray Scattering and Simulations. *J. Chem. Phys.* **2011**, *134*, 064501.
(47) Zheng, W.; Mohammed, A.; Hines, L. G.; Xiao, D.; Martinez, O. J.; Bartsch, R. A.; Simon, S. L.; Russina, O.; Triolo, A.; Quitevis, E. L. Effect of Cation Symmetry on the Morphology and Physicochemical Properties of Imidazolium Ionic Liquids. *J. Phys. Chem. B* **2011**, *115*, 6572-6584.
(48) Macchiagodena, M.; Gontrani, L.; Ramondo, F.; Triolo, A.; Caminiti, R. Liquid Structure of 1-Alkyl-3-Methylimidazolium-Hexafluorophosphates by Wide Angle X-Ray and Neutron Scattering and Molecular Dynamics. *J. Chem. Phys.* **2011**, *134*, 114521.
(49) Sutto, T. E.; Duncan, T. T.; Wong, T. C.; McGrady, K. Ionic Liquid Batteries: Chemistry to Replace Alkaline/Acid Energy Storage Devices. *Electrochim. Acta* **2011**, *56*, 3375-3379.
(50) Frackowiak, E.; Lota, G.; Pernak, J. Room-Temperature Phosphonium Ionic Liquids for Supercapacitor Application. *Appl. Phys. Lett.* **2005**, *86*, 164104.
(51) Lewandowski, A.; Galinski, M.; Stepniak, I. Ionic Liquids as Electrolytes. *Electrochim. Acta* **2006**, *51*, 5567-5580.
(52) Egashira, M.; Todo, H.; Yoshimoto, N.; Morita, M.; Yamaki, J. Functionalized Imidazolium Ionic Liquids as Electrolyte Components of Lithium Batteries. *J. Power Sources* **2007**, *174*, 560-564.
(53) Seki, S.; Kobayashi, Y.; Miyashiro, H.; Ohno, Y.; Usami, A.; Mita, Y.; Kihira, N.; Watanabe, M.; Terada, N. Lithium Secondary Batteries Using Modified-Imidazolium Room-Temperature Ionic Liquid. *J. Phys. Chem. B* **2006**, *110*, 10228-10230.
(54) Seki, S.; Ohno, Y.; Kobayashi, Y.; Miyashiro, H.; Usami, A.; Mita, Y.; Tokuda, H.; Watanabe, M.; Hayamizu, K.; Tsuzuki, S.; Hattori, M.; Terada, N. Imidazolium-Based Room-Temperature Ionic Liquid for Lithium Secondary Batteries - Effects of Lithium Salt Concentration. *J. Electrochem. Soc.* **2007**, *154*, A173-A177.

(55) Diaw, A.; Chagnes, A.; Carre, B.; Willmann, P.; Lemordant, D. Mixed Ionic Liquid as Electrolyte for Lithium Batteries. *J. Power Sources* **2005**, *146*, 682-684.
(56) Md. A. B. H. Susan; Noda, A.; Mitsushima, S.; Watanabe, M. Brønsted Acid–Base Ionic Liquids and Their Use as New Materials for Anhydrous Proton Conductors. *Chem. Commun.* **2003**, 938-939.
(57) Watanabe, H. N. a. M. Brønsted Acid–Base Ionic Liquids for Fuel Cell Electrolytes. *Chem. Commun.* **2007**, 2539-2541.
(58) Vatamanu, J.; Borodin, O.; Smith, G. D. Molecular Dynamics Simulations of Atomically Flat and Nanoporous Electrodes with a Molten Salt Electrolyte (Vol 12, Pg 170, 2010). *Phys. Chem. Chem. Phys.* **2010**, *12*, 15136-15138.
(59) Ohsaka, T.; Islam, M. M.; Alam, M. T. Electrical Double-Layer Structure in Ionic Liquids: A Corroboration of the Theoretical Model by Experimental Results. *J Phys Chem C* **2008**, *112*, 16568-16574.
(60) Lockett, V.; Horne, M.; Sedev, R.; Rodopoulos, T.; Ralston, J. Differential Capacitance of the Double Layer at the Electrode/Ionic Liquids Interface. *Phys Chem Chem Phys* **2010**, *12*, 12499-12512.
(61) Alam, M. T.; Islam, M. M.; Okajima, T.; Ohsaka, T. Capacitance Measurements in a Series of Room-Temperature Ionic Liquids at Glassy Carbon and Gold Electrode Interfaces. *J. Phys. Chem. C* **2008**, *112*, 16600-16608.
(62) Sachdeva, G. In *Harvard U's Science in the News* 2011.
(63) Kim, H. J.; Shim, Y. Nanoporous Carbon Supercapacitors in an Ionic Liquid: A Computer Simulation Study. *Acs Nano* **2010**, *4*, 2345-2355.
(64) Yan, T. Y.; Wang, S.; Li, S.; Cao, Z. Molecular Dynamic Simulations of Ionic Liquids at Graphite Surface. *J. Phys. Chem. C* **2010**, *114*, 990-995.
(65) Vatamanu, J.; Borodin, O.; Smith, G. D. Molecular Simulations of the Electric Double Layer Structure, Differential Capacitance, and Charging Kinetics for N-Methyl-N-Propylpyrrolidinium Bis(Fluorosulfonyl)Imide at Graphite Electrodes. *J. Phys. Chem. B* **2011**, *115*, 3073-3084.
(66) Qiao, R.; Feng, G. A.; Huang, J. S.; Dai, S.; Sumpter, B. G.; Meunier, V. The Importance of Ion Size and Electrode Curvature on Electrical Double Layers in Ionic Liquids. *Phys Chem Chem Phys* **2011**, *13*, 1152-1161.

(67) Helmholtz, H. Ueber Einige Gesetze Der Vertheilung Elektrischer Ströme in Körperlichen Leitern Mit Anwendung Auf Die Thierisch-Elektrischen Versuche. *Annalen der Physik* **1853**, *165*, 211-233.

(68) Gouy, L. G. Sur La Constitution De La Charge Électrique À La Surface D'un Électrolyte *J. Phys.* **1910**, *9*, 457-468.

(69) Chapman, D. L. A Contribution to the Theory of Electrocapillarity *Philos. Mag.* **1913**, *25*, 475-481.

(70) Stern, O. Zur Theorie Der Elektrolytischen Doppelschicht. *Z. Electrochem.* **1924**, *30*, 508-516.

(71) Butt, H.-J.; Graf, K.; Kappl, M. *Physics and Chemistry of Interfaces*; WILEY-VCH GmbH & Co. KGaA, 2004.

(72) Borodin, O.; Gorecki, W.; Smith, G. D.; Armand, M. Molecular Dynamics Simulation and Pulsed-Field Gradient Nmr Studies of Bis(Fluorosulfonyl)Imide (FSI) and Bis[(Trifluoromethyl)Sulfonyl]Imide (TFSI)-Based Ionic Liquids. *J. Phys. Chem. B* **2010**, *114*, 6786-6798.

(73) Allen, M. P.; Tildesley, D. J. *Computer Simulation of Liquids*; Oxford University Press: New York, 1987.

(74) Sachs, J. N.; Crozier, P. S.; Woolf, T. B. Atomistic Simulations of Biologically Realistic Transmembrane Potential Gradients. *J Chem Phys* **2004**, *121*, 10847-10851.

(75) Sachs, J. N.; Crozier, P. S.; Woolf, T. B. Atomistic Simulations of Biologically Realistic Transmembrane Potential Gradients. *J Chem Phys* **2004**, *121*, 10847-10851.

(76) Spohr, E. Molecular Simulation of the Electrochemical Double Layer. *Electrochim Acta* **1999**, *44*, 1697-1705.

(77) Berendsen, H. J. C.; Vanderspoel, D.; Vandrunen, R. Gromacs - a Message-Passing Parallel Molecular-Dynamics Implementation. *Comput. Phys. Commun.* **1995**, *91*, 43-56.

(78) Earle, M. J.; Seddon, K. R. Ionic Liquids. Green Solvents for the Future. *Pure Appl. Chem.* **2000**, *72*, 1391-1398.

(79) Taige, T.; Schubert, T. J. S. Physico-Chemical Properties of Ionic Liquids-Part I. **2011**, *1-11*, 4-10.

(80) Santos, C. S.; Murthy, N. S.; Baker, G. A.; Castner, E. W. Communication: X-Ray Scattering from Ionic Liquids with Pyrrolidinium Cations. *J Chem Phys* **2011**, *134*, 121101-121104.

(81) Forsyth, S. A.; Pringle, J. M.; MacFarlane, D. R. Ionic Liquids - an Overview. *Aust. J. Chem.* **2004**, *57*, 113-119.

(82) Yoshizawa, M.; Ito-Akita, K.; Ohno, H. Evidence of Inter-Action between Anion and Polyether in the Bulk. *Electrochim. Acta* **2000**, *45*, 1617-1621.

(83) Anderson, J. L.; Ding, R. F.; Ellern, A.; Armstrong, D. W. Structure and Properties of High Stability Geminal Dicationic Ionic Liquids. *J. Am. Chem. Soc.* **2005**, *127*, 593-604.

(84) Fang, D.; Yang, J. M.; Ni, C. J. Dicationic Ionic Liquids as Recyclable Catalysts for One-Pot Solvent-Free Synthesis of Alpha-Aminophosphonates. *Heteroatom. Chem.* **2011**, *22*, 5-10.

(85) Chinnappan, A.; Kim, H. Environmentally Benign Catalyst: Synthesis, Characterization, and Properties of Pyridinium Dicationic Molten Salts (Ionic Liquids) and Use of Application in Esterification. *Chem. Eng. J.* **2012**, *187*, 283-288.

(86) Fan, M. M.; Yang, J.; Jiang, P. P.; Zhang, P. B.; Li, S. S. Synthesis of Novel Dicationic Basic Ionic Liquids and Its Catalytic Activities for Biodiesel Production. *RSC Adv.* **2013**, *3*, 752-756.

(87) Liu, X. F.; Xiao, L. F.; Wu, H. J. T.; Chen, J.; Xia, C. G. Synthesis of Novel Gemini Dicationic Acidic Ionic Liquids and Their Catalytic Performances in the Beckmann Rearrangement. *Helv. Chim. Acta* **2009**, *92*, 1014-1021.

(88) Han, X. X.; Armstrong, D. W. Using Geminal Dicationic Ionic Liquids as Solvents for High-Temperature Organic Reactions. *Org. Lett.* **2005**, *7*, 4205-4208.

(89) Pagano, F.; Gabler, C.; Zare, P.; Mahrova, M.; Dorr, N.; Bayon, R.; Fernandez, X.; Binder, W. H.; Hernaiz, M.; Tojo, E.; Igartua, A. Dicationic Ionic Liquids as Lubricants. *P. I. Mech. Eng. J.-J. Eng.* **2012**, *226*, 952-964.

(90) Jin, C. M.; Ye, C. F.; Phillips, B. S.; Zabinski, J. S.; Liu, X. Q.; Liu, W. M.; Shreeve, J. M. Polyethylene Glycol Functionalized Dicationic Ionic Liquids with Alkyl or Polyfluoroalkyl Substituents as High Temperature Lubricants. *J. Mater. Chem.* **2006**, *16*, 1529-1535.

(91) Zhancy, Z. X.; Zhou, H.; Yang, L.; Tachibana, K.; Kamijima, K.; Xu, J. Asymmetrical Dicationic Ionic Liquids Based on Both Imidazolium and Aliphatic Ammonium as Potential Electrolyte Additives Applied to Lithium Secondary Batteries. *Electrochim. Acta* **2008**, *53*, 4833-4838.

(92) Cho, W. J.; Yeom, C. G.; Kim, B. C.; Kim, K. M.; Ko, J. M.; Yu, K. H. Supercapacitive Properties of Activated Carbon Electrode in Organic Electrolytes Containing Single- and Double-Cationic Liquid Salts. *Electrochim. Acta* **2013**, *89*, 807-813.

(93) Castner, E. W., Jr.; Margulis, C. J.; Maroncelli, M.; Wishart, J. F. Ionic Liquids: Structure and Photochemical Reactions. *Annu. Rev. Phys. Chem.* **2011**, *62*, 85-105.

(94) Lall, S. I.; Mancheno, D.; Castro, S.; Behaj, V.; Cohen, J. L. I.; Engel, R. Polycations. Part X. Lips, a New Category of Room Temperature Ionic Liquid Based on Polyammonium Salts. *Chem. Commun.* **2000**, 2413-2414.

(95) Payagala, T.; Huang, J.; Breitbach, Z. S.; Sharma, P. S.; Armstrong, D. W. Unsymmetrical Dicationic Ionic Liquids: Manipulation of Physicochemical Properties Using Specific Structural Architectures. *Chem. Mater.* **2007**, *19*, 5848-5850.

(96) Karna, M.; Lahtinen, M.; Hakkarainen, P. L.; Valkonen, J. Physicochemical Properties of New Dicationic Ether-Functionalized Low Melting Point Ammonium Salts. *Aust. J. Chem.* **2010**, *63*, 1122-1137.

(97) Shirota, H.; Ishida, T. Microscopic Aspects in Dicationic Ionic Liquids through the Low-Frequency Spectra by Femtosecond Raman-Induced Kerr Effect Spectroscopy. *J. Phys. Chem. B* **2011**, *115*, 10860-10870.

(98) Shirota, H.; Mandai, T.; Fukazawa, H.; Kato, T. Comparison between Dicationic and Monocationic Ionic Liquids: Liquid Density, Thermal Properties, Surface Tension, and Shear Viscosity. *J. Chem. Eng. Data* **2011**, *56*, 2453-2459.

(99) Annapureddy, H. V. R.; Kashyap, H. K.; Biase, P. M.; Margulis, C. J. What Is the Origin of the Prepeak in the X-Ray Scattering of Imidazolium-Based Room-Temperature Ionic Liquids? *J. Phys. Chem. B* **2010**, *114*, 16838–16846.

(100) Urahata, S. M.; Ribeiro, M. C. Structure of Ionic Liquids of 1-Alkyl-3-Methylimidazolium Cations: A Systematic Computer Simulation Study. *J. Chem. Phys.* **2004**, *120*, 1855-1863.

(101) Hettige, J. J.; Kashyap, H. K.; Annapureddy, H. V. R.; Margulis, C. J. Anions, the Reporters of Structure in Ionic Liquids. *J. Phys. Chem. Lett.* **2013**, *4*, 105-110.
(102) Ishida, T.; Shirota, H. Dicationic Versus Monocationic Ionic Liquids: Distinctive Ionic Dynamics and Dynamical Heterogeneity. *J. Phys. Chem. B* **2013**, *117*, 1136-1150.
(103) Bodo, E.; Chiricotto, M.; Caminiti, R. Structure of Geminal Imidazolium Bis(Trifluoromethylsulfonyl)Imide Dicationic Ionic Liquids: A Theoretical Study of the Liquid Phase. *J. Phys. Chem. B* **2011**, *115*, 14341-14347.
(104) Borodin, O. Polarizable Force Field Development and Molecular Dynamics Simulations of Ionic Liquids. *J Phys Chem B* **2009**, *113*, 11463-11478.
(105) Pierce, F.; Tsige, M.; Borodin, O.; Perahia, D.; Grest, G. S. Interfacial Properties of Semifluorinated Alkane Diblock Copolymers. *J. Chem. Phys.* **2008**, *128*, 214903.
(106) Yeganegi, S.; Soltanabadi, A.; Farmanzadeh, D. Molecular Dynamic Simulation of Dicationic Ionic Liquids: Effects of Anions and Alkyl Chain Length on Liquid Structure and Diffusion. *J. Phys. Chem. B* **2012**, *116*, 11517-11526.
(107) Lopes, J. N. C.; Deschamps, J.; Padua, A. A. H. Modeling Ionic Liquids Using a Systematic All-Atom Force Field. *J. Phys. Chem. B* **2004**, *108*, 2038-2047.
(108) Hess, B.; Bekker, H.; Berendsen, H. J. C.; Fraaije, J. G. E. M. Lincs: A Linear Constraint Solver for Molecular Simulations. *J. Comput. Chem.* **1997**, *18*, 1463-1472.
(109) Essmann, U.; Perera, L.; Berkowitz, M. L.; Darden, T.; Lee, H.; Pedersen, L. G. A Smooth Particle Mesh Ewald Method. *J. Chem. Phys.* **1995**, *103*, 8577-8593.
(110) Ji, Y. M.; Shi, R.; Wang, Y. T.; Saielli, G. Effect of the Chain Length on the Structure of Ionic Liquids: From Spatial Heterogeneity to Ionic Liquid Crystals. *J. Phys. Chem. B* **2013**, *117*, 1104-1109.
(111) Saboungi, M. L.; Aoun, B.; Goldbach, A.; Gonzalez, M. A.; Kohara, S.; Price, D. L. Nanoscale Heterogeneity in Alkyl-Methylimidazolium Bromide Ionic Liquids. *J. Chem. Phys.* **2011**, *134*, 104509.
(112) Wilson, M.; Madden, P. A. Prepeaks and 1st Sharp Diffraction Peaks in Computer-Simulations of Strong and Fragile Ionic Liquids. *Phys. Rev. Lett.* **1994**, *72*, 3033-3036.
(113) Tosi, M. P.; Price, D. L.; Saboungi, M. L. Ordering in Metal Halide Melts. *Annu. Rev. Phys. Chem.* **1993**, *44*, 173-211.

(114) Mei, Q.; Benmore, C. J.; Weber, J. K. Structure of Liquid Sio2: A Measurement by High-Energy X-Ray Diffraction. *Phys. Rev. Lett.* **2007**, *98*, 057802.
(115) Bychkov, E.; Benmore, C. J.; Price, D. L. Compositional Changes of the First Sharp Diffraction Peak in Binary Selenide Glasses. *Phys. Rev. B* **2005**, *72*, 172107.
(116) Annapureddy, H. V. R.; Kashyap, H. K.; De Biase, P. M.; Margulis, C. J. What Is the Origin of the Prepeak in the X-Ray Scattering of Imidazolium-Based Room-Temperature Ionic Liquids? *J. Phys. Chem. B* **2011**, *115*, 9507-9508.
(117) Guo, J.; Baker, G. A.; Hillesheim, P. C.; Dai, S.; Shaw, R. W.; Mahurin, S. M. Fluorescence Correlation Spectroscopy Evidence for Structural Heterogeneity in Ionic Liquids. *Phys Chem Chem Phys* **2011**, *13*, 12395-12398.
(118) Lin, C.; Busse, L. E.; Nagel, S. R.; Faber, J. Temperature Dependence of the Structure Factor of Ges2 Glass. *Phys. Rev. B* **1984**, *29*, 5060-5062.
(119) Busse, L. E.; Nagel, S. R. Temperature Dependence of the Structure Factor of As2se3 Glass up to the Glass Transition. *Phys. Rev. Lett.* **1981**, *47*, 1848-1851.
(120) Susman, S.; Volin, K. J.; Montague, D. G.; Price, D. L. The Structure of Vitreous and Liquid Gese2: A Neutron Diffraction Study. *J. Non-Cryst. Solids* **1990**, *125*, 168-180.
(121) Santos, C. S.; Murthy, N. S.; Baker, G. A.; Castner, E. W. Communication: X-Ray Scattering from Ionic Liquids with Pyrrolidinium Cations. *J. Chem. Phys.* **2011**, *134*.
(122) Kashyap, H. K.; Santos, C. S.; Annapureddy, H. V. R.; Murthy, N. S.; Margulis, C. J.; Castner, E. W. Temperature-Dependent Structure of Ionic Liquids: X-Ray Scattering and Simulations. *Farad. Discuss.* **2012**, *154*, 133-143.
(123) Russina, O.; Triolo, A.; Gontrani, L.; Caminiti, R.; Xiao, D.; Jr, L. G. H.; Bartsch, R. A.; Quitevis, E. L.; Plechkova, N.; Seddon, K. R. Morphology and Intermolecular Dynamics of 1-Alkyl-3-Methylimidazolium Bis{(Trifluoromethane)Sulfonyl}Amide Ionic Liquids: Structural and Dynamic Evidence of Nanoscale Segregation. *J. Phys.: Condens. Matter.* **2009**, *21*, 424121.
(124) Kashyap, H. K.; Hettige, J. J.; Annapureddy, H. V. R.; Margulis, C. J. Saxs Anti-Peaks Reveal the Length-Scales of Dual Positive-Negative and Polar-Apolar Ordering in Room-Temperature Ionic Liquids. *Chem. Commun.* **2012**, *48*, 5103-5105.

(125) Baltazar, Q. Q.; Chandawalla, J.; Sawyer, K.; Anderson, J. L. Interfacial and Micellar Properties of Imidazolium-Based Monocationic and Dicationic Ionic Liquids. *Colloid Surf. A* **2007**, *302*, 150-156.

(126) Deng, L.; Shi, R.; Wang, Y. T.; Ou-Yang, Z. C. Hydrogen-Bond Rich Ionic Liquids with Hydroxyl Cationic Tails. *Chem. Phys. Lett.* **2013**, *560*, 32-36.

(127) Olivier, H. Recent Developments in the Use of Non-Aqueous Ionic Liquids for Two-Phase Catalysis. *J. Mol. Catal. a-Chem.* **1999**, *146*, 285-289.

(128) Gorlov, M.; Kloo, L. Ionic Liquid Electrolytes for Dye-Sensitized Solar Cells. *Dalton Trans.* **2008**, 2655-2666.

(129) Devarajan, T.; Higashiya, S.; Dangler, C.; Rane-Fondacaro, M.; Snyder, J.; Haldar, P. Novel Ionic Liquid Electrolyte for Electrochemical Double Layer Capacitors. *Electrochem. Commun.* **2009**, *11*, 680-683.

(130) Lee, J. S.; Bae, J. Y.; Lee, H.; Quan, N. D.; Kim, H. S.; Kim, H. Ionic Liquids as Electrolytes for Li Ion Batteries. *J. Ind. Eng. Chem.* **2004**, *10*, 1086-1089.

(131) Bermudez, M. D.; Jimenez, A. E.; Sanes, J.; Carrion, F. J. Ionic Liquids as Advanced Lubricant Fluids. *Molecules* **2009**, *14*, 2888-2908.

(132) Zhou, F.; Liang, Y. M.; Liu, W. M. Ionic Liquid Lubricants: Designed Chemistry for Engineering Applications. *Chem. Soc. Rev.* **2009**, *38*, 2590-2599.

(133) Islam, M. M.; Alam, M. T.; Okajima, T.; Ohsaka, T. Electrical Double Layer Structure in Ionic Liquids: An Understanding of the Unusual Capacitance-Potential Curve at a Nonmetallic Electrode. *J. Phys. Chem. C* **2009**, *113*, 3386-3389.

(134) Feng, G.; Zhang, J. S.; Qiao, R. Microstructure and Capacitance of the Electrical Double Layers at the Interface of Ionic Liquids and Planar Electrodes. *J. Phys. Chem. C* **2009**, *113*, 4549-4559.

(135) Feng, G.; Qiao, R.; Huang, J.; Dai, S.; Sumpter, B. G.; Meunier, V. The Importance of Ion Size and Electrode Curvature on Electrical Double Layers in Ionic Liquids. *Phys. Chem. Chem. Phys.* **2011**, *13*, 1152-1161.

(136) Feng, G.; Huang, J. S.; Sumpter, B. G.; Meunier, V.; Qiao, R. A "Counter-Charge Layer in Generalized Solvents" Framework for Electrical Double Layers in Neat and Hybrid Ionic Liquid Electrolytes. *Phys. Chem. Chem. Phys.* **2011**, *13*, 14723-14734.

(137) Ania, C. O.; Pernak, J.; Stefaniak, F.; Raymundo-Pinero, E.; Beguin, F. Solvent-Free Ionic Liquids as in Situ Probes for Assessing the Effect of Ion Size on the Performance of Electrical Double Layer Capacitors. *Carbon* **2006**, *44*, 3126-3130.

(138) Shim, Y.; Kim, H. J. Nanoporous Carbon Supercapacitors in an Ionic Liquid: A Computer Simulation Study. *ACS Nano*. **2010**, *4*, 2345-2355.

(139) Bazant, M. Z.; Storey, B. D.; Kornyshev, A. A. Double Layer in Ionic Liquids: Overscreening Versus Crowding. *Phys. Rev. Lett.* **2011**, *106*.

(140) Frackowiak, E.; Beguin, F. Carbon Materials for the Electrochemical Storage of Energy in Capacitors. *Carbon* **2001**, *39*, 937-950.

(141) Simon, P.; Gogotsi, Y. Materials for Electrochemical Capacitors. *Nat. Mater.* **2008**, *7*, 845-854.

(142) Ramiasa, M.; Ralston, J.; Fetzer, R.; Sedev, R. Nanoroughness Impact on Liquid-Liquid Displacement. *J. Phys. Chem. C* **2012**, *116*, 10934-10943.

(143) Xu, B. X.; Li, Y. B.; Park, T.; Chen, X. Effect of Wall Roughness on Fluid Transport Resistance in Nanopores. *J. Chem. Phys.* **2011**, *135*.

(144) Sofos, F.; Karakasidis, T. E.; Liakopoulos, A. Effect of Wall Roughness on Shear Viscosity and Diffusion in Nanochannels. *Int. J. Heat Mass Tran.* **2010**, *53*, 3839-3846.

(145) Krekelberg, W. P.; Shen, V. K.; Errington, J. R.; Truskett, T. M. Impact of Surface Roughness on Diffusion of Confined Fluids. *J. Chem. Phys.* **2011**, *135*.

(146) Monk, J.; Singh, R.; Hung, F. R. Effects of Pore Size and Pore Loading on the Properties of Ionic Liquids Confined inside Nanoporous Cmk-3 Carbon Materials. *J. Phys. Chem. C* **2011**, *115*, 3034-3042.

(147) Singh, R.; Monk, J.; Hung, F. R. A Computational Study of the Behavior of the Ionic Liquid [Bmim+][PF_6-] Confined inside Multiwalled Carbon Nanotubes. *J. Phys. Chem. C* **2010**, *114*, 15478-15485.

(148) Coasne, B.; Viau, L.; Vioux, A. Loading-Controlled Stiffening in Nanoconfined Ionic Liquids. *J. Phys. Chem. Lett.* **2011**, *2*, 1150-1154.

(149) Singh, M. P.; Singh, R. K.; Chandra, S. Properties of Ionic Liquid Confined in Porous Silica Matrix. *ChemPhysChem*. **2010**, *11*, 2036-2043.

(150) Kanakubo, M.; Hiejima, Y.; Minami, K.; Aizawa, T.; Nanjo, H. Melting Point Depression of Ionic Liquids Confined in Nanospaces. *Chem. Commun*. **2006**, 1828-1830.

(151) Chen, S. M.; Liu, Y. S.; Fu, H. Y.; He, Y. X.; Li, C.; Huang, W.; Jiang, Z.; Wu, G. Z. Unravelling the Role of the Compressed Gas on Melting Point of Liquid Confined in Nanospace. *J. Phys. Chem. Lett.* **2012**, *3*, 1052-1055.

(152) Plimpton, S. Fast Parallel Algorithms for Short-Range Molecular-Dynamics. *J. Comput. Phys.* **1995**, *117*, 1-19.

(153) Cygan, R. T.; Liang, J. J.; Kalinichev, A. G. Molecular Models of Hydroxide, Oxyhydroxide, and Clay Phases and the Development of a General Force Field. *J. Phys. Chem. B* **2004**, *108*, 1255-1266.

(154) Zhuravlev, L. T. Concentration of Hydroxyl-Groups on the Surface of Amorphous Silicas. *Langmuir* **1987**, *3*, 316-318.

(155) Borodin, O. Polarizable Force Field Development and Molecular Dynamics Simulations of Ionic Liquids. *J. Phys. Chem. B* **2009**, *113*, 11463-11478.

(156) Sendner, C.; Horinek, D.; Bocquet, L.; Netz, R. R. Interfacial Water at Hydrophobic and Hydrophilic Surfaces: Slip, Viscosity, and Diffusion. *Langmuir* **2009**, *25*, 10768-10781.

(157) Yang, K.; Lin, Y. Z.; Lu, X. C.; Neimark, A. V. Solvation Forces between Molecularly Rough Surfaces. *J. Colloid Interf. Sci.* **2011**, *362*, 382-388.

(158) Porcheron, F.; Schoen, M.; Fuchs, A. H. Monte Carlo Simulation of a Complex Fluid Confined to a Pore with Nanoscopically Rough Walls. *J. Chem. Phys.* **2002**, *116*, 5816-5824.

(159) Vinogradova, O. I.; Yakubov, G. E. Dynamic Effects on Force Measurements. 2. Lubrication and the Atomic Force Microscope. *Langmuir* **2003**, *19*, 1227-1234.

(160) Kaggwa, G. B.; Nalam, P. C.; Kilpatrick, J. I.; Spencer, N. D.; Jarvis, S. P. Impact of Hydrophilic/Hydrophobic Surface Chemistry on Hydration Forces in the Absence of Confinement. *Langmuir* **2012**, *28*, 6589-6594.

(161) Li, T. D.; Gao, J. P.; Szoszkiewicz, R.; Landman, U.; Riedo, E. Structured and Viscous Water in Subnanometer Gaps. *Phys. Rev. B* **2007**, *75*.

(162) Rodriguez, J.; Elola, M. D.; Laria, D. Confined Polar Mixtures within Cylindrical Nanocavities. *J. Phys. Chem. B* **2010**, *114*, 7900-7908.

(163) Jun, C.; Peng, X. F.; Lee, D. J. Diffusion Coefficient of Brownian Particle in Rough Micro-Channel. *J. Colloid Interf. Sci.* **2006**, *296*, 737-742.

(164) Inagaki, M.; Konno, H.; Tanaike, O. Carbon Materials for Electrochemical Capacitors. *J. Power Sources* **2010**, *195*, 7880-7903.
(165) Liu, C. G.; Yu, Z. N.; Neff, D.; Zhamu, A.; Jang, B. Z. Graphene-Based Supercapacitor with an Ultrahigh Energy Density. *Nano Lett.* **2010**, *10*, 4863-4868.
(166) Conway, B. E. *Electrochemical Supercapacitors : Scientific Fundamentals and Technological Applications*; Kluwer Academic/Plenum: New York ; London, 1999.
(167) Cheng, Q.; Tang, J.; Ma, J.; Zhang, H.; Shinya, N.; Qin, L. C. Graphene and Carbon Nanotube Composite Electrodes for Supercapacitors with Ultra-High Energy Density. *Phys. Chem. Chem. Phys.* **2011**, *13*, 17615-17624.
(168) Kunze, M.; Jeong, S.; Paillard, E.; Winter, M.; Passerini, S. Melting Behavior of Pyrrolidinium-Based Ionic Liquids and Their Binary Mixtures. *J. Phys. Chem. C* **2010**, *114*, 12364-12369.
(169) Egashira, M.; Kanetomo, A.; Yoshimoto, N.; Morita, M. Electrode Properties in Mixed Imidazolium Ionic Liquid Electrolytes. *Electrochem.* **2010**, *78*, 370-374.
(170) Zistler, M.; Wachter, P.; Schreiner, C.; Fleischmann, M.; Gerhard, D.; Wasserscheid, P.; Hinsch, A.; Goresa, H. J. Temperature Dependent Impedance Analysis of Binary Ionic Liquid Electrolytes for Dye-Sensitized Solar Cells. *J. Electrochem. Soc.* **2007**, *154*, B925-B930.
(171) Portet, C.; Yushin, G.; Gogotsi, Y. Electrochemical Performance of Carbon Onions, Nanodiamonds, Carbon Black and Multiwalled Nanotubes in Electrical Double Layer Capacitors. *Carbon* **2007**, *45*, 2511-2518.
(172) McDonough, J. K.; Frolov, A. I.; Presser, V.; Niu, J. J.; Miller, C. H.; Ubieto, T.; Fedorov, M. V.; Gogotsi, Y. Influence of the Structure of Carbon Onions on Their Electrochemical Performance in Supercapacitor Electrodes. *Carbon* **2012**, *50*, 3298-3309.
(173) Silva, F.; Gornes, C.; Figueiredo, M.; Costa, R.; Martins, A.; Pereira, C. M. The Electrical Double Layer at the [Bmim][Pf6] Ionic Liquid/Electrode Interface - Effect of Temperature on the Differential Capacitance. *J. Electroanal. Chem.* **2008**, *622*, 153-160.
(174) Fletcher, S. I.; Sillars, F. B.; Carter, R. C.; Cruden, A. J.; Mirzaeian, M.; Hudson, N. E.; Parkinson, J. A.; Hall, P. J. The Effects of Temperature on the Performance of Electrochemical Double Layer Capacitors. *J. Power Sources* **2010**, *195*, 7484-7488.

(175) Vatamanu, J.; Borodin, O.; Smith, G. D. Molecular Insights into the Potential and Temperature Dependences of the Differential Capacitance of a Room-Temperature Ionic Liquid at Graphite Electrodes. *J. Am. Chem. Soc.* **2010**, *132*, 14825-14833.
(176) Boda, D.; Henderson, D.; Chan, K. Y. Monte Carlo Study of the Capacitance of the Double Layer in a Model Molten Salt. *J. Chem. Phys.* **1999**, *110*, 5346-5350.
(177) Boda, D.; Henderson, D. The Capacitance of the Solvent Primitive Model Double Layer at Low Effective Temperatures. *J. Chem. Phys.* **2000**, *112*, 8934-8938.
(178) Reszko-Zygmunt, J.; Sokolowski, S.; Henderson, D.; Boda, D. Temperature Dependence of the Double Layer Capacitance for the Restricted Primitive Model of an Electrolyte Solution from a Density Functional Approach. *J. Chem. Phys.* **2005**, *122*.
(179) Boda, D.; Henderson, D.; Chan, K. Y.; Wasan, D. T. Low Temperature Anomalies in the Properties of the Electrochemical Interface. *Chem. Phys. Lett.* **1999**, *308*, 473-478.
(180) Ukshe, E. A.; Bukun, N. G.; Leikis, D. I.; Frumkin, A. N. Investigation of the Electric Double Layer in Salt Melts. *Electrochim. Acta* **1964**, *9*, 431-439.
(181) Bukun, N. G. T., N. S.; Ukshe, E. A. Double Layer Capacity on Molybdenum in Fused Salts. *Elektrokhimiya* **1970**, *6*, 1215-1218.
(182) Alam, M. T.; Islam, M. M.; Okajima, T.; Ohsaka, T. Measurements of Differential Capacitance at Mercury/Room-Temperature Ionic Liquids Interfaces. *J. Phys. Chem. C* **2007**, *111*, 18326-18333.
(183) Kisza, A. The Capacitance of the Diffuse Layer of Electric Double Layer of Electrodes in Molten Salts. *Electrochim. Acta* **2006**, *51*, 2315-2321.
(184) Loth, M. S.; Skinner, B.; Shklovskii, B. I. Anomalously Large Capacitance of an Ionic Liquid Described by the Restricted Primitive Model. *Phys. Rev. E* **2010**, *82*.
(185) Holovko, M.; Kapko, V.; Henderson, D.; Boda, D. On the Influence of Ionic Association on the Capacitance of an Electrical Double Layer. *Chem. Phys. Lett.* **2001**, *341*, 363-368.
(186) Yang, L.; Fang, S.; Jin, Y.; Hirano, S.; Tachibana, K.; Katayama, S. Functionalized Ionic Liquids Based on Quaternary Ammonium Cations with Three or Four Ether Groups as New Electrolytes for Lithium Battery. *Electrochim. Acta* **2011**, *56*, 4663-4671.

(187) Fedorov, M. V.; Kornyshev, A. A. Towards Understanding the Structure and Capacitance of Electrical Double Layer in Ionic Liquids. *Electrochim. Acta* **2008**, *53*, 6835-6840.

(188) Su, Y. Z.; Yan, J. W.; Li, M. G.; Zhang, M.; Mao, B. W. Electric Double Layer of Au(100)/Imidazolium-Based Ionic Liquids Interface: Effect of Cation Size. *J. Phys. Chem. C* **2013**, *117*, 205-212.

(189) Alam, M. T.; Masud, J.; Islam, M. M.; Okajima, T.; Ohsaka, T. Differential Capacitance at Au(111) in 1-Alkyl-3-Methylimidazolium Tetrafluoroborate Based Room-Temperature Ionic Liquids. *J. Phys. Chem. C* **2011**, *115*, 19797-19804.

(190) Mayrand-Provencher, L.; Lin, S. X.; Lazzerini, D.; Rochefort, D. Pyridinium-Based Protic Ionic Liquids as Electrolytes for Ruo2 Electrochemical Capacitors. *J. Power Sources* **2010**, *195*, 5114-5121.

(191) Lockett, V.; Horne, M.; Sedev, R.; Rodopoulos, T.; Ralston, J. Differential Capacitance of the Double Layer at the Electrode/Ionic Liquids Interface. *Phys. Chem. Chem. Phys.* **2010**, *12*, 12499-12512.

(192) Fedorov, M. V.; Georgi, N.; Kornyshev, A. A. Double Layer in Ionic Liquids: The Nature of the Camel Shape of Capacitance. *Electrochem. Commun.* **2010**, *12*, 296-299.

(193) Vatamanu, J.; Borodin, O.; Bedrov, D.; Smith, G. D. Molecular Dynamics Simulation Study of the Interfacial Structure and Differential Capacitance of Alkylimidazolium Bis(Trifluoromethanesulfonyl)Imide [C(N)Mim][Tfsi] Ionic Liquids at Graphite Electrodes. *J. Phys. Chem. C* **2012**, *116*, 7940-7951.

(194) Kurig, H.; Vestli, M.; Tonurist, K.; Janes, A.; Lust, E. Influence of Room Temperature Ionic Liquid Anion Chemical Composition and Electrical Charge Delocalization on the Supercapacitor Properties. *J. Electrochem. Soc.* **2012**, *159*, A944-A951.

(195) Costa, R.; Pereira, C. M.; Silva, F. Double Layer in Room Temperature Ionic Liquids: Influence of Temperature and Ionic Size on the Differential Capacitance and Electrocapillary Curves. *Phys. Chem. Chem. Phys.* **2010**, *12*, 11125-11132.

(196) Fedorov, M. V.; Kornyshev, A. A. Ionic Liquid near a Charged Wall: Structure and Capacitance of Electrical Double Layer. *J. Phys. Chem. B* **2008**, *112*, 11868-11872.

(197) Lauw, Y.; Horne, M. D.; Rodopoulos, T.; Nelson, A.; Leermakers, F. A. M. Electrical Double-Layer Capacitance in Room Temperature Ionic Liquids: Ion-Size and Specific Adsorption Effects. *J. Phys. Chem. B* **2010**, *114*, 11149-11154.

(198) Feng, G.; Zhang, J. S.; Qiao, R. Microstructure and Capacitance of the Electrical Double Layers at the Interface of Ionic Liquids and Planar Electrodes. *J. Phys. Chem. C* **2009**, *113*, 4549-4559.

(199) Simon, P.; Gogotsi, Y. Capacitive Energy Storage in Nanostructured Carbon-Electrolyte Systems. *Accounts Chem. Res.* **2013**, *46*, 1094-1103.

(200) Simon, P.; Gogotsi, Y. Charge Storage Mechanism in Nanoporous Carbons and Its Consequence for Electrical Double Layer Capacitors. *Philos. T. R. Soc. A* **2010**, *368*, 3457-3467.

(201) McDonough, J. K.; Gogotsi, Y. Carbon Onions: Synthesis and Electrochemical Applications. *Electrochem. Soc. Interface* **2013**, *22*, 61-66.

(202) Zhu, Y. W.; Murali, S.; Stoller, M. D.; Ganesh, K. J.; Cai, W. W.; Ferreira, P. J.; Pirkle, A.; Wallace, R. M.; Cychosz, K. A.; Thommes, M.; Su, D.; Stach, E. A.; Ruoff, R. S. Carbon-Based Supercapacitors Produced by Activation of Graphene. *Science* **2011**, *332*, 1537-1541.

(203) Tokuda, H.; Baek, S. J.; Watanabe, M. Room-Temperature Ionic Liquid-Organic Solvent Mixtures: Conductivity and Ionic Association. *Electrochemistry* **2005**, *73*, 620-622.

(204) Arulepp, M.; Permann, L.; Leis, J.; Perkson, A.; Rumma, K.; Janes, A.; Lust, E. Influence of the Solvent Properties on the Characteristics of a Double Layer Capacitor. *J. Power Sources* **2004**, *133*, 320-328.

(205) Lin, R.; Taberna, P. L.; Chmiola, J.; Guay, D.; Gogotsi, Y.; Simon, P. Microelectrode Study of Pore Size, Ion Size, and Solvent Effects on the Charge/Discharge Behavior of Microporous Carbons for Electrical Double-Layer Capacitors. *J. Electrochem. Soc.* **2009**, *156*, A7-A12.

(206) Guerfi, A.; Dontigny, M.; Charest, P.; Petitclerc, M.; Lagac√©, M.; Vijh, A.; Zaghib, K. Improved Electrolytes for Li-Ion Batteries: Mixtures of Ionic Liquid and Organic Electrolyte with Enhanced Safety and Electrochemical Performance. *J. Power Sources* **2010**, *195*, 845-852.

(207) Diaw, M.; Chagnes, A.; Carre, B.; Willmann, P.; Lemordant, D. Mixed Ionic Liquid as Electrolyte for Lithium Batteries. *J. Power Sources* **2005**, *146*, 682-684.
(208) Yu, Z.; Vlachopoulos, N.; Hagfeldt, A.; Kloo, L. Incompletely Solvated Ionic Liquid Mixtures as Electrolyte Solvents for Highly Stable Dye-Sensitized Solar Cells. *RSC Adv*. **2013**, *3*, 1896-1901.
(209) *Encyclopedia of Electrochemical Power Sources*; Garche, J., Ed.; Elsevier: Amberg, 2009.
(210) Chaban, V. V.; Voroshyloya, I. V.; Kalugin, O. N.; Prezhdo, O. V. Acetonitrile Boosts Conductivity of Imidazolium Ionic Liquids. *J. Phys. Chem. B* **2012**, *116*, 7719-7727.
(211) Van Aken, K. L.; McDonough, J. K.; Li, S.; Feng, G.; Chathoth, S. M.; Mamontov, E.; Fulvio, P. F.; Cummings, P. T.; Dai, S.; Gogotsi, Y. Effect of Cation on Diffusion Coefficient of Ionic Liquids at Onion-Like Carbon Electrodes (Submitted). **2013**.
(212) Feng, G.; Huang, J. S.; Sumpter, B. G.; Meunier, V.; Qiao, R. Structure and Dynamics of Electrical Double Layers in Organic Electrolytes. *Phys. Chem. Chem. Phys.* **2010**, *12*, 5468-5479.
(213) Merlet, C.; Salanne, M.; Rotenberg, B.; Madden, P. A. Influence of Solvation on the Structural and Capacitive Properties of Electrical Double Layer Capacitors. *Electrochim. Acta* **2013**, *101*, 262-271.
(214) Feng, G.; Huang, J. S.; Sumpter, B. G.; Meunier, V.; Qiao, R. A "Counter-Charge Layer in Generalized Solvents" Framework for Electrical Double Layers in Neat and Hybrid Ionic Liquid Electrolytes. *Phys. Chem. Chem. Phys.* **2011**, *13*, 14723-14734.
(215) Jiang, D. E.; Jin, Z. H.; Henderson, D.; Wu, J. Z. Solvent Effect on the Pore-Size Dependence of an Organic Electrolyte Supercapacitor. *J. Phys. Chem. Lett.* **2012**, *3*, 1727-1731.
(216) Cornell, W. D.; Cieplak, P.; Bayly, C. I.; Gould, I. R.; Merz, K. M.; Ferguson, D. M.; Spellmeyer, D. C.; Fox, T.; Caldwell, J. W.; Kollman, P. A. A Second Generation Force Field for the Simulation of Proteins, Nucleic Acids, and Organic Molecules *J. Am. Chem. Soc.* **1995**, *117*, 5179-5197.
(217) Nikitin, A. M.; Lyubartsev, A. P. New Six-Site Acetonitrile Model for Simulations of Liquid Acetonitrile and Its Aqueous Mixtures. *J. Comput. Chem.* **2007**, *28*, 2020-2026.

(218) Wang, J. M.; Wolf, R. M.; Caldwell, J. W.; Kollman, P. A.; Case, D. A. Development and Testing of a General Amber Force Field. *J. Comput. Chem.* **2004**, *25*, 1157-1174.

(219) Yang, L.; Fishbine, B. H.; Migliori, A.; Pratt, L. R. Dielectric Saturation of Liquid Propylene Carbonate in Electrical Energy Storage Applications. *J. Chem. Phys.* **2010**, *132*.

(220) Wu, H. P.; Fang, Y.; Wan, H. D.; Xia, Y. M. Effect of Low Dosage Ionic Liquid on R-Miehei Lipase-Catalyzed Synthesis of Arnyl Caprylate in Organic Solvent. *Acta Chim. Sinica* **2008**, *66*, 823-826.

(221) Salminen, J.; Papaiconomou, N.; Kumara, R. A.; Lee, J. M.; Kerr, J.; Newman, J.; Prausnitz, J. M. Physicochemical Properties and Toxicities of Hydrophobic Piperidinium and Pyrrolidinium Ionic Liquids. *Fluid Phase Equilibr.* **2007**, *261*, 421-426.

(222) Triolo, A.; Russina, O.; Fazio, B.; Appetecchi, G. B.; Carewska, M.; Passerini, S. Nanoscale Organization in Piperidinium-Based Room Temperature Ionic Liquids. *J. Chem. Phys.* **2009**, *130*.

(223) Feng, G.; Jiang, D.; Cummings, P. T. Curvature Effect on the Capacitance of Electric Double Layers at Ionic Liquid/Onion-Like Carbon Interfaces. **2012**.

(224) Si, X. J.; Li, S.; Wang, Y. L.; Ye, S. H.; Yan, T. Y. Effects of Specific Adsorption on the Differential Capacitance of Imidazolium-Based Ionic Liquid Electrolytes. *ChemPhysChem* **2012**, *13*, 1671-1676.

(225) Kornyshev, A. A. Double-Layer in Ionic Liquids: Paradigm Change? *J. Phys. Chem. B* **2007**, *111*, 5545-5557.

(226) Huang, J. S.; Sumpter, B. G.; Meunier, V.; Yushin, G.; Portet, C.; Gogotsi, Y. Curvature Effects in Carbon Nanomaterials: Exohedral Versus Endohedral Supercapacitors. *J. Mater. Res.* **2010**, *25*, 1525-1531.

(227) Dou, Q.; Sha, M. L.; Fu, H. Y.; Wu, G. Z. Molecular Dynamics Simulation of the Interfacial Structure of [C(N)Mim][Pf6] Adsorbed on a Graphite Surface: Effects of Temperature and Alkyl Chain Length. *J. Phys.:Condens. Mat.* **2011**, *23*, 175001.

(228) Ghatee, M. H.; Zolghadr, A. R.; Moosavi, F.; Ansari, Y. Studies of Structural, Dynamical, and Interfacial Properties of 1-Alkyl-3-Methylimidazolium Iodide Ionic Liquids by Molecular Dynamics Simulation. *J. Chem. Phys.* **2012**, *136*, 124706-124719.

(229) Romero, C.; Moore, H. J.; Lee, T. R.; Baldelli, S. Orientation of 1-Butyl-3-Methylimidazolium Based Ionic Liquids at a Hydrophobic Quartz Interface Using Sum Frequency Generation Spectroscopy. *J. Phys. Chem. C* **2007**, *111*, 240-247.

(230) Islam, M. M.; Alam, M. T.; Ohsaka, T. Electrical Double-Layer Structure in Ionic Liquids: A Corroboration of the Theoretical Model by Experimental Results. *J. Phys. Chem. C* **2008**, *112*, 16568-16574.

(231) Alam, M. T.; Islam, M.; Okajima, T.; Ohsaka, T. Ionic Liquid Structure Dependent Electrical Double Layer at the Mercury Interface. *J. Phys. Chem. C* **2008**, *112*, 2601-2606.

(232) Alam, M. T.; Islam, M. M.; Okajima, T.; Ohsaka, T. Measurements of Differential Capacitance in Room Temperature Ionic Liquid at Mercury, Glassy Carbon and Gold Electrode Interfaces. *Electrochem. Commun.* **2007**, *9*, 2370-2374.

(233) Kurig, H.; Vestli, M.; Janes, A.; Lust, E. Electrical Double Layer Capacitors Based on Two 1-Ethyl-3-Methylimidazolium Ionic Liquids with Different Anions. *Electrochem. Solid. St. Lett.* **2011**, *14*, A120-A122.

(234) Richey, F. W.; Dyatkin, B.; Gogotsi, Y.; Elabd, Y. A. Ion Dynamics in Porous Carbon Electrodes in Supercapacitors Using in Situ Infrared Spectroelectrochemistry. *J. Am. Chem. Soc.* **2013**, *135*, 12818-12826.

(235) Presser, V.; Heon, M.; Gogotsi, Y. Carbide-Derived Carbons - from Porous Networks to Nanotubes and Graphene. *Adv. Funct. Mater.* **2011**, *21*, 810-833.

(236) Liang, C. D.; Li, Z. J.; Dai, S. Mesoporous Carbon Materials: Synthesis and Modification. *Angew Chem. Int. Edit.* **2008**, *47*, 3696-3717.

(237) Kofu, M.; Nagao, M.; Ueki, T.; Kitazawa, Y.; Nakamura, Y.; Sawamura, S.; Watanabe, M.; Yamamuro, O. Heterogeneous Slow Dynamics of Imidazolium-Based Ionic Liquids Studied by Neutron Spin Echo. *J. Phys. Chem. B* **2013**, *117*, 2773-2781.

(238) Feng, G.; Li, S.; Atchison, J. S.; Presser, V.; Cummings, P. T. Molecular Insights into Carbon Nanotube Supercapacitors: Capacitance Independent of Voltage and Temperature. *J. Phys. Chem. C* **2013**, *117*, 9178-9186.

(239) Kotz, R.; Carlen, M. Principles and Applications of Electrochemical Capacitors. *Electrochim. Acta* **2000**, *45*, 2483-2498.

(240) Burke, A. Ultracapacitors: Why, How, and Where Is the Technology. *J. Power Sources* **2000**, *91*, 37-50.
(241) Wu, Z. S.; Parvez, K.; Feng, X. L.; Mullen, K. Graphene-Based in-Plane Micro-Supercapacitors with High Power and Energy Densities. *Nat. Commun.* **2013**, *4*.